# Quantify Plasma Response to Non-Axisymmetric (3D) Magnetic Fields in Tokamaks, Final Report for FES FY2014 Joint Research Target

E.J. Strait[1], J.-K. Park[2], E.S. Marmar[3], J.-W. Ahn[4], J.W. Berkery[5], K.H. Burrell[1], J.M. Canik[4], L. Delgado-Aparicio[2], N.M. Ferraro[1], A.M. Garofalo[1], D.A. Gates[2], M. Greenwald[3], K. Kim[2], J.D. King[1], M.J. Lanctot[1], S.A. Lazerson[2], Y.Q. Liu[6], N.C. Logan[2], J.D. Lore[4], J. E. Menard[2], R. Nazikian[2], M.W. Shafer[4], C. Paz-Soldan[1], A.H. Reiman[2], J.E. Rice[3], S.A. Sabbagh[5], L. Sugiyama[3], A.D. Turnbull[1], F. Volpe[5], Z.R. Wang[2], and S.M. Wolfe[3]

[1]*General Atomics, San Diego, CA 92186, USA*
[2]*Princeton Plasma Physics Laboratory, Princeton, NJ 08543, USA*
[3]*Massachusetts Institute of Technology, Cambridge, MA, 02139, USA*
[4]*Oak Ridge National Laboratory, Oak Ridge, TN 37831-6372, USA*
[5]*Columbia University, New York, NY 10027, USA*
[6]*Euratom/CCFE Association, Culham Science Center, Abingdon OX14 3DB, UK*

## Annual Target

Conduct experiments and analysis to investigate and quantify plasma response to non-axisymmetric (3D) magnetic fields in tokamaks. Effects of 3D fields can be both beneficial and detrimental and research will aim to validate theoretical models in order to predict plasma performance with varying levels and types of externally imposed 3D fields. Dependence of response to multiple plasma parameters will be explored in order to gain confidence in predictive capability of the models.

## Quarter Milestones

**4th Quarter Milestone**: Complete the required experiments and analysis. Prepare a joint report summarizing the contributions toward the understanding of the plasma response to 3D fields, and identifying possible paths to optimizing the use of 3D fields in tokamaks.

## CONTENTS

# 1. Overview

The goal of the 2014 Joint Research Target (JRT) has been to conduct experiments and analysis to investigate and quantify the response of tokamak plasmas to non-axisymmetric (3D) magnetic fields. Although tokamaks are conceptually axisymmetric devices, small asymmetries often result from inaccuracies in the manufacture and assembly of the magnet coils, or from nearby magnetized objects. In addition, non-axisymmetric fields may be deliberately applied for various purposes. Even at small amplitudes of order $10^{-4}$ of the main axisymmetric field, such "3D" fields can have profound impacts on the plasma performance. The effects are often detrimental (reduction of stabilizing plasma rotation, degradation of energy confinement, localized heat flux to the divertor, or excitation of instabilities) but may in some case be beneficial (maintenance of rotation, or suppression of instabilities).

In general, the magnetic response of the plasma alters the 3D field, so that the magnetic field configuration within the plasma is not simply the sum of the external 3D field and the original axisymmetric field. Typically the plasma response consists of a mixture of local screening of the external field by currents induced at resonant surfaces in the plasma, and amplification of the external field by stable kink modes. Thus, validated magnetohydrodynamic (MHD) models of the plasma response to 3D fields are crucial to the interpretation of existing experiments and the prediction of plasma performance in future devices. The non-axisymmetric coil sets available at each facility allow well-controlled studies of the response to external 3D fields.

The work performed in support of the 2014 Joint Research Target has included joint modeling and analysis of existing experimental data, and collaboration on new experiments designed to address the goals of the JRT. A major focus of the work was validation of numerical models through quantitative comparison to experimental data, in order to gain confidence in their ability to predict the performance of ITER and other burning plasmas. An important element of this effort was also to verify experimentally the limits of validity of the models. The rest of this overview will summarize the key results of the work, with parentheses indicating references to the relevant sections of the present report.

A significant effort was made to validate a range of non-axisymmetric MHD codes against experimental data. This work complements an ongoing theoretical initiative to benchmark the codes against each other [1,2]. Linear and non-linear ideal MHD models, and a resistive two-fluid model, were all in rough quantitative agreement with DIII-D measurements of the response to an applied perturbation with toroidal mode number $n$=3. In particular, MARS-F (a linear, ideal MHD model) was in good quantitative agreement

with poloidally resolved magnetic measurements (2.9). In addition, measurements of edge displacements are in good agreement with ideal MHD models (2.8). These results confirm the expectation that in many circumstances ideal MHD provides a good representation of tokamak plasmas.

The limit of validity of linear MHD models has been an important topic of investigation. A direct experimental measurement has confirmed linear behavior of the plasma response to perturbations in the range of most present error fields and applied fields. Comparison of several nonlinear models suggests that initial disagreements with experimental data may be due to the approximations in the numerical codes, rather than a fundamental difficulty with the non-linear physics (2.7).

As expected from the foregoing results, linear ideal MHD has been successful in modeling various specific aspects of the plasma response. The experimental observation of a dramatic difference between single-null and double-null plasma geometries, in the high field side plasma response to perturbations applied on the low field side, has been reproduced by several MHD models (2.2). Ideal MHD predictions are also in good qualitative agreement with the variation of the high field side structure as the plasma current (or edge safety factor) varies (2.3).

DIII-D and NSTX data, in combination with modeling, show that the simplified picture of a plasma response dominated by a single stable eigenmode may become invalid as beta (normalized plasma pressure) increases. New DIII-D data shows that at beta approaching the no-wall stability limit, the poloidal structure of the $n$=1 plasma response varies with the shape of the external field, suggesting the presence of multiple eigenmodes of comparable importance. This trend is qualitatively reproduced by MHD modeling that includes kinetic effects. Ideal MHD modeling of high-beta, wall-stabilized NSTX plasmas also shows that at high beta several eigenmodes can have a role in the plasma response (2.4).

The ideal MHD approximation is also found to break down at high beta. The inclusion of non-ideal drift-kinetic physics (resonances with ion drift motion) allows models to predict a smoothly rising stable plasma response at high beta, with an amplitude in good quantitative agreement with experimental observations in both NSTX and DIII-D, as well as the decreasing response seen at very high beta in NSTX. The inclusion of drift-kinetic terms also yields closer agreement of the model with the internal 3D structure of the plasma, as measured by a soft-x-ray diagnostic (2.5).

Very recent experiments show that suppression of edge-localized modes (ELMs) by applied 3D fields may be associated with nonlinear, non-ideal MHD effects. As the poloidal structure of an applied $n$=2 field is varied, discontinuous changes in the magnetic response are observed at transitions into and out of the ELM-suppressed state. These

changes are consistent with the formation of an island at the top of the H-mode pressure pedestal, and may depend on modification of the local rotation (or radial electric field) caused by the applied 3D field (2.6).

The compensation of intrinsic error fields is an important aspect of applied 3D fields. A long history of success with empirically determined $n$=1 compensation has recently been reinforced by the successful calculation of the required compensation coil currents, based on measurements of the error fields. This calculation is based on the single-mode picture of the plasma response, which implies that the compensation field can have a very different spatial structure from that of the error field, as long as it couples to the single dominant eigenmode of the plasma. Experiments have now confirmed that there is very little effect on the plasma from an external field designed not to couple to the dominant eigenmode (3.1). As noted earlier, however, this picture can become more complicated as beta approaches and exceeds the no-wall beta limit, where additional eigenmodes may become important (2.4).

Recent experiments indicate that it may not be possible to extend this simple single-mode paradigm to $n$=2 error fields. Empirical compensation of an $n$=2 artificial "proxy" error field, using a compensating field having a poor spatial match to the error field, is in good agreement with a prediction based on minimization of the torque due to neoclassical toroidal viscosity (NTV). However, this optimized compensation was unable to fully recover the loss of plasma rotation caused by the error field (3.3). An initial attempt at simultaneous $n$=1 and $n$=2 compensation of the local perturbation from a Test Blanket Module mockup yielded a similar result (3.4). Unlike the $n$=1 case, an $n$=2 external field designed to be "orthogonal" to the optimized compensation field still has a significant braking effect (3.5). These results indicate the possible excitation of multiple stable eigenmodes with comparable strength, and imply the need for closer spatial matching of the compensation field to the error field.

Non-resonant magnetic braking (or in some cases acceleration) of plasma rotation through NTV is an important effect of 3D fields. Plasma rotation may have a significant impact on transport and stability, so the capability to predict NTV torque is a crucial element of 3D physics. Several NTV models were benchmarked against each other, including semi-analytic and particle simulation models. Good qualititative agreement was found, and in some cases quantitative agreement. The differences can be understood in terms of the approximations of the different models (4.1)

NTV models are well supported by experimental data. Three NTV models are in quantitative agreement with the volume-integrated torque from $n$=3 non-resonant braking in a DIII-D discharge. Despite the challenges posed to the models by low aspect ratio, large particle orbits, and rapid toroidal rotation, the predicted $n$=3 torque profile in NSTX is in reasonable agreement with the measured profile. These results are sensitive to the

internal 3D magnetic field structure generated by the perturbation, and the non-ideal response including drift-kinetic physics may be needed to account for modification of the mode structure by NTV effects (4.2, 4.4).

Computational tools for stellarator design have been combined with NTV models in studies for the design and operation of the Non-axisymmetric Control Coils (NCC) in NSTX-U. It was shown that the planned NCC coils can be optimized for large central torque with low edge torque, a combination that also minimizes resonant fields that could otherwise lead to tearing mode. The resulting field configuration is similar to the "orthogonal" fields discussed in Sec. 3, which minimize coupling to the dominant eigenmodes. The optimization routine was successfully benchmarked against empirical $n$=1 error field compensation in DIII-D (4.3).

3D fields can lead to high local heat flux in the divertor, through "strike point splitting" and other magnetic field asymmetries. Linear ideal MHD modeling shows that the plasma's magnetic response, including resonant screening and non-resonant amplification by stable kink modes, enhances strike point splitting and may lead to large peak heat flux. Strong strike point splitting is predicted when the kink response is increased by varying the plasma shape and spatial structure of the applied 3D field, in qualitative agreement with DIII-D data (5.1).

As observed in NSTX, 3D fields can also alter the divertor heat flux by causing a detached divertor plasma to re-attach, presumably by increasing the local divertor heat flux. 3D transport modeling using the perturbed fields shows local hot spots at the divertor, in qualitative agreement with experiments (5.2).

Experiments in DIII-D have shown that applied 3D fields can control the position of a magnetic island and aid electron cyclotron current drive (ECCD) stabilization of locked modes, allowing recovery of H-mode operation (6.2). In C-Mod, delay of the onset of a locked mode and locked-mode recovery has been successfully obtained without external momentum input, using ion cyclotron resonance heating (ICRH). Power above a threshold level unlocks the mode, allowing a return to H-mode operation and recovery of the toroidal rotation (6.3).

In summary, research carried out in support of the 2014 Joint Research Target has validated 3D MHD models against experimental data. In many cases, linear ideal MHD is found to provide a good description of the plasma response to small-amplitude external 3D magnetic fields, and regimes were identified where additional physics must be included in the mode. The limits of the simplified picture of plasma response dominated by a single eigenmode were also explored, particularly in the context of error field compensation. Neoclassical toroidal viscosity is found to be a good representation of the torque resulting from 3D fields. Modeling predictions of the effects of the 3D plasma

response on divertor heat flux were found to be in qualitative agreement with experiments. Applied 3D fields have important applications that include disruption avoidance and recovery of H-mode operation after an instability.The joint work summarized here represents significant progress in the field of 3D effects in tokamak plasmas, and will provide a springboard for future research.

## References

[1] A.D. Turnbull, et al., Phys. Plasmas **20**, 056114 (2013).

[2] A. Reiman, et al., Proceedings of the 41st European Physical Society Conference on Plasma Physics, Berlin, 2014 (EPS, Petit-Lancy, Switzerland) paper P2.058, online at ocs.ciemat.es/EPS2014PAP/pdf/P2.058.pdf

# 2. Validation of Models For 3D Plasma Response

## 2.1 Introduction

The extent to which models of plasma response are able to describe the observed non-axisymmetric response has been investigated through comprehensive modeling of DIII-D and NSTX experiments. In particular, several experiments run this year on DIII-D were specifically designed to yield precise data appropriate for testing plasma response models over a range of parameters. These experiments included steady-state, up-down symmetric hybrid discharges amenable to modeling with a broad range of codes (including those requiring or preferring stellarator symmetry), and ITER similar-shaped experiments in ELM suppression regimes. Modeling of these experiments, and of experiments from previous years on DIII-D and NSTX, has helped define the limits of our quantitative understanding of non-axisymmetric response. In addition, these experiments have provided a wealth of data that will be used as a basis for model validation and understanding non-axisymmetric response in the future.

This section focuses on experimental results that provide clear, quantitative tests for model validation, and the results of modeling efforts that have been applied to these cases thus far. These results include the disparate dependences of the high-field side (HFS) and low-field side (LFS) magnetic response on the plasma geometry (Sec.2.2); the dependence of the HFS poloidal structure on the safety factor profile (Sec. 2.3); the amplification of the response and emergence of multiple eigenmodes at high $\beta$ (Sec. 2.4), and the breakdown of ideal-MHD as the no-wall limit is exceeded (Sec. 2.5); an investigation of the characteristics of plasma response as the plasma enters and exits ELM suppression (Sec. 2.6); an investigation of the extent to which the plasma response is linear with the applied fields (Sec. 2.7); and measurements of non-axisymmetric perturbations caused by intrinsic MHD (Sec. 2.8). Finally, the results of a multi-code benchmarking and validation effort, in which the predicted magnetic response from IPEC [1], M3D-C1 [2,3], MARS-F [4], NSTAB [5], and VMEC [6] is compared with experimental data, are presented in Sec. 2.9.

In general, plasma response models are found to reproduce the experimental results qualitatively, and often quantitatively. In particular, linear modeling is found to reproduce the observed HFS/LFS response dependence on geometry; and the HFS structure dependence on $q_{95}$; and the amplification and multi-mode response at high $\beta$. While ideal-MHD appears to be adequate to describe most externally measurable features of the magnetic response below the no-wall limit, more sophisticated models, including stabilizing kinetic resonance effects, are found to be necessary to describe experimental results as this limit

is approached and exceeded. Additionally, although it has been shown previously that assumptions of linearity may be violated in typical DIII-D and NSTX discharges, it is shown here that linear modeling is apparently sufficient to describe most aspects of the magnetic response. Conversely, nonlinearity is clearly present in the axisymmetric transport response and in the dynamics of mode locking.

This section excludes results that specifically pertain to the topics of subsequent sections: the role of plasma response in error field correction (Sec. 3); transport and NTV (Sec. 4); divertor heat flux (Sec. 5); and island penetration and locking (Sec. 6).

### 2.2 Dependence of Plasma Response on Equilibrium Geometry

A one-day experiment was performed on DIII-D to study the magnetic response of the plasma to externally applied magnetic perturbations, toward the goal of experimental validation of a range of 3D equilibrium and stability codes. This experiment used an up-down symmetric double-null configuration, which can be modeled by the widest range of codes, including stellarator codes. The discharge was run in "hybrid" mode, maintaining the central safety factor $q_0$>1, with a steady-state $n$=3 perturbation applied by the I-coil.

The experiment yielded the unexpected result that the magnetic response on the high field side of the plasma, away from the I-coils, was a factor of 3–4 smaller in amplitude than for comparable single-null plasmas (Fig. 2-1). This strong difference between the two cases was confirmed by visible light imaging of the plasma edge at the high field side (HFS). The LFS magnetic response was very similar in the two cases. Other data included variation of the amplitude of the applied $n$=3 field, to look for possible nonlinearities in the magnetic response at the threshold for reduction of particle confinement ("density pump-out"); this is discussed in Sec. 2.7.

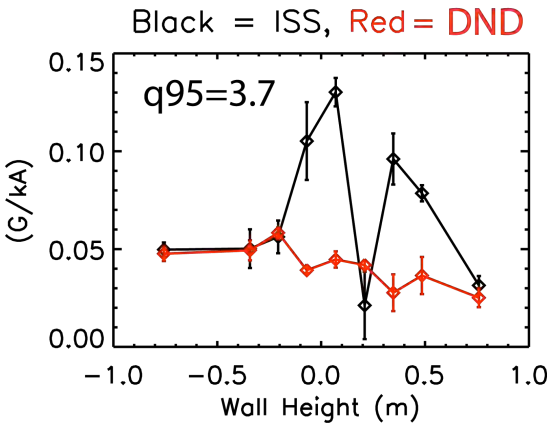


Fig. 2-1. Amplitude of the magnetic response to an *n=3* field applied with the I-coil, plotted vs. height along the high field side wall. Cases shown are an up-down symmetric double null configuration (DND) and an ITER-like lower single-null configuration (SND) with similar plasma current and $\beta_N$.

The dramatic difference in the high field side plasma response between the two plasma shapes might be related to the difference in peeling-ballooning eigenfunctions of DNDs versus SNDs. In H-modes, the least-stable $n$=3 eigenfunctions tend to be peeling-ballooning like, localized to the steep-gradient region of the pedestal [7]. In DND, this eigenfunction is restricted to the LFS, whereas in SND the eigenfunction tends to wrap around to the high-field side along the

edge of the plasma opposite the active x-point. Physically, this difference is due to the near field-alignment of the least-stable mode.

DIII-D discharges 154243 and 154247, which had DN and lower SN geometry respectively, were modeled with IPEC, M3D-C1, MARS-F, and VMEC. On the HFS, all four codes showed a clear enhancement of the field from the plasma response in the SND relative to the DND, and relatively less change on the LFS. Results of the M3D-C1, MARS-F, and IPEC modeling are shown in Fig. 2-2. This is in qualitative agreement with the experimental result, although a quantitative comparison will require further analysis of the magnetics data to accurately compensate for the vacuum field coupling.

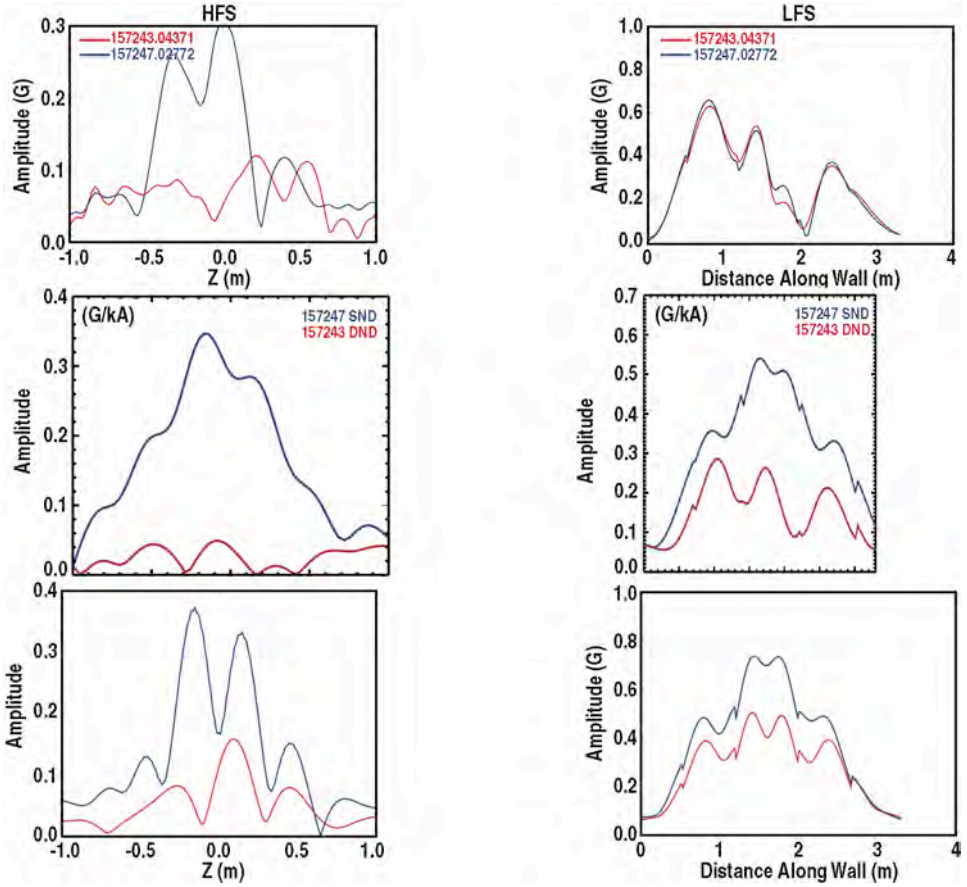


Fig. 2-2. The magnitude of the tangential field from the plasma response on the high-field side (left) and low-field side (right) in M3D-C1 (top) and MARS-F (center), and IPEC (bottom) modeling, for DIII-D discharges 157243 (double-null) and 157247 (lower single-null).

### 2.3 Dependence of High-Field Side Structure on $q_{95}$

A number of recent experiments in DIII-D since the installation of the new magnetic probe set have observed the plasma response during ramps of the plasma current. Among these is an experiment that was conducted this year to investigate the plasma's response to applied $n$=3 magnetic perturbations as the current was ramped through ELM suppression windows. For this experiment, an ITER-like single-null configuration was used. Detailed measurements of the plasma response included magnetics [8], fast camera imaging, and soft x-ray (XR) imaging [9] of the edge pedestal region.

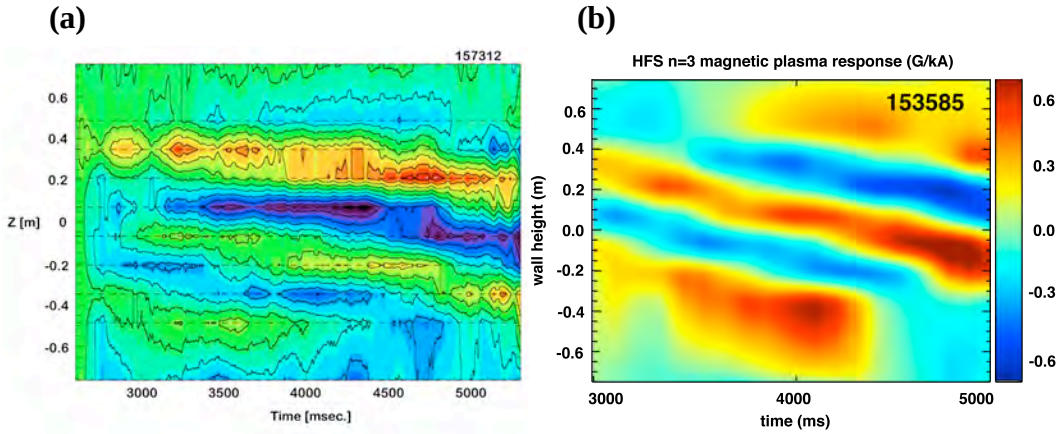


Fig. 2-3. Contours of the amplitude of the magnetic response to an $n$=3 field applied with the I-coil, vs time and height along the high field side wall, for two similar lower single-null discharges with increasing plasma current. From $t$ = 3000 ms to $t$ = 5000 ms, $q_{95}$ decreases from (a) 3.8 to 3.3 and (b) 3.8 to 3.1. The discharges differ in $\beta_N$ and $l_i$ with (a) $\beta_N \approx 1.7$, $l_i \approx 0.95$, and (b) $\beta_N \approx 2.2$, $l_i \approx 0.75$.

This experiment yielded detailed measurements of the magnetic structure as the safety factor at the normalized poloidal flux surface $\Psi_N$ = 95% ($q_{95}$) was slowly varied. The magnetic structure of the plasma response on the high-field side was seen to move downward as the current was increased, as shown in Fig. 2-3(a). In contrast, the magnetic structure on the low-field side remained essentially constant. This experimental result is qualitatively similar to a previous measurement of the $n$=3 response at the high field side, shown in Fig. 2-3(b). However, the two cases show a distinct difference in the rate at which the structure varies vs. time and $q_{95}$, perhaps related to differences in β and internal inductance ($l_i$) of the two discharges.

DIII-D discharge 157312, from which the data shown in Fig. 2-3(a) was taken, was modeled with both M3D-C1 and IPEC, using reconstructed equilibria at four different times during the current ramp. The magnitude of the plasma response predicted by M3D-C1 at those four times at the high field sidewall is shown in Fig. 2-4. Consistent with the experiment, the peaks of the plasma response were found to move vertically downward by 20–25 cm over the duration of the current ramp. This M3D-C1 calculation was done using a linear, resistive, two-fluid model; roughly the same vertical shift was also found us-

using a single-fluid model. The ideal MHD result from IPEC, plotted as a function of $q_{95}$, is shown in Fig. 2-5(b). (Note that $q_{95}$ was decreasing in time, so the vertical shift appears to be in the opposite direction.) IPEC finds a similar qualitative behavior, with the magnetic structure shifting vertically on the HFS as a function of $q_{95}$, although the shift appears to be somewhat larger in the IPEC modeling relative to the M3D-C1 result. This discrepancy is not yet well understood, but may provide insight into the role of non-ideal effects in the plasma response.

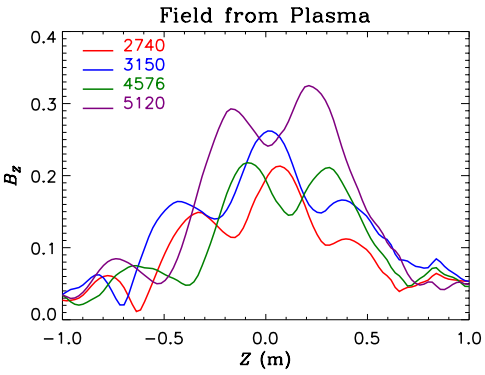


Fig. 2-4. The plasma response at the high field sidewall, as calculated by M3D-C1 or DIII-D discharge 157312. Consistent with the experimental results, the peak of the response near the midplane at $t$ = 2740 ms is found to move downward vertically by roughly 20–25 cm by $t$ = 5120 ms.

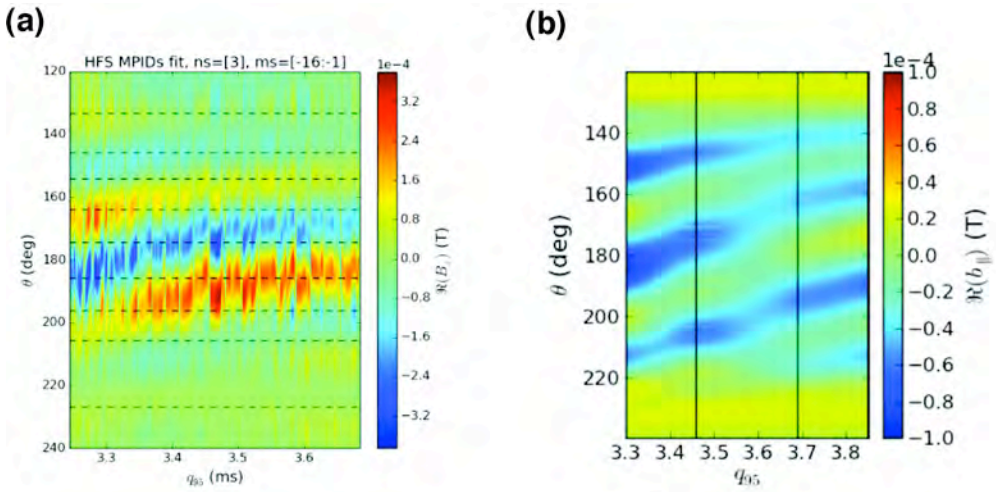


Fig. 2-5. (a) Tangential field due to the plasma response measured on the high field sidewall for DIII-D discharge 157312, as a function of $q_{95}$ and geometric angle from the magnetic axis ($\theta$ = 180° represents the HFS midplane). Dashed horizontal lines indicate the locations of magnetic probes. (b) The same quantity, as predicted by IPEC modeling. Solid vertical lines (including the vertical axes) indicate the four equilibria used; the interstitial values are interpolated.

Analysis of SXR imaging data from an earlier DIII-D discharge (149454) with a $q_{95}$ scan shows that the internal response also varies with $q_{95}$. (The DIII-D SXR imaging diagnostic requires higher density or $Z_{eff}$ than was achieved in 157312 for adequate signal-to-noise ratio.) Figure 2-6 shows the perturbed SXR imaging signal at the $\beta_N$=97.5% surface, in the steep-gradient region of the pedestal, as a function of the geometric poloidal angle and $q_{95}$. In particular, the poloidal wavenumber of the response in the pedestal is found to increase with $q_{95}$, which is consistent with a field-aligned perturbation that remains at a fixed radial location as $q$ increases. The evolution in the phase of the mode is such that the perturbation on the LFS remains essentially fixed, while additional periods

of the field perturbation are "born" from the x-point as $q_{95}$ increases, compressing the structure on the HFS.

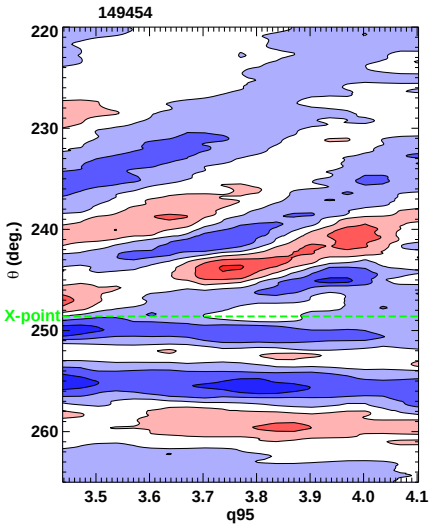


Fig. 2-6. The perturbed SXR signal from the $\beta_N$=97.5% surface, as a function of geometric poloidal angle and $q_{95}$. The x-point is at $\theta \approx 248°$; lower values are on the HFS, and higher values are on the LFS.

### 2.4 Dependence of Plasma Response on β

The plasma response in DIII-D and NSTX is observed to depend on the plasma β. As β is increased, the response, as measured by magnetic probes and internal displacements, is also observed to increase. This trend is consistent for $n$=1–3. Furthermore, the spatial structure of the measured response changes as β increases, especially as β approaches and exceeds the no-wall limit. How the spatial structure depends on β is itself found to be dependent on the poloidal spectrum of the applied fields, indicating that multiple eigenmodes are present in the response, and that these eigenmodes have different dependences on β. The presence of these multiple modes may have implications for coil design for stability control and error field correction.

In DIII-D, the presence of multiple modes at various values of $\beta_N$ was probed by varying the poloidal spectrum of an applied $n$=1 field. This was accomplished by changing the relative phases of the upper and lower I-coil rows. At values of $\beta_N$ below the ideal no-wall stability limit ($\beta_N \approx 2.2$ in this case), the phase and amplitude of the response measured at the high field sidewall is very weakly dependent on the spectrum of the applied field, as can be seen in Fig. 2-7(a). A response that is independent of the details of the applied field is consistent with excitation of a single stable eigenmode. In contrast, at higher $\beta_N$, the poloidal structure and magnitude of response is strongly dependent on the applied fields, as can be seen in Fig. 2-7(b), indicating that multiple eigenmodes are present in the response. At high $\beta_N$, the strongest response is found at a relative phase of 240°, which differs from the relative phase of 300° measured previously for peak coupling at lower beta [13]. In addition, there is a qualitative change in the response from two peaks to one peak, depending on the structure of the applied field (240° vs 300° relative phase of the upper and lower coils). These differences suggest the excitation of a second eigenmode at high beta that is more strongly coupled to the 240° field configuration.

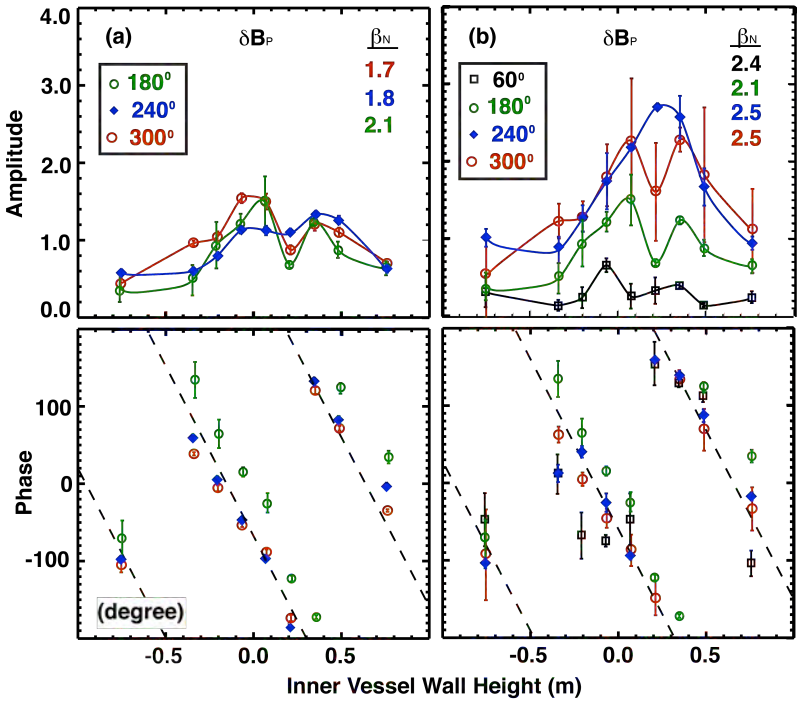


Fig. 2-7. The amplitude (top) and phase (bottom) of the poloidal field component of the *n*=1 plasma response measured at the DIII-D vacuum vessel wall along with a spline fit to the amplitude profiles, at values of $\beta_N$ (a) below and (b) near or above the ideal no-wall limit. Different colors/symbols represent different relative phases of the upper and lower I-coil rows.

Figure 2-8(a) shows the strong dependence of the plasma response to kink-resonant (240°) applied fields over a larger range of $\beta_N$, as well as the qualitative change in poloidal structure as $\beta_N$ increases. The MARS-K results in Fig. 2-8(b) show a similar trend of strongly increasing amplitude and greater peaking of the spatial structure at high beta. The transition to the peaked mode structure occurs at a somewhat higher beta in the model, perhaps as a result of overestimating the drift-kinetic damping. The radial structure of the plasma response in MARS-K (not shown) also exhibits a qualitative change at high beta, possibly as a result of the excitation of a second stable eigenmode. The presence of these multiple modes may have implications for coil design for stability control and error field correction.

One potential consequence of the presence of multiple modes is that the influence of multiple eigenmodes in RWM spectra on *n*=1 active feedback, including the stable mode spectrum, may cause $\beta_N$ fluctuation and loss of control. The multi-mode VALEN code has been applied to NSTX experiments to determine the multi-mode resistive wall mode (RWM) spectrum and characteristics. The multi-mode response is theoretically computed to be significant in NSTX plasmas when $\beta_N$>5.2 [10,11], based on the criterion of Boozer [12]. The perturbed normal field due to induced wall currents shows the influence

of the NSTX passive conducting plates Fig. 2-9(a). The computed RWM growth time vs $\beta_N$ is in the range observed when such modes are destabilized Fig. 2-9(b).

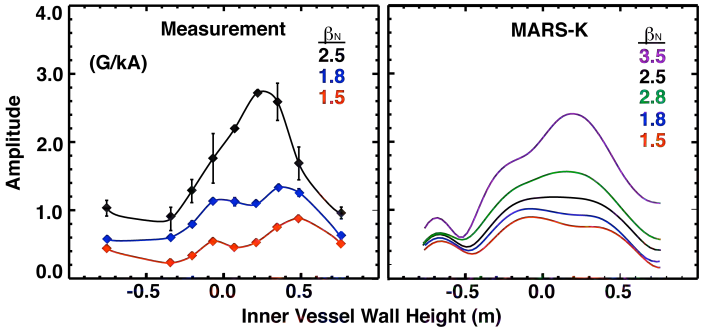


Fig. 2-8. The *n*=1 magnetic plasma response amplitude over a range of $\beta_N$ as measured (a) and predicted by MARS-K (b) on the DIII-D high field sidewall. The applied fields use a relative I-coil phasing of 240°.

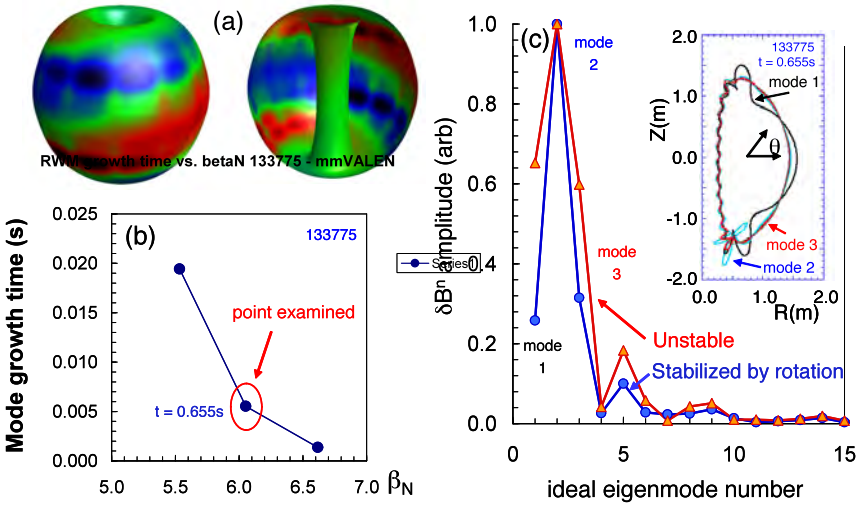


Fig. 2-9. (a) Multi-mode RWM analysis of high $\beta_N$ plasmas (a) $\delta B_{normal}$ from wall currents; (b) growth time vs $\beta_N$, for unstable modes; and (c) ideal eigenmode spectrum of multi-mode RWM perturbation showing the spectrum of an unstable mode, and one stabilized by plasma rotation.

The computed spectrum of ideal-MHD eigenmodes comprising the total perturbed field Fig 2-9(c) is shown for an unstable RWM, and one stabilized by plasma rotation. The RWM multi-mode spectra consist of ideal-MHD eigenmodes computed by the DCON code. These eigenmodes are ordered from lower to higher number, with the lowest number being least stable when each eigenmode is considered separately in ideal-MHD theory. Both spectra show significant amplitude in eigenmodes up to 10, with the *second* eigenmode having the maximum amplitude. Poloidal cross-sections of the eigenmodes are also shown. Eigenmode 1 is ballooning, while eigenmode 2, which has dominant amplitude, has maximum perturbation near the lower divertor. There is a significant change

in the multi-mode RWM spectrum for the stabilized plasma. In this case, the ballooning component of the perturbation is significantly reduced compared to the component with maximum perturbation in the lower divertor region. The rotationally stabilized multi-mode RWM has a computed rotation frequency of 41 Hz, close to the ~30 Hz frequency measured in experiments with both magnetic and kinetic diagnostics (SXR).

The preceding results show the dependence of the $n$=1 response on $\beta$, but similar trends are found to hold at higher $n$ as well. An experiment was conducted on DIII-D to investigate the sensitivity of H-mode plasmas to $n$=2 perturbations over a range of $\beta_N$. The $n$=2 response is advantageous in that it exhibits some features similar to what is observed in both $n$=1 and $n$=3 perturbations. Like $n$=1, the amplitude of the low field side $n$=2 response rises with $\beta_N$, consistent with excitation of a stable $n$=2 kink mode (Fig. 2-10). Like $n$=3, the $n$=2 perturbation with amplitude above a threshold value produces density pump-out. The appearance of phenomena associated both with $n$=3 and $n$=1 applied fields yields an opportunity to study the importance of stable kink mode excitation to the commonly observed transport responses of $n$>1 fields.

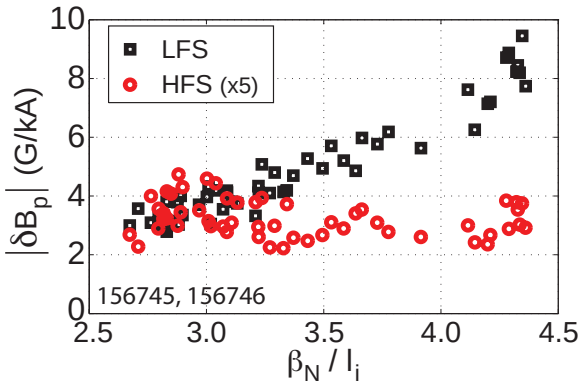


Fig. 2-10. Magnetic response of the plasma (at the low and high field side midplane) to a rotating $n$=2 field applied with the I-coil, with MARS-F prediction.

## 2.5 Kinetic Effects in the Plasma Response at High $\beta$

It has previously been shown that ideal-MHD over-predicts the plasma response to externally applied $n$=1 magnetic perturbations as the no-wall Troyon $\beta$ limit is approached and exceeded [13]. Recently, it has been found that a model that self-consistently includes drift kinetic resonance effects offers a significant improvement to the quantitative description of the plasma response in this high-$\beta$ regime. Furthermore, measurements showing that the plasma response is maximized at a finite field rotation frequency, and is reduced at high $\beta_N/l_i$ in NSTX, also suggest that kinetic effects play an important role in plasma response at high $\beta$.

The MARS-K code solves the linear hybrid MHD equation including resonant kinetic effects through the non-adiabatic kinetic pressure ($p_{||}$ and $p_{\perp}$) which includes contributions from both thermal particles (TPs) and energetic particles (slowing down distribution, EPs). In particular, the non-adiabatic contributions come from the resonant drift kinetic effects associated with the particles' toroidal precession, as well as bounce (for

trapped particles) or transit (for passing particles) motions. The external coils, resistive wall, and the vacuum are also included in the MARS-K simulation.

This work resolves an outstanding issue of the ideal-MHD model, which finds a very high (almost singular) amplification near the no-wall $\beta$ limit, denoted as $\beta^{NW}$. The large plasma response is due to the ideal potential energy approaching zero when $\beta$ approaches $\beta^{NW}$. In contrast, experiments [14,15] show the plasma response increases smoothly along with $\beta$ across the ideal $\beta^{NW}$. This disagreement between ideal MHD theory and experiments is studied through a quantitative comparison between MARS-K modeling and experimental results in DIII-D [13] and NSTX [16]. Since the drift kinetic effects can dramatically modify the plasma response structure, the results also highlight the importance of solving the model equations self-consistently.

In a study of DIII-D experiments, the amplitude of plasma response, measured by the radial magnetic sensors located at the LFS midplane, is compared in Fig. 2-11(a) with that computed by MARS-F/K. Here, MARS-F solves the plasma response using a linear ideal-MHD model (labeled the "fluid" model). The ideal-MHD response agrees well with experiments till the normalized $\beta_N = 0.81\,\beta_N^{NW}$, suggesting that the ideal-MHD approximation is adequate for modeling the plasma response at low $\beta$. However, significant disagreement between the ideal-MHD prediction and experiments appears as the plasma pressure approaches or exceeds the no-wall beta limit. Much better agreement is obtained by the kinetic response computations with MARS-K (labeled the "thermal" model). In this model, adiabatic contributions from both TPs and EPs are included, but the non-adiabatic term includes the TPs contribution only. The kinetic effects result in a complex dissipative drift kinetic energy and modify the structure of the plasma response.

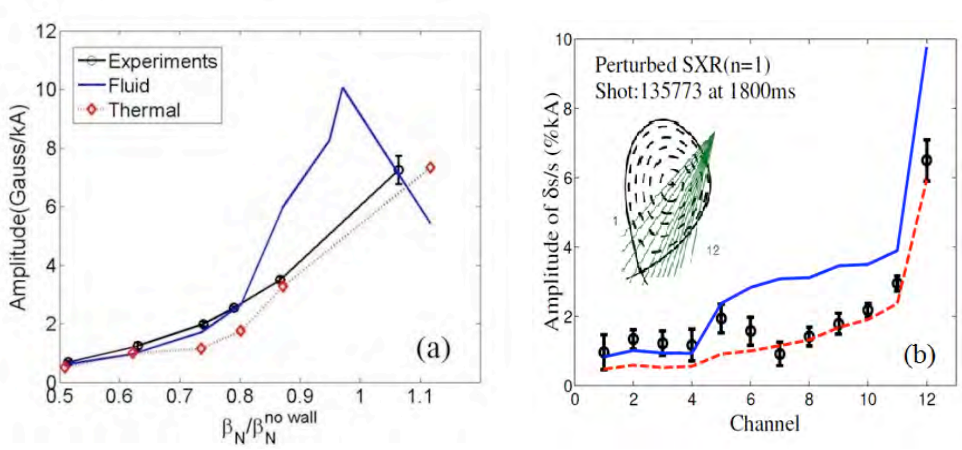


Fig. 2-11. (a) The amplitude of plasma response measured at the magnetic sensor is plotted as a function of $\beta_N^{NW}$ for ideal-MHD ("fluid") and kinetic ("thermal") plasma response. (b) Comparison of amplitude between the measured (dotted) and computed soft x-ray structure of plasma response at $\beta_N$=0.87 $\beta_N^{NW}$. The inset shows the sightline geometry of each SXR channel. Here, $\beta_N^{NW}$ is around 2.25.

This work reveals the key importance of kinetic effects from the TPs. Figure 2-11(b) shows another crucial validation of the kinetic model. The internal structure of plasma response computed by MARS-K/F is compared with SXR measurements in DIII-D experiments at $\beta_N = 0.81\,\beta_N^{NW}$ near the ideal no-wall $\beta$ limit. It is noted that the ideal-MHD response (solid line) largely overestimates the amplitude of the internal perturbation. The kinetic response (dashed line), on the other hand, generally shows very good quantitative agreement with experiments, in both amplitude and phase. Moreover, the hybrid kinetic-MHD theory predicts that the resistive wall modes are stable in the highest beta case ($\beta_N = 1.12\,\beta_N^{NW}$), which is consistent with the experimental observation.

In NSTX plasma response studies, the kinetic plasma response increases smoothly across the no-wall $\beta$ limit, as shown in Fig. 2-12(a). We note that the plasma response is strongly coupled to the resistive wall since the 30 Hz applied external fields is close to the field penetrating frequency of wall ~40 Hz in NSTX. Therefore, the ideal-MHD response with resistive wall (dashed line) shows a strong suppression of amplitude comparing with the no wall case (solid line). Moreover, both "fluid" cases show a large phase value when $\beta_N$ approaches or exceeds $\beta_N^{NW}$, which differs from the small phase shift observed in NSTX experiments. The kinetic plasma response not only agrees with the measured amplitude, but also maintains a relatively small phase shift as in the experiments.

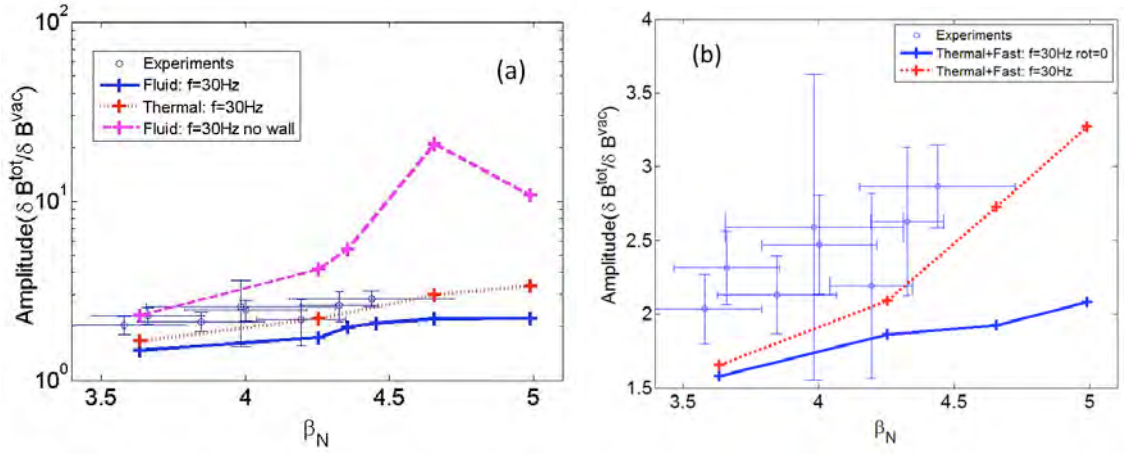


Fig, 2-12. The $\beta_N$ dependence of plasma response amplitude measured at the LFS midplane. (a) The ideal-MHD plasma response ("fluid," with/without resistive wall) and kinetic plasma response ("thermal" case) are compared. (b) The "Thermal+Fast" cases of kinetic plasma response with/without fluid rotation are presented. The $\beta_N^{NW}$ in NSTX experiments, is around 4.6.

Since NSTX plasmas can achieve much faster fluid rotation than DIII-D plasmas, it is important to investigate the importance of rotation in the kinetic plasma response calculations for NSTX. Figure 2-12(b) clearly shows the kinetic plasma response with the fluid rotation (dotted line) has much larger amplitude than the case without rotation (solid

line). The "thermal + fast" case additionally includes non-adiabatic contributions of EPs, which are not present in the "thermal" case. This indicates that the fluid rotation could have a destabilizing effect in the plasma, which is consistent with the results in a recent NSTX Ideal Wall Mode study [17]. The perturbed energy analysis shows the inertial energy plays the dominant role in destabilizing the plasma and leads to the larger amplitude of response. In both experiments, the energy analysis also shows the modification of plasma response is mainly contributed by the precession, bounce, and transit resonances of thermal ions.

Kinetic effects are also likely responsible for the dependence of the magnitude of plasma response on the rotation rate of applied fields, and for enhanced stability of NSTX plasmas at high $\beta_N/l_i$ in NSTX. Early experiments determined the maximum plasma response as a function of the toroidal rotation frequency of applied field, and the field rotation direction. For NSTX, the maximum was found to occur when the field rotates in the co- neutral beam injection (NBI) direction, at a frequency between 30 and 40 Hz [14]. At fixed frequency, the plasma response was found to increase with $\beta_N$, as its value was increased to values approaching and exceeding the $n$=1 ideal MHD no-wall beta limit [18], as shown in Fig. 2-13. Similar results were also found and reported in DIII-D [13,19] and JET [20].

More recent experiments on NSTX at higher $\beta_N$ and lower $l_i$ have shown a more complex dependence of the plasma response on these parameters. Operation at higher $\beta_N/l_i$ in NSTX (while still at the highest $\beta_N$ produced in the device) yields plasma operation with the highest margin over the $n$=1 no-wall limit. In this regime, the $n$=1 ideal no-wall $\beta$ limit can be exceeded by 100% [21]. At these highest margins over the no-wall limit, the resonant field amplification (RFA) [22] — the enhancement of the total field relative to the applied field — of an applied 40 Hz co-NBI rotating $n$=1 field showed an increase to a broad peak near $\beta_N/l_i$=10. This decrease in RWM stability, shown by the increase in RFA, was expected from past results mentioned above as $\beta_N$ increased. In contrast, and remarkably, the RFA was found to decrease at higher values of $\beta_N/l_i$ indicating increased RWM stability (Fig 2-14). This reduction in plasma response is likely related to the proximity to broad kinetic resonances in plasma rotation (e.g. ion precession drift resonance) providing kinetic stabilization of the RWM [23–25]. The Fig. 2-14 also illustrates two plasmas (RFA amplitudes increase off-scale in the figure) that become unstable and suffer disruptions at intermediate $\beta_N/l_i$. This was not observed at the highest $\beta_N/l_i$ in these experiments, and is consistent with other high $\beta_N$ NSTX experiments that showed that disruptions occurred more frequently at intermediate values of $\beta_N/l_i$, rather than at the highest values.

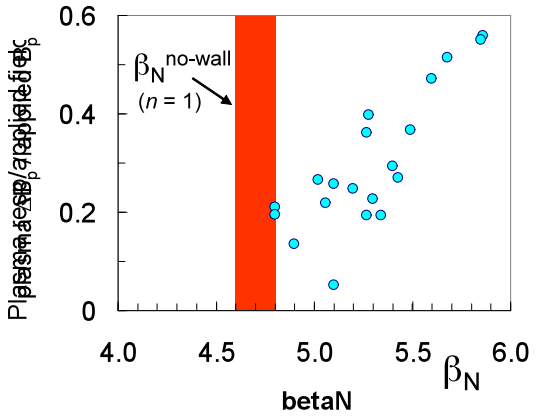


Fig. 2-13. Increase in the $n$=1 resonant field amplification with increasing $\beta_N$ for an externally applied $n$=1 magnetic field in NSTX.

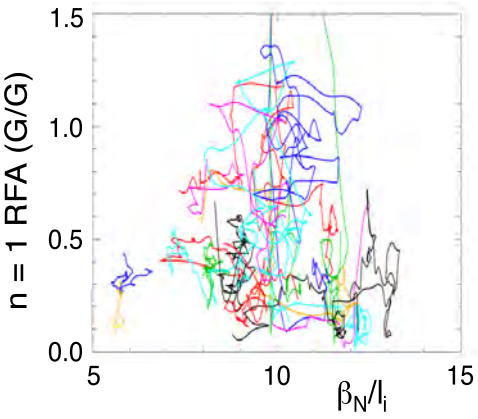


Fig, 2-14. Non-monotonic dependence of $n$=1 RFA vs $\beta_N/l_i$ during high-$\beta$ NSTX discharges, indicating improved stability at high $\beta_N/l_i$ in NSTX.

## 2.6 Plasma Response in ELM Suppression Regimes

As the poloidal spectrum of an applied field is changed, ELM suppression is found to be coincident with the phase that maximizes the plasma response, both as measured by the magnetic response and the transport response. Additionally, clear, rapid changes to the measured plasma response are observed as the plasma enters and exits an ELM-suppressed state. These changes are consistent with the penetration of an $n$=3 island at the top of the pedestal.

An experiment to measure the plasma response in an ELM suppressed regime as a function of the applied poloidal spectrum was conducted this year on DIII-D. Here $n$=2 fields, which can be rotated continuously, were applied by the I-coils. These discharges were configured as ITER-similar shape plasmas, with normalized current ($I_N$) of 1.2, neutral beam injected power of 6 MW, modest electron resonance heating of 1 MW, yielding a normalized pedestal electron collisionality ($\nu_{*e}$) of 0.23. The value of $q_{95}$ of 4.1 in these discharges is a half-integer above the standard $n$=2 ELM suppression window [26]. The in-vessel coils were configured such that the lower in-vessel coil row was fixed in toroidal phase ($\phi_{IL}$), while the upper row toroidal phase ($\phi_{IU}$) could be continuously rotated. Scanning only $\phi_{IU}$ yields a continuous scan in upper-lower phase difference ($\Delta\phi_{UL} = \phi_{IU} - \phi_{IL}$), thus scanning the applied $n$=2 poloidal spectrum.

As shown in Fig. 2-15, density pump-out, thermal confinement loss, and braking were all found to be maximum in the range $\Delta\phi_{UL} \approx 0$–45°. Furthermore, ELM suppression was also found to occur in this range. Measurements of the fields due to the plasma response show that this phase coincides with the maximum plasma response on the HFS midplane [Fig 2-16(a)], but not the on the LFS midplane [Fig 2-16(b)]. These distinct responses indicate that at least two separate components of the magnetic response exist, each of which is preferentially excited by a different $n$=2 poloidal spectrum and preferentially detected on the LFS or HFS.

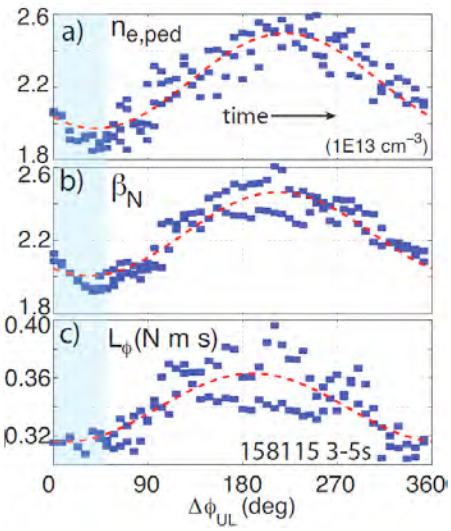


Fig. 2-15. The electron density at the top of the pedestal ($n_{e,ped}$), the normalized beta ($\beta_N$), and the toroidal momentum ($L_\phi$) are plotted as a function of $\otimes\phi_{UL}$. ELM suppression (shaded blue region) occurs near the phase where all three of these quantities are minimized.

Ideal and resistive MHD calculations with IPEC and MARS-F find that the LFS measurement is primarily sensitive to excitation of stable kink modes, while the HFS measurement is correlated with the predicted excitation of resonant currents. The resonant currents are themselves strongly modified by kink

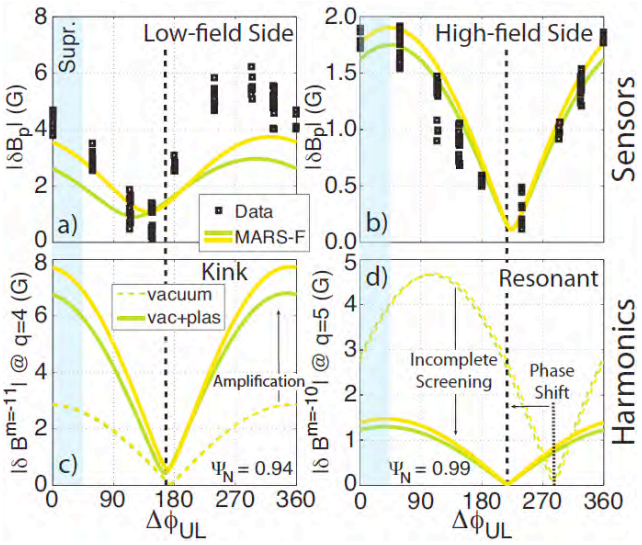


Fig. 2-16. The magnitude of the tangential magnetic field due to the plasma response (a) on the low-field side and (b) on the high-field side, as a function of the relative phase difference of the upper and lower I-coil rows. A poloidal Fourier component, $m$=11 at the $q$=4 surface, correlated with the kink-resonance is found to align well with the LFS response (c), whereas the pitch-resonant poloidal Fourier component at the $q$=5 surface aligns more closely with the HFS response (d). ELM-suppression (blue shaded region) is found to occur at the phase that maximizes the measured HFS response.

excitation, with the optimal applied helicity for pump-out and ELM suppression found to differ significantly from pitch-alignment of the vacuum fields. The role of the kink mode is thus primarily through its impact on the kink-resonant components, which in turn drive pump-out and ELM suppression.

Clear changes to the magnetic response and the temperature profile were observed as the plasma entered and exited an ELM-suppressed state during rotation of the $n$=2 applied field. In particular, a clear broadening of the electron temperature profile at the top of the pedestal ($\beta_N$<94%) is observed, as well as a strengthening and phase shift of the magnetic plasma response measured on the high field sidewall. These effects are illustrated in Fig. 2-17. Furthermore, rotation, which has long been observed to increase during ELM-suppressed states is found to drop just before the ELMs return, suggesting that the spin up is not simply a consequence of ELM suppression. These changes occur rapidly, within ~30 ms of a transition to/from an ELM-suppressed regime, relative to the 1 Hz frequency of the applied field rotation. The broadening of the electron temperature at the top of the pedestal and the accompanying changes to the magnetic response are consistent with island penetration in that region. It has been shown that the tearing response of the plasma is most likely in this region, where the electron rotation perpendicular to the magnetic field crosses zero [2].

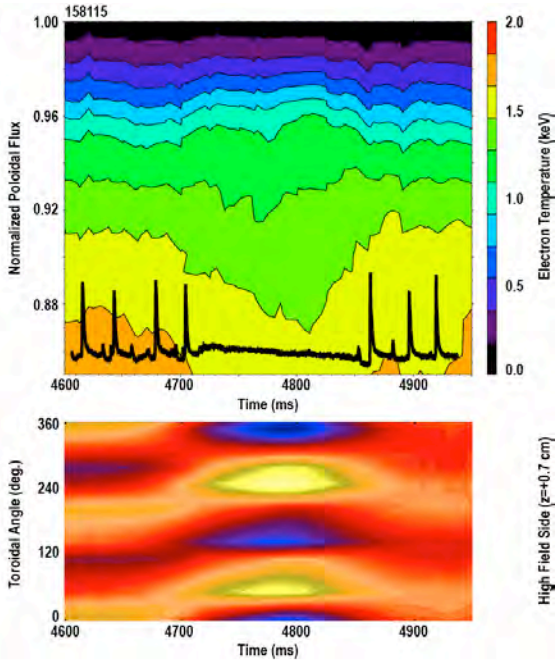


Fig. 2-17. (a) Contours of the electron temperature from Thomson scattering, as a function of $\beta_N$ and time, overlaid with a plot of $D_\alpha$ radiation showing ELMs (thick black line). (b) The tangential field due to the plasma response from the magnetic probes on the DIII-D high field side wall.

## 2.7 Nonlinearity of Plasma Response

The degree to which the plasma response can be accurately described by linear models has been a key point of inquiry. This question was raised after response linear and nonlinear calculations of DIII-D discharge 142603 were found to yield perturbed surfaces with noticeably different shapes. These differences are particularly evident along the high-field side, where linear modeling with IPEC, MARS, and M3D-C1 all show significantly larger normal displacements than does VMEC. A comparison of the perturbed $q$=8.5/3 surface as calculated by nonlinear, ideal VMEC modeling and linear, ideal MARS modeling is shown in Fig. 2-18. Furthermore, it was found that the linear displacements calculated by linear codes are large enough to imply the overlapping of mag-

netic surfaces in the edge for typical applied field magnitudes, indicating that the assumption of linearity there is being violated.

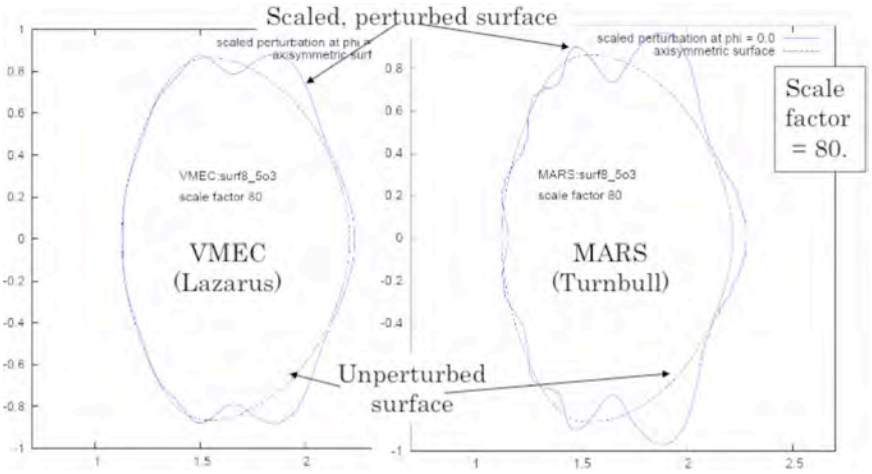


Fig. 2-18. Poloidal cross-sections of a DIII-D equilibrium, showing the perturbed and unperturbed $q$=8.5/3 flux surfaces predicted by VMEC and MARS-F in response to an applied $n$=3 perturbation. The amplitude of the perturbation is scaled up by a factor of 80 for visibility in each case.

Subsequent investigation has found that linear and nonlinear solutions for the displacement of the $q$=2.42 surface both calculated with the M3D-C1 code are in good agreement with each other, using 4 kA of I-coil current (Fig. 2-19). This suggests that the breakdown of the linear approximation does not contribute significantly to the disagreement between the VMEC and perturbative 3D equilibrium calculations. A potential cause of the disagreement is the absence of localized screening currents at low order rational surfaces in the VMEC solutions. This is supported by recent M3D-C1 calculations of 3D equilibria for rotating and nonrotating plasmas. The rotation leads to the persistence of localized currents at rational surfaces. There is a corresponding effect on the calculated displacement on the inboard side, with the amplitude of the displacement significantly larger in

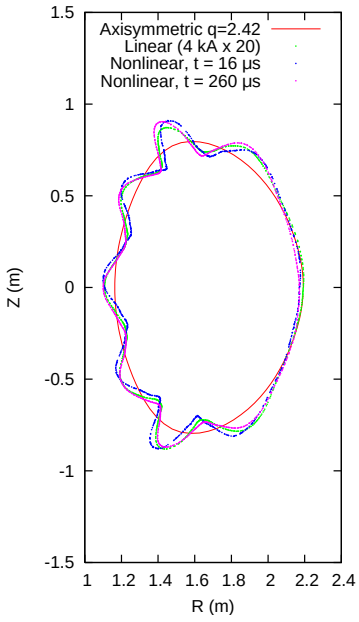


Fig. 2-19. Poincaré plots of the $q$=2.42 surface in a time-independent linear M3D-C1 calculation (green), and a time-dependent nonlinear M3D-C1 calculation at $t$ = 16 μs (blue) and $t$ = 260 μs (magenta). The field perturbations are calculated for 4 kA even-parity $n$=3 from the DIII-D I-coils. In these plots, the normal distance of the perturbed surfaces from the axisymmetric surface (red) has been multiplied by 20 to improve visibility.

the rotating plasma. Calculations with the NSTAB code provide further support for this picture. NSTAB is believed to have improved handling of localized currents relative to VMEC. The NSTAB calculations find a displacement amplitude on the inboard side significantly larger than that of VMEC, despite the fact that the NSTAB calculation is a fixed boundary calculation, imposing the VMEC boundary on the NSTAB calculation.

In one of the 3D response experiments conducted on DIII-D this year, the I-coil current was oscillated in an $n$=3 even parity configuration with a steadily increasing amplitude. (The oscillation is to allow a clear signal in the inductive probes.) As shown in Fig. 2-20, the plasma response measured by the magnetic probes is found to scale linearly with the I-coil field, up until at least 3 kA. Above this value, the response is found to deviate from linearity, but this is likely due to an error in the toroidal field programming in this discharge that caused a change in the axisymmetric equilibrium after $t$ = 5400 ms.

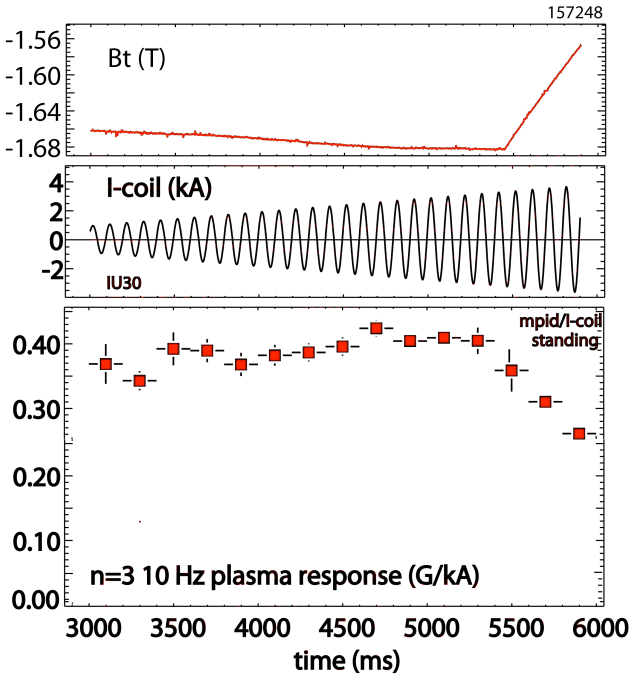


Fig. 2-20. (a) The toroidal field as a function of time in DIII-D discharge 157248. (b) The current in the upper I-coil. (c) The measured plasma response, normalized to coil current.

While the magnetic response appears to be accurately described by linear MHD in the regime considered here, there are clear instances where nonlinear physics becomes important. One example of this is mode locking and island penetration, which are discussed in Sec. 6. Another example is in the evolution of the axisymmetric profiles that results from the non-axisymmetric magnetic response, including braking and density pump-out. Pump-out, in particular, is observed to behave nonlinearly, exhibiting both an onset threshold and a nonlinear dependence on the applied field strength. These transport effects are discussed in Sec. 4.

### 2.8 Measurements of Edge Displacements

Displacements of the kinetic profiles near the plasma edge offer a useful way to measure the internal response. Previous studies on DIII-D have shown that these edge displacements may be 2 cm or greater in magnitude at the LFS midplane in response to typical applied non-axisymmetric fields [27]. Vacuum modeling of the perturbed fields generally predicts non-axisymmetric excursions of a few millimeters due to these applied fields, which is in rough agreement with measurements of $n$=3 response away from the mid-

plane [28]. Models including plasma response have successfully obtained quantitative agreement with DIII-D experimental measurements for $n$=1–3, both on the midplane and along the core Thomson chord ($R$ = 1.94 m) [29], highlighting the importance of the plasma response in this region. Furthermore, it was found that the radial and poloidal structure of the edge displacements imaged by the SXR camera on DIII-D were significantly different than would be predicted using vacuum fields together with a parallel thermal transport model. These structures were more accurately reproduced by MHD modeling, which essentially predicts the excitation of the least stable modes — in this case, edge-localized kink/peeling type modes.

Non-axisymmetric displacements result not only from the application of non-axisymmetric fields, but also through the effects of saturated MHD instabilities. Edge displacements have been measured with the multi-energy soft x-ray (ME-SXR) system on NSTX in the presence of both core-localized MHD and kink instabilities. The ME-SXR cameras have 1 cm radial resolution between channels near the plasma edge, and interpolation allows sub-cm resolution. An $n$=$m$=1 internal kink mode in plasmas with low-shear above $q$=1 has been found to couple to $m$/$n$=2/1 tearing modes, giving rise to islands of 10 cm, equating to 15% of the minor radius [17]. The position of the boundary in the presence of a 1/1 kink coupled to a 2/1 tearing mode, which can persist for half the length of the plasma discharge in NSTX. It was evident that the plasma boundary is distorted by ±7.5 mm, or ±1.3% of the minor radius.

Larger displacements are measured in the case of global MHD instabilities. High normalized beta plasmas often exhibit saturated global $n$=1 kink instabilities, or resistive wall modes, which can persist for long times in the presence of magnetic feedback [30]. While this low frequency mode activity is global and perturbs the plasma core, it also gives rise to significant shifts of the plasma boundary by ±0.95 cm, or ±1.6% of the minor radius, when there is a saturated $n$=1 RWM in high $\beta_N$ NSTX plasmas.

Finally, there is no correlation between the boundary displacement in the presence of such global $n$=1 instabilities and $\beta_N$ when the $n$=1 no-wall beta limit is exceeded. Figure 2-21 shows that the edge displacement is largely independent of $\beta_N$. This is not unexpected since it has been shown that the RWM stability depends sensitively on rotation and $l_i$ as well as $\beta_N$, and often plasmas at intermediate levels of rotation (i.e. neither the fastest nor slowest rotating cases in NSTX) have the least stable modes as the kinetic damping is minimized [24,30].

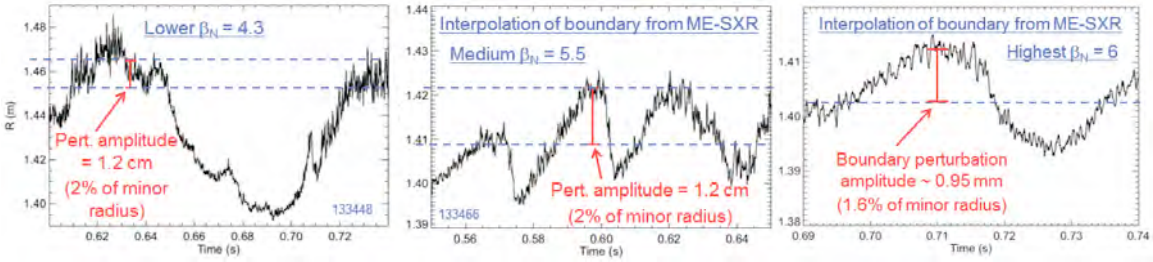


Fig. 2-21. The plasma boundary measured by the ME-SXR system in NSTX for a discharge with an $n$=1 RWM at $\beta_N$ less than the no-wall limit (a), intermediate $\beta_N$ (b), and for high $\beta_N$ above the no-wall limit (c).

## 2.9 Progress in Code Benchmarking and Validation

In order to validate codes and to investigate the importance of different physical effects on the plasma response, DIII-D discharge 153485, which has a well-measured magnetics response, was chosen for careful comparison between experimental data and modeling. Because the modeling results are particularly sensitive to the current density profile, three equilibrium reconstructions of DIII-D discharge $t$ = 4525 ms were produced, in which the bootstrap current was calculated using the Sauter formula multiplied by 0.82, 0.94, and 1.05, respectively, each giving edge current density profiles falling within the uncertainty of the experimental data. The plasma response to $n$=1 fields applied by 2 kA in the DIII-D I-coils was calculated using four codes: IPEC, M3D-C1, MARS-F, and VMEC. IPEC and MARS-F used linear, ideal models; M3D-C1 used a linear, resistive, two-fluid model; and VMEC used a nonlinear ideal model. IPEC, MARS-F, and VMEC each used an equilibrium that had been modified from the EFIT equilibrium by truncating the profiles at the $q$=4.631 magnetic surface using CORSICA. A comparison of the magnetics measurements of the $n$=1 plasma response (the total measured $n$=1 field minus the applied $n$=1 field) on the both the low-field wall and the high field sidewall with the code results is shown in Fig. 2-22.

MARS-F has also been applied to two equilibria at different times during a current ramp in DIII-D discharge 153480, finding good agreement with measurements. The results of these comparisons are shown in Fig. 2-23. The good quantitative agreement between the experimental data with and the linear, ideal MARS-F modeling suggests that linear, ideal MHD is sufficient in this case to accurately describe the magnetic response.

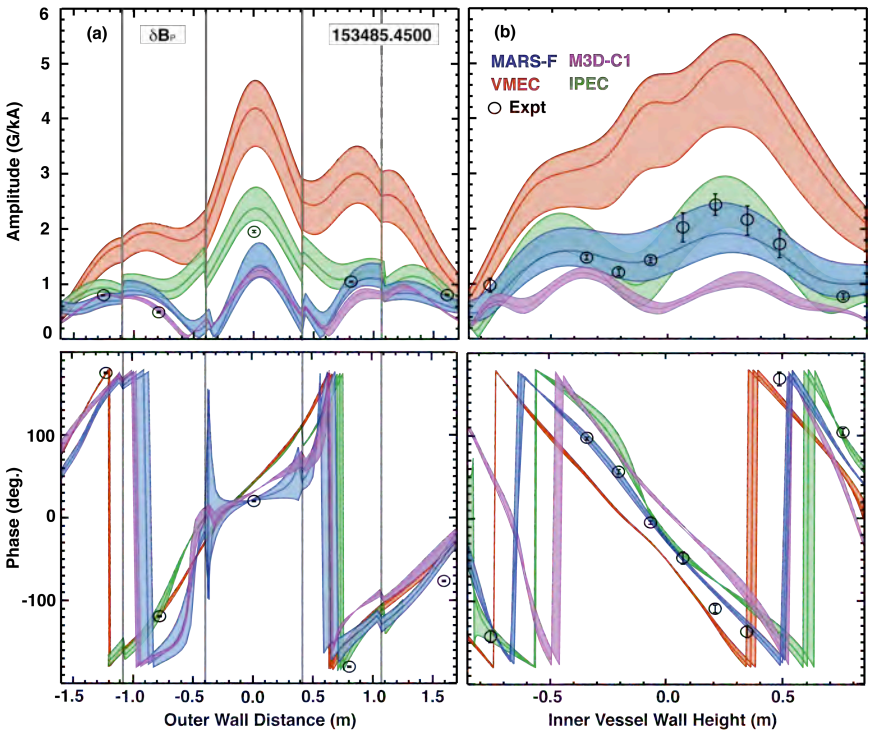


Fig. 2-22. The amplitude (top) and phase (bottom) of the tangential magnetic field from the $n$=1 plasma response as measured (black circles) and as calculated by four codes, along the low-field sidewall (left) and the high field sidewall (right). Equilibria with three different current density profiles within the experimental uncertainty were used to generate the three curves for each code.

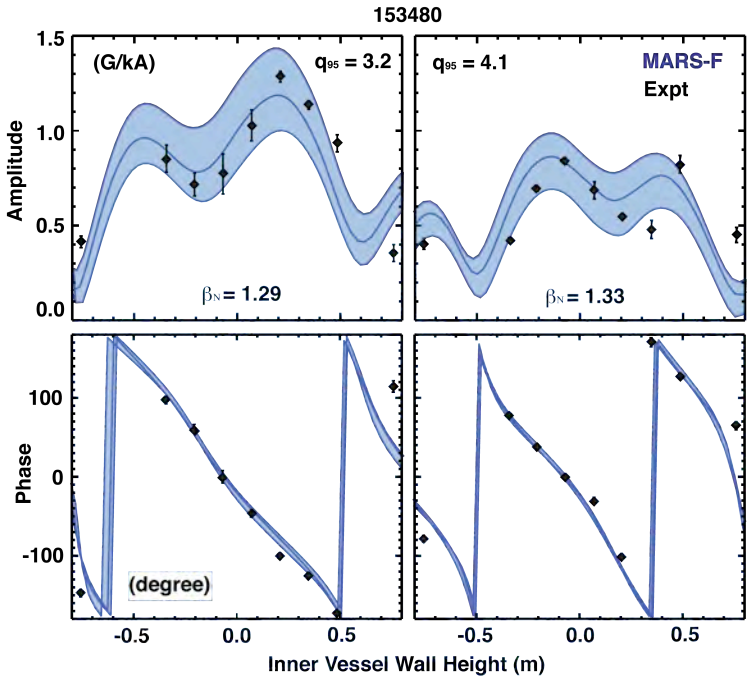


Fig. 2-23. The amplitude (top) and phase (bottom) of the vertical field from the $n$=1 plasma response as measured on the DIII-D high field sidewall (black diamonds) and as calculated by MARS-F, at two times during a current ramp for which $q_{95}$=3.2 (left) and $q_{95}$=4.2 (right).

In general, all of the codes find rough quantitative agreement within a factor of two of the experimental data. MARS-F, in particular, finds good quantitative agreement in both amplitude and phase with the experimental data in these discharges. Differences among the codes may be due to some extent to differences among their models; however, even codes that use the same physical model (MARS-F and IPEC) are found to yield somewhat different results. The reason for these discrepancies is under investigation. While the sensitivity of the results to the current density profile has been quantified to some extent by considering three different edge current profiles here, the sensitivity to other factors such as the rotation profile, resistivity profile, and transport parameters (e.g. viscosity, thermal conductivity) has not yet been systematically explored. Ultimately, systematic model variations of this kind may be used to determine the extent to which various features of the internal response (e.g. magnetic islands) may have a distinct signature on the magnetic probe data.

## References

[1] J.-K. Park, M.J. Schaffer, J.E. Menard, and A.H. Boozer, *Phys. Rev. Lett.* **99**, 195003 (2007).

[2] N.M. Ferraro, *Phys. Plasmas* **19**, 056105 (2012).

[3] S.C. Jardin, N. Ferraro, X. Luo, J. Breslau, K.E. Jensen, and M.S. Shephard, *J. Phys, Conf. Ser.* **125,** 012044 (2008).

[4] Y.Q. Liu, A. Bondeson, C.M. Fransson, B. Lennartson, and C. Breitholts, *Phys. Plasmas* **7**, 3681 (2000).

[5] P.R. Garabedian, *Proc. of the National Academy of Sciences* **103**, 19232 (2006).

[6] S.P. Hirshman and J. C. Whitson, *Phys. Fluids* **26**, 3553 (1983).

[7] P.B. Snyder, *et al., Phys. Plasmas* **9**, 2037 (2002).

[8] J.D. King, *et al., Rev. Sci. Instrum*. **85**, 083503 (2014).

[9] M.W. Shafer, *et al., Rev. Sci. Instrum*. **8**1, 10E534 (2010).

[10] S.A. Sabbagh, *et al., 23rd IAEA Fusion Energy Conference*, Daejeon, Republic of Korea, 2010, paper EXS/5-5.

[11] S.A. Sabbagh, *et al., Proc. of the 37th European Conference on Plasma Physics, Dublin, Ireland*, 2010 (EPS, Petit-Lancy, Switzerland) paper P4.160.

[12] A.H. Boozer, *Phys. Plasmas* **10**, 1458 (2003).

[13] M.J. Lanctot, *et al., Phys. Plasmas* **17**, 030701 (2010).

[14] S.A. Sabbagh, *et al., Nucl. Fusion* **46**, 635 (2006).

[15] A.M. Garofalo, T.H. Jensen, and E.J. Strait, *Phys. Plasmas* **10** (2003) 4776

[16] J.-K. Park, *et al., Phys. Plasmas* **16**, 082512 (2009).

[17] J.E. Menard, *et al., Nucl. Fusion* **45,** 539 (2005).

[18] A.H. Boozer, *Phys. Rev. Lett.* **86**, 5059 (2001).
[19] H. Reimerdes, *et al.*, *Nucl. Fusion* **45**, 368 (2005).
[20] M.P. Gryaznevich, *et al.*, *Nucl. Fusion* **52**, 083018 (2012).
[21] S.A. Sabbagh, *et al.*, *Nucl. Fusion* **53**, 104007 (2013).
[22] H. Reimerdes, *et al., Phys. Rev. Lett*. **93**, 135002 (2004).
[23] B. Hu and R. Betti, *Phys. Rev. Lett.* **93**, 105002 (2004).
[24] J.W. Berkery, *et al., Phys. Rev. Lett.* **104**, 035003 (2010).
[25] H. Reimerdes, *Phys. Rev. Lett.* **106**, 215002 (2011).
[26] M.J. Lanctot, *et al.*, *Nucl. Fusion* **53**, 083019 (2013).
[27] R.A. Moyer, *et al., Nucl. Fusion* **52**, 123019 (2012).
[28] D.M. Orlov, *et al., Nucl. Fusion* **54**, 093008 (2014).
[29] N.M. Ferraro, *et al., Nucl. Fusion* **53**, 073042 (2013).
[30] S.A. Sabbagh, *et al., Nucl. Fusion* **50**, 025020 (2010).

# 3. Correction of Higher Toroidal Mode Number Error Fields and Limitations of the Single-Mode Model

## 3.1 Introduction and Motivation

Recent theoretical advances in understanding the plasma response to non-axisymmetric fields have shown that the response driven by external coils can be represented as a hierarchy of stable modes, found through singular value decomposition (SVD) [1–3] Strong (order of magnitude) separation of singular values is usually found, with the first SVD mode is termed the `dominant' mode and all SVD modes being orthogonal to one another. The strong singular value separation implies that the secondary modes can be ignored, effectively rendering the plasma sensitive only to the degree of coupling to the dominant mode, which is a scalar property of an applied 3D spectrum at each toroidal mode number $n$.

Experimental assessment of the degree to which the plasma is sensitive only to the dominant mode is of critical importance to understanding the limits of error field correction (EFC), as a strong performance recovery can be expected after coupling to the dominant mode is nulled by a set of EF correction coils. Furthermore, the ease of nulling dominant mode coupling means similar performance should be expected for any reasonable geometry of EFCC, specifically both in- and ex-vessel.

Previous experiments at DIII-D have demonstrated that several key $n$=1 field sensitivities are directly related to their coupling to this dominant mode of the plasma, and concomitantly that the plasma is remarkably insensitive to $n$=1 fields which have no net coupling to this mode [4]. Specifically, plasma rotation and EF penetration thresholds were nearly unchanged despite application of large amplitude probing fields with no dominant mode coupling. Fields with no net coupling are here termed “orthogonal” to the dominant mode. These results are summarized in Fig. 3-1, showing $n$=1 results in a variety of plasma regimes.

These results motivate a companion study using $n$=2 fields, which was conducted during the timeframe of the JRT and is discussed in this Chapter. Experiments are conducted both by applying a known $n$=2 “proxy” EF with the DIII-D ex-vessel coilset and correcting it with the in-vessel coil set, as well as by applying a localized magnetic perturbation with the Test Blanket Module mockup coils. Experiments contrasted plasma sensitivity with applied fields calculated to have maximized and nulled coupling to the IPEC dominant mode.

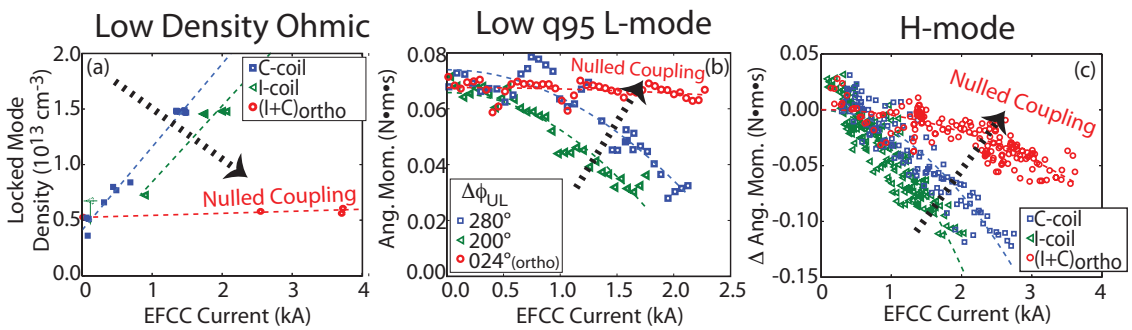


Fig. 3-1. Summary of $n$=1 sensitivities as dominant-mode coupling is nulled in various regimes. (a) Ohmic regime error field penetration, (b) Low $q_{95}$ rotation braking, and (c) co-rotating H-mode rotation braking are all strongly reduced minimized when coupling is nulled.

In this study optimal $n$=2 in-vessel EFC currents will be shown to be consistent with those calculated to minimize the volume integrated neoclassical toroidal viscosity torque $T_{NTV}$ using ideal MHD (IPEC) plasma response calculations [5]. However, unlike $n$=1, the degradation of angular momentum introduced by the proxy EF cannot be recovered through optimal $n$=2 correction. This imperfect performance recovery demonstrates the importance of multiple components of the $n$=2 response and is inconsistent with only a single SVD mode being dominant. Unlike angular momentum, density pumpout was found to be avoided when dominant mode coupling was nulled. This demonstrates that through precise spectral control (forming the "orthogonal" field), particle and momentum transport can be decoupled.

### 3.2 Experimental Setup

This experiment uses a lower single-null ITER-similar shape H-mode scenario, shown in Fig. 3-2(a). For this equilibrium normalized current $I_N$=1.12, normalized pressure $\beta_N \approx 2.0$, and safety factor $q_{95}$=4.3. Co-neutral beam injected power of 4.2 MW and torque of 3.3 N·m yields robust toroidal rotation and a plasma tolerant to the large imposed proxy EF, facilitating EF measurement. Pedestal electron collisionality $\nu^* \approx 0.33$ is fairly low, allowing large neoclassical toroidal viscosity torques ($T_{NTV}$) to be driven by the $n$=2 fields.

The geometry of the in-vessel "I-coils" and ex-vessel "C-coils" is also shown in Fig. 3-2(a). As the coilset geometry is very dissimilar, so too is the spectrum of their applied fields. To analyze the spectrum, Fourier decomposition is performed using the SURFMN code [6], with Fig. 3-2(b) displaying the computed poloidal spectra near the plasma boundary for both coil sets used in this work. Coil set fields are normalized to 1 kA in the leads. The C-coil spectrum is dominantly low $|m|$ due to its distance from the plasma, while the I-coil spectrum displays more definition. The I-coil is hard-wired to equal toroidal phase between upper and lower rows (even parity). This hardwiring is

chosen to maximize coupling to the coupling to the IPEC dominant mode of the plasma, as will be described.

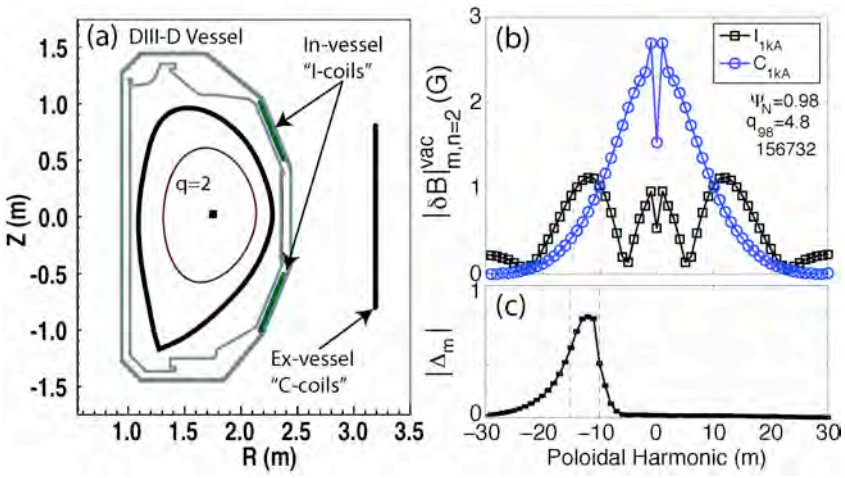


Fig. 3.2. (a) Plasma shape and geometry of the in-vessel (I) and ex-vessel (C) coil sets which generate the $n$=2 perturbations used in this study. (b) $n$=2 poloidal spectrum of the in- and ex-vessel DIII-D coil sets. The in-vessel coils are hardwired in an even parity configuration. Coupling is computed by the inner product of the poloidal spectra ($\delta B^{vac}_{m,n}$) with the coupling vector ($\Delta_m$) shown in (c).

A key output of the IPEC code [1,7] is the coupling of the external field to the resonant surfaces of the plasma. IPEC calculates the coupling from the external field to each resonant surface, then performs a SVD on the coupling to all rational surfaces, and outputs the field patterns of each SVD mode. The first left-singular vector ($\equiv\Delta_m$), shown in Fig. 3-2(c) represents the "dominant mode" which dominates the coupling. The second left-singular vector is the sub-dominant mode, to which coupling can also be calculated. The singular value separation is over ten-fold for this equilibrium, indicating IPEC predicts a weak role for the sub-dominant modes. The degree of coupling to the dominant mode of the $n$=2 IPEC response is a scalar property of any given $n$=2 spectrum, and is calculated by forming the inner product (in $m$) of the applied spectrum ($\delta B^{vac}_{m,n}$) with the coupling vector ($\Delta_m$) [8],

$$overlap \equiv \delta B^{vac}_{m,n=1}\,\Delta_m \qquad (1)$$

and is denoted the "overlap"of the applied field with the IPEC dominant mode.

### 3.3 Determination of Optimal Currents

Determination of optimal currents is achieved by scanning the I-coil field with and without the imposed C-coil proxy EF. Cases without the proxy EF are needed as the DIII-D tokamak is known to possess a significant $n$=2 intrinsic EF, which must be subtracted from the proxy measurement. Several discharges are used in each scan dataset, and representative discharges are shown in Fig. 3-3. Slowly scanning the I-coil currents [shown in Fig. 3-3(c,d)] yields clear responses across many global ($n$=0) parameters, with line-averaged density ($\langle n_e \rangle$), normalized pressure ($\beta_N$), and total angular momentum ($L_\phi$) shown in Fig. 3-3(e,f). These n=0 parameters are fit on the space defined by $\mathbf{I}_C$, the $n$=2 magnitude and phase of the I-coil currents, as will be discussed. Figure 3-3(f) also previews a key result of this study: the $L_\phi$ degradation introduced by the ex-vessel proxy is not recovered at any value of I-coil current, while density pumpout is recovered ($\langle n_e \rangle$).

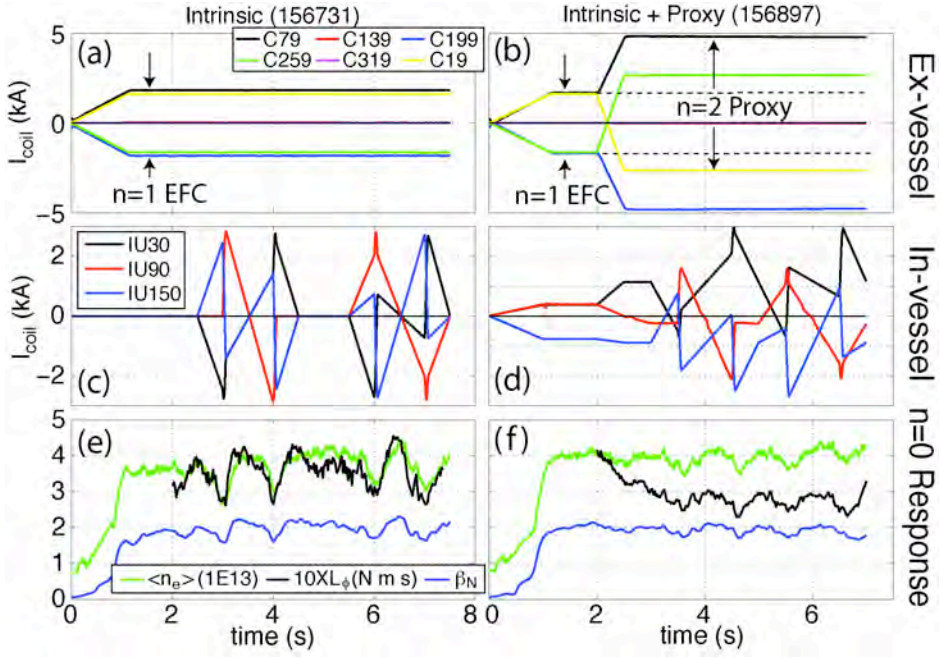


Fig. 3-3. Time-domain representation of discharges used to measure $n$=2 optimal correction currents ($\mathbf{I}_{opt}$) with and without the C-coil "proxy" EF. (a,b) Displays C-coil currents, which provide $n$=1 EFC and potentially an $n$=2 proxy EF. (c,d) Displays scans of I-coil currents to measure $\mathbf{I}_{opt}$, by fitting to the $n$=0 responses shown in (e,f).

#### 3.3.1 Assessment via total angular momentum

A simple ad-hoc model is used to fit the total angular momentum ($L_\phi$) to the I-coil current amplitude and phase ($\mathbf{I}_C$), given below:

$$L_\phi = \alpha \left| I_C - I_{opt} \right| + L_{\phi,0} \qquad (2)$$

where $L_\phi$ is calculated utilizing the measured $n_e$ and carbon $V_\phi$ profiles and reconstructed equilibrium geometry. While this relationship does not employ the nominal quadratic dependence on $\mathbf{I}_C$ [9], experimental data with $n$=2 fields exhibit a strikingly linear degradation, thus motivating this empirical functional form for the fitting. The quadratic dependence may be absent because the $n$=2 field strongly reduces $\beta_N$ which in turn reduces plasma sensitivity to the $n$=2 field. Assuming sensitivity is linearly dependent on $\beta_N$, this would reduce the quadratic relationship to a linear one.

Experimental fits to Eq. (2) and data assessment is shown in Fig. 3-4 for datasets with and without the C-coil proxy EF. Each scan contains several discharges, which slowly scan a wide range in $\mathbf{I}_C$. As injected torque is high, the plasma is robust to the $n$=2 fields and can tolerate the significant deviations from optimal correction employed to constrain the fits. Plots of measured $L_\phi$ on the I-coil $n$=2 phase space ($\mathbf{I}_C$), shown in Fig. 3-4(a,b) for cases with and without the proxy, show degradation of $L_\phi$ away from the optimal point, as well as a significant difference in the optimal currents ($\mathbf{I}_{opt}$) with and without the proxy. The change in $\mathbf{I}_{opt}$ indicates that the I-coil is capable of at least partially correcting the C-coil spectrum, despite poorly matched spectra. Figure 3-4(e,f) represents the same data in one dimension, with the X- and Y- components of $\mathbf{I}_C$ plotted as $L_\phi$ evolves. Also plotted in Fig. 3-4(c,d) are the $L_\phi$ prediction from the fit to Eq. (2) and the residual, which generally indicates a good quality of fit. Note also data from multiple discharges is plotted without re-normalization, indicating shot-to-shot repeatability is adequate for this measurement.

Angular momentum data from the intrinsic and intrinsic+proxy EF datasets is now plotted against the I-coil current magnitude away from $\mathbf{I}_{opt}$ in Fig. 3-5. As can be seen, the $L_\phi$ values without the proxy are never recovered after the proxy EF is introduced, despite the new optimal current level found. This imperfect recovery should be contrasted with the various scans of Fig. 3-1, where strong performance recovery was found for $n$=1 fields. Imperfect recovery is suggestive of multiple components, or modes, of the plasma response and will be further discussed in Sec. 3.5.

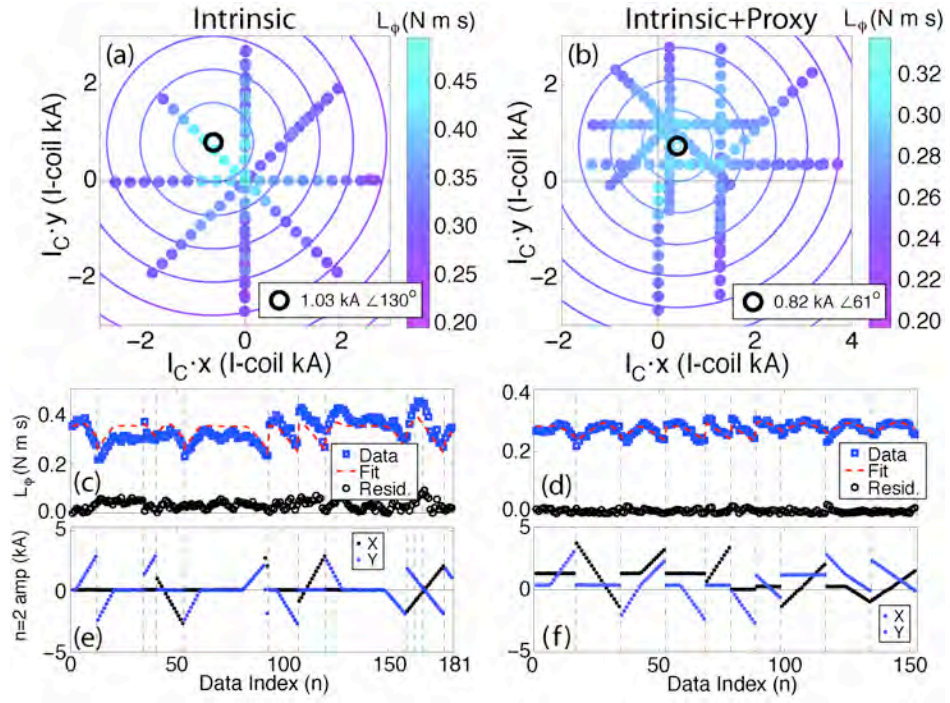


Fig. 3-4. Determination of $n$=2 $\mathbf{I}_{opt}$ by optimization of $L_\phi$. (a,b) Display $L_\phi$ data on the $\mathbf{I}_C$ phase space of the $n$=2 coil currents. Also plotted are contours of fitted $L_\phi$ using Eq. (2), with the center defining $\mathbf{I}_{opt}$ (black circle). (c,d) Display of $L_\phi$ vs fitted result and residual. (e,f) X-Y coordinates of $\mathbf{I}_C$ at each point in fit.

While complete performance recovery was not achieved after introduction of the $n$=2 C-coil proxy EF, Fig. 3-4(a,b) does show a modification of $\mathbf{I}_{opt}$ by the proxy EF. The part of $\mathbf{I}_{opt}$ needed to correct the proxy is determined by subtracting the $\mathbf{I}_{opt}$ of the intrinsic only dataset from the intrinsic+proxy dataset, thus isolating the proxy component as shown in the inset of Fig. 3-6. The proxy contribution is compared to modeling in Fig. 3-6, indicating that the experimental $\mathbf{I}_{opt}$ are near to those computed to null the IPEC dominant mode coupling. Thus, the residual spectrum after correction of the C-coil proxy by the I-coil closely resembles the pre-calculated "orthogonal" field. Further modeling of $T_{NTV}$ by the PENT code [5] is also consistent with both the SVD1 null and $\mathbf{I}_{opt}$. This is consistent with previous work on NSTX in which $n$=3 $\mathbf{I}_{opt}$ was found to minimize $T_{NTV}$ [10]. While the SVD1 null is perfect, a residual $T_{NTV}$ is found at the optimum which

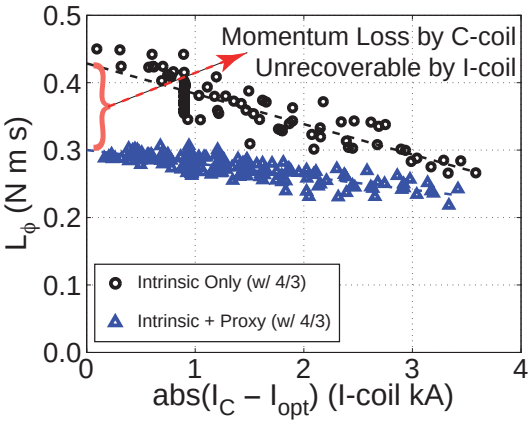


Fig. 3-5. Dependence of $L_\phi$ on I-coil current with and without the C-coil proxy EF. The degradation introduced by the C-coil is not recovered even with optimal I-coil correction.

partially explains the incomplete performance recovery. The importance of the "orthogonal" field and the residual braking will be directly explored in Sec. 3.5.

### 3.3.2 Assessment via other *n*=0 parameters

While optimization based on $L_\phi$ provides a good measurement of $\mathbf{I}_{opt}$, Fig. 3-3 shows other global parameters (such as $\beta_N$ and $\langle n_e \rangle$) are also strongly affected by the *n*=2 field and thus can also be used as optimization param-eters. Fits to $\beta_N$ and $\langle n_e \rangle$, as well as $L_\phi$ for the discharge of Fig. 3-3(b) is shown in Fig. 3-7. As can be seen, the difference between the fitted $\mathbf{I}_{opt}$ for each optimization parameter is small. Interestingly, agreement with the IPEC calculation shown in Fig. 3-6 would actually be improved by using these alternate parameters. Uncertainty is assessed by also plotting the fit to each parameter enforcing the optimum to be that of $L_\phi$ [green dashed line in Fig. 3-7(b)], indicating a very small difference in fitted behavor. Thus, the differences in the optimal currents between these different optimization parameters is likely within experimental uncertainties.

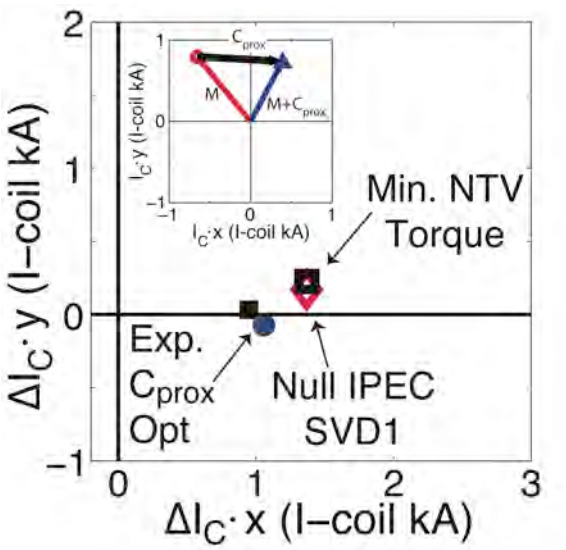


Fig. 3-6. Comparison of optimal *n*=2 currents with field structure analysis on the $\mathbf{I}_C$ phase space. Experimental $\mathbf{I}_{opt}$ are within 20% of the predicted IPEC dominant mode null and the integrated $T_{NTV}$ minimum. The inset shows the subtraction of optimal currents with intrinsic only (M) and with the intrinsic and without the known proxy field, isolating the contribution from the proxy.

## 3.4 Direct Examination of Orthogonal Field

### 3.4.1 Experimental observations

Having confirmed in Sec. 3.3 the validity of the IPEC dominant mode to determining optimal correction currents for *n*=2 fields, a direct assessment of the *n*=2 orthogonal field (termed $(I+C)_{ortho}$) is now presented. The orthogonal field is that which is pre-calculated to have zero coupling to the IPEC dominant mode [as per Eq. (1)] and is formed by superimposing I-coil and C-coil fields. Equivalently, this field can be defined as the I-coil $\mathbf{I}_{opt}$ superimposed on the C-coil proxy EF, so long as the I-coil intrinsic EF contribution to $\mathbf{I}_{opt}$ is subtracted. The orthogonal field is contrasted to a field which has "maximum" coupling [termed $(I+C)_{max}$], as defined by inverting the polarity of the I-coil currents relative to the orthogonal field, such that individual coil set overlaps add instead of cancel. The poloidal spectra for these fields are shown in Fig. 3-8(a), and are compared

to a C-coil only spectrum. Due to the poor spectral match between coil sets, the modification of the poloidal spectrum required to null coupling is limited to the high |m| wings, while the bulk of the spectrum is left unchanged. Computed dominant mode coupling (overlaps) are shown in Table I, showing a strong ordering, as well as the total field power by Parseval's theorem, which actually increases when forming the $(I+C)_{ortho}$ field.

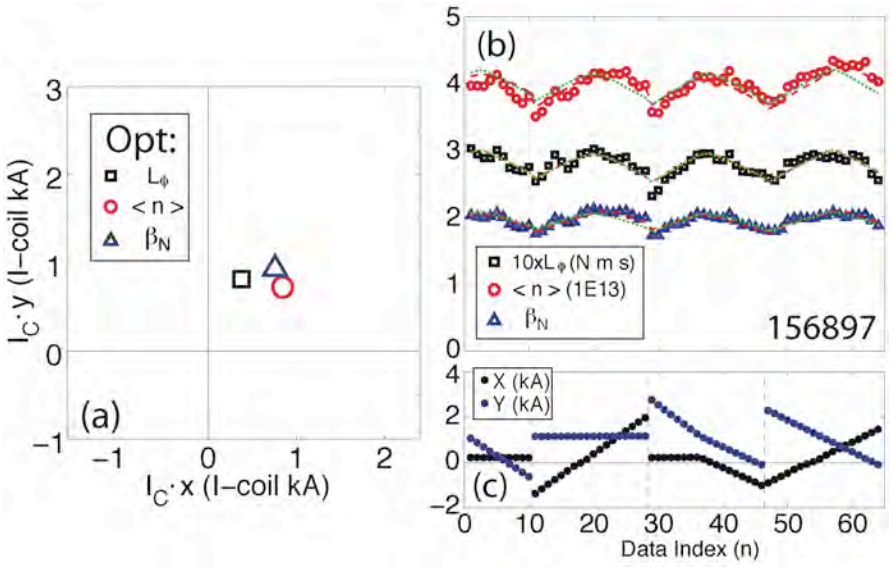


Fig. 3-7. (a) Comparison of $\mathbf{I}_{opt}$ found through optimization of other $n$=0 parameters for the discharge of the proxy dataset shown in Fig. 3-3. (b) Assessment of each parameter along with fit prediction (red dashed line). The green dashed line is the prediction assuming the optimum was unchanged from that found via $L_\phi$. (c) Plots coordinates of $\mathbf{I}_C$ during this discharge.

Despite modest modification to the applied spectrum, strong $n$=0 response differences are seen. While the $(I+C)_{max}$ spectrum drives transport in all channels, the $(I+C)_{ortho}$ spectrum does not materially affect pumpout and confinement, though $L_\phi$ is still significantly reduced. This is consistent with the observations in the proxy EF dataset presented in Sec. 3.3, where for no value of I-coil current could the momentum degradation be recovered, though particle and energy confinement was restored. Note the changes in the pumpout are consistent with coupling to the resonant surfaces (also proportional to the IPEC dominant mode) driving particle transport in this scenario. In contrast, momentum degradation must also arise from additional components of the $n$=2 field. Interestingly, the effect of the $(I+C)_{ortho}$ field is likely a pure observation of non-resonant braking, despite the application of large $m=nq$ vacuum field components.

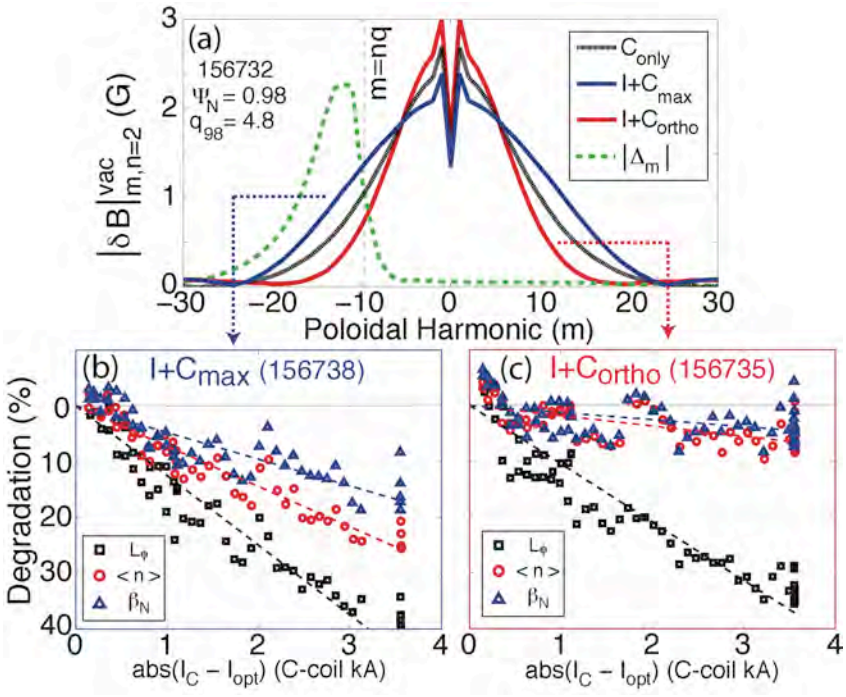


Fig. 3-8. Comparison of global plasma sensitivity to combinations of in- and ex-vessel $n$=2 fields with maximized [$(I+C)_{max}$] or nulled [$(I+C)_{ortho}$] coupling to the IPEC dominant mode, given by the dot product of $\delta B^{vac}_{m,n}$ with $\Delta_m$. While the $(I+C)_{max}$ spectrum (b) strongly drives transport in all channels, the $(I+C)_{ortho}$ spectrum (c) does not affect pumpout or confinement, though braking is still found.

### 3.4.2 Comparison to NTV Modeling

**Table I. Comparison of Coupling to the IPEC Dominant Mode (denoted overlap) and Total Field (by Parseval's Theorem) for each *n*=2 Poloidal Spectrum shown in Fig. 3-2.**

| Spectrum | Overlap (au/kA) | $\sum\left(\delta B^{vac}_m\right)^2$ $(G/kA)^2$ |
|---|---|---|
| C-coil | 0.417 | 47.6 |
| $(I+C)_{max}$ | 0.848 | 34.9 |
| $(I+C)_{ortho}$ | 0.006 | 70.7 |

The disparate sensitivities found between the spectra of Fig. 3-8 are simulated by the IPEC-PENT code to assess the degree to which modeling captures the observation. Figure 3-9 displays the computed integrated NTV torque profile for the spectra of Fig. 3-8 using representative experimental kinetic profiles. IPEC-PENT predicts a strong ordering of the total $T_{NTV}$, consistent with the degree of coupling to the IPEC dominant mode. However, within the core of the plasma ($\Psi_N$<0.9) the $(I+C)_{ortho}$ field actually drives the largest $T_{NTV}$, whereas the dominant mode coupling is found to predominantly control the torque originating from the edge. $T_{NTV}$ driven from the core of the plasma, driven by the low |m| harmonics may provide a mechanism for the unrecoverable $L_\phi$ degradation [note absence of low $|m|$ harmonics in the I-coil spectrum of Fig. 3-2(b)], though admittedly IPEC-PENT does calculate this contribution to be small. Similar core-edge discrepancies were found in PENT simulations of orthogonal

*n*=1 fields, though for *n*=1 the $(I+C)_{ortho}$ field drove weak braking, consistent with PENT modeling [4].

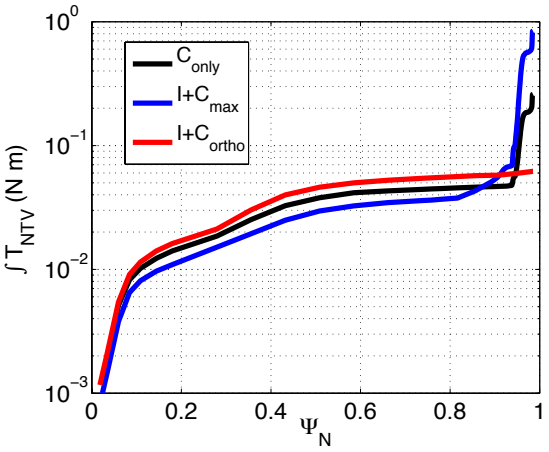


Fig. 3-9. IPEC-PENT modeling of the integrated $T_{NTV}$ radial profile for the spectra of Fig. 3-8. Within the core, slightly larger $T_{NTV}$ is driven by the $(I+C)_{ortho}$ field while the edge $T_{NTV}$ goes like the IPEC dominant mode coupling.

### 3.5 Compensation of a Local Error Field Test Blanket Module Mockup

Experiments with the DIII-D Test Blanket Module (TBM) mockup coils also suggest that nulling the dominant component of an error field, while very important, may not completely remove the effects of the error field. The TBM mockup was designed to investigate the effects on plasma perform-ance of magnetic field perturbations similar to those that would be encountered from the ITER Test Blanket Modules, and to investigate requirements for compensation of those perturbations. A more comprehensive review of recent TBM experiments is found in Ref. [11].

Results from multi-coil, multi-mode error field correction experiments show that the performance of *n*=1 error field correction strategies improves as the plasma pressure increases and the dominant *n*=1 plasma mode becomes more unstable. This is consistent with the hypothesis that the increase in the TBM-induced confinement degradation with plasma pressure is due to *n*=1 field amplification of the TBM field by the plasma. However, *n*=1 correction does not fully remove the effects of the TBM field on plasma rotation. A preliminary experiment to test correction of *n*>1 components of the TBM field did not further reduce the TBM torque over optimized *n*=1 error field correction. Future experiments will continue to study *n*>1 error field coil (EFC) approaches in order to understand his result.

#### 3.5.1 TBM compensation with *n*=1 control fields

Motivated by initial success in correction of the TBM induced error field in low-density L-mode plasmas [12], a set of experiments in 2011 evaluated the effectiveness of TBM error field correction in ITER baseline relevant ELMy H-mode plasmas [13]. The error field correction currents are optimized using a non-disruptive technique that maximizes the toroidal angular momentum of the plasma.

Despite extensive optimization of the plasma rotation and elimination of the *n*=1 plasma response at the midplane, it was found that *n*=1 EFC is only partially successful at avoiding the TBM-induced rotation degradation at the ITER $\beta_N$ target of 1.8 [14].

Contrary to earlier analysis [12], this suggests higher toroidal harmonic contributions to the TBM torque may be significant to correct. Further, the ability of $n$=1 EFC to eliminate the $n$=1 plasma response suggests that it should be possible to completely avoid the deterioration of confinement with increasing beta [12] if it holds that the degradation is due solely to the amplification of the $n$=1 component of the TBM error.

This hypothesis was tested at high beta by optimizing the plasma rotation using either the I-coil (as above), or the C-coil, an ITER-like ex-vessel coil. Similar to the early TBM experiments, TBM effects on confinement reach the 15%–20% level for $\beta_N$~2.75, outer gap of 6 cm, and TBM current of 1.1 kA. However, restrictions on heat loads to plasma facing components in DIII-D has required operation with a larger plasma-wall gap. A 1 cm increase of the gap reduces TBM effects to below 10%. Control room analysis is used to identify the optimal EFC currents, and the resulting improvement of performance is assessed by ramping up the control field with the TBM field, Figs 3-10 and 3-11.

In both cases, $n$=1 EFC is capable of

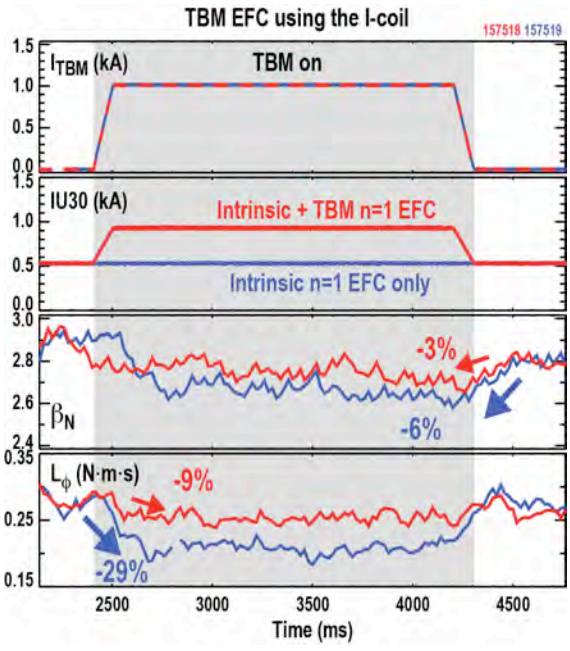


Fig. 3-10. Error field correction of both the intrinsic magnetic field errors (blue) and the TBM error field (red) using an in-vessel coil shows that plasma performance (denoted by $\beta_N$) drops by only 3% when error field corrections are optimized. The total angular momentum of the plasma ($L_{tot}$) is reduced by only 9% with optimized error field correction.

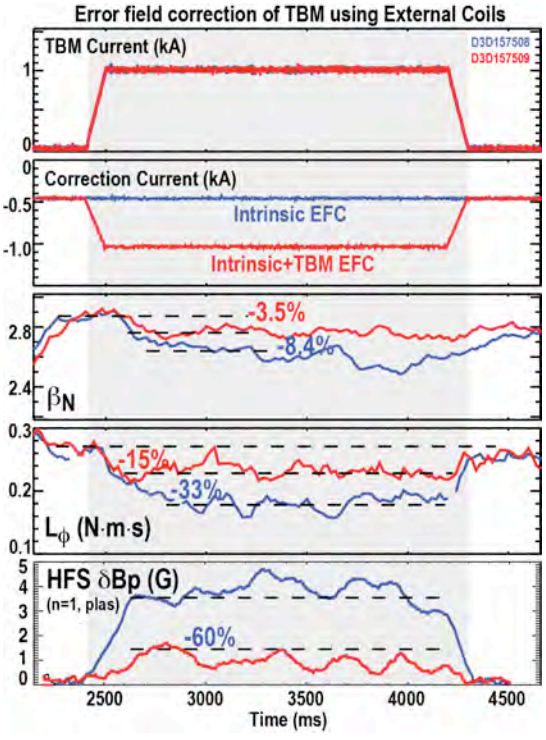


Fig. 3-11. Same as Fig. 3-10 except $n$=1 EFC is applied using ex-vessel coils (C-coil). Also, the evolution of the $n$=1 magnetic plasma response at the midplane (bottom) shows a reduction of 60% with EFC compared to the uncorrected case.

recovering over 60% of the TBM-induced performance degradation as measured using $\beta_N$ and $L_\phi$, which is a factor of 2 improvement over the recovery at lower $\beta_N$ [14]. Also, the degradation of $\beta_N$ is reduced to the 3% level, the same level observed at lower pressures. This suggests $n$=1 field ampli-fication is responsible for a dominant fraction of the confinement degradation increase with beta. Performance with in-vessel and ex-vessel coils is similar with slightly better performance recovery found with in-vessel coils. However, this may be due to a slight reduction in $\beta_N$ in discharge 157518, which was used to assess $n$=1 EFC of the TBM with the I-coil. Unlike the results at lower beta, the $n$=1 plasma response was not entirely cancelled, Fig. 3-11(bottom), indicating room for further improvement in performance.

### 3.5.2 TBM compensation with n=2 control fields

Contrary to the early modeling results, more recent calculations using the IPEC-PENT code [5] indicate that the NTV torque spectrum has significant contributions from $n$>1 harmonics, Fig. 3-12, with the $n$=1 component only 145% of the $n$=2 component (rather than 2 orders of magnitude larger). IPEC is used to get the perturbed magnetic fields and the PENT code is used to calculate the NTV torque in full toroidal geometry. Recent benchmarks between IPEC-PENT, MARS-K, and the MISK code show good agreement leading to increased confidence in this recent result [15]. Note that the drastic difference compared to the previous analysis is now thought to be due mainly to the low $q$-shear around the magnetic axis leading to a large plasma response there whereas the recently considered case had a monotonic $q$ profile with $q_0$>1.

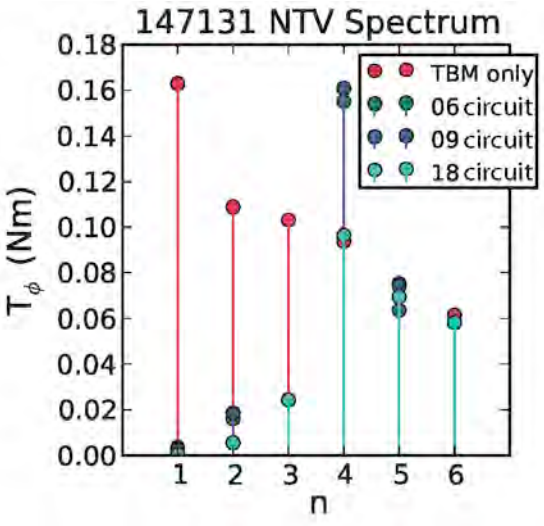


Fig. 3-12. Predicted NTV torque from IPEC-PENT modeling of DIII-D discharge 147131 for TBM alone and with I-coil EFC of the TBM for various circuit combinations allowing reduction of the NTV torque from $n$=1,2 and 3 harmonics.

Contrary to the IPEC-PENT results, little benefit of $n$>1 EFC of the TBM has been observed experimentally. This is demonstrated by applying optimized $n$=2 fields using a single I-coil array (the upper one) in addition to optimized $n$=1 EFC with the C-coil, Fig. 3-13. Discharge 157527 has both $n$=1 and $n$=2 EFC of the TBM; however, the $n$=2 EFC did not reduce the degradation in $\beta_N$ or the angular momentum over $n$=1 EFC of the TBM alone as in 157529. No EFC of the TBM is used in 157530. Various effects that may clarify this result are presently under study including the role of multiple $n$=2 plasma

modes, the impact of the $n$=2 control field on the $n$=1 plasma response, and the interaction of the TBM field with the intrinsic $n$=2 error field.

### 3.5.3 Discussion

Multi-coil, multi-mode error field correction experiments show that understanding of the plasma's magnetic response is important for minimizing the effects of the TBM's perturbation to the magnetic field. As $\beta_N$ increases so does the TBM-induced degradation of particle and energy confinement, as a result of the plasma's increasing magnetic response. Fortunately, the capability of $n$=1 EFC also increases with $\beta_N$ allowing recovery of high performance with TBM fields using either in-vessel or ex-vessel correction coils (a favorable result for ITER as the error field correction strategy is based solely on correction of $n$=1 error fields using ex-vessel coils). However, at the ITER $\beta_N$ target, $n$=1 EFC of the TBM field provides only a partial (~25%) recovery of the plasma rotation despite minimizing the entire $n$=1 magnetic plasma response, suggesting that other toroidal harmonics may also play a role.

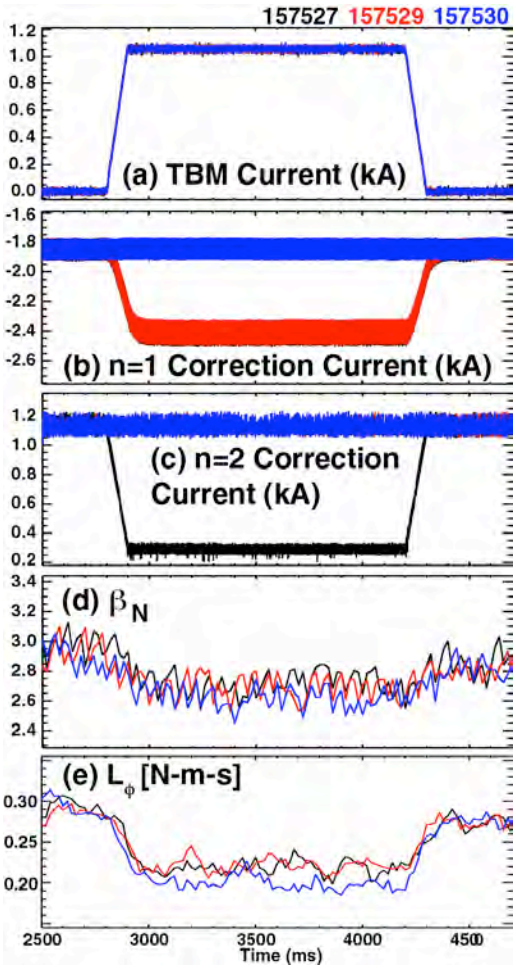


Fig. 3-13. Impact of error field correction of the (a) TBM field using (b) $n$=1 ex-vessel coil, (c) $n$=2 in-vessel coil on $\beta_N$ and L$\phi$. Optimized $n$=1 and 2 EFC of TBM (black) did not improve plasma performance beyond that obtained with $n$=1 EFC alone (red). The blue traces are the case with no EFC of the TBM field.

In an initial experiment, correction of $n$=2 components of the TBM field using a compensation field with a fixed poloidal spectrum did not further reduce the TBM torque over optimized $n$=1 error field correction. This result may be consistent with the "C-coil proxy" experiments described earlier in this section, which also found that $n$=2 compensation with a poorly matched poloidal spectrum could not fully eliminate the torque of an $n$=2 error field. Further experiments are planned to clarify the physics of $n$=2 error fields and their compensation, including the possible roles of sidebands of the compensation fields, multiple stable $n$=2 modes, or non-resonant braking.

### 3.6 Discussion and Conclusion

Recent experimental investigations assessed the importance of IPEC dominant mode coupling to optimal correction of $n$=2 error fields. Discharges with and without deliberately applied "proxy" EFs from the DIII-D C-coil were optimized by scanning $n$=2 I-coil currents. Different I-coil optimal currents were found with and without the proxy EF, indicating that the I-coil could correct a portion of the C-coil EF, despite poorly matched poloidal spectra. The changes in the optimal $n$=2 correction currents were consistent with those required to null the IPEC dominant mode coupling, and also with the currents needed to minimize the volume-integrated NTV torque. However, despite optimal I-coil correction, the induced momentum degradation from the C-coil could not be recovered. Similarly, in experiments with a localized magnetic perturbation (the Test Blanket Module mockup), optimized $n$=2 error field correction yielded little or no reduction of the braking torque. Dedicated discharges applying fields with nulled and maximized dominant mode coupling confirm the presence of residual braking with fields that do not couple (and are thus orthogonal) to the IPEC dominant mode, directly demonstrating additional components of the field are important. Interestingly, nulling IPEC dominant mode coupling was found to eliminate density pumpout and thus confinement degradation, suggesting this phenomenon is dependent only to the degree of dominant mode coupling perhaps through the connection to the resonant surfaces. Future analysis of this dataset will assess the importance of $n$=4 sidebands to these results, and examine the structure of the magnetic plasma response excited by the different applied spectra.

### References

[1] J.-K. Park, A.H. Boozer, and A.H. Glasser, *Phys. Plasmas* **14**, 052110 (2007).

[2] J.-K. Park, M.J. Schaffer, J.E. Menard, and A.H. Boozer, *Phys. Rev. Lett*. **99**, 195003 (2007).

[3] A.H. Boozer, *Fusion Sci. and Technol.* **59**, 561 (2011).

[4] C. Paz-Soldan, M.J. Lanctot, N.C. Logan, D. Shiraki, R.J. Buttery, J.M. Hanson, R.J. La Haye, J.-K. Park, W.M. Solomon, and E.J. Strait, *Phys. Plasmas* **21**, 072503 (2014).

[5] N.C. Logan, J.-K. Park, K. Kim, Z. Wang, and J.W. Berkery, *Phys. Plasmas* **20**, 122507 (2013).

[6] M.J. Schaffer, J.E. Menard, M.P. Aldan, J.M. Bialek, T.E. Evans, and R.A. Moyer, *Nucl. Fusion* **48**, 024004 (2008).

[7] J.-K. Park, M.J. Schaffer, R.J. La Haye, J.T. Scoville, and J.E. Menard, *Nucl. Fusion* **51**, 023003 (2011).

[8] J.-K. Park, A.H. Boozer, J.E. Menard, and M.J. Schaffer, *Nucl. Fusion* **48**, 045006 (2008).

[9] H. Reimerdes, A.M. Garofalo, E.J. Strait, R.J. Buttery, M.S. Chu, Y. In, G.L. Jackson, R.J. La Haye, M.J. Lanctot, Y.Q. Liu, M. Okabayashi, J.-K. Park, M.J. Schaffer, and W.M. Solomon, *Nucl. Fusion* **49**, 115001 (2009).

[10] S.P. Gerhardt, J.E. Menard, J.-K. Park, R.E. Bell, D.A. Gates, B.P. LeBlanc, S.A. Sabbagh, and H. Yuh, *Plasma Phys. Controlled Fusion* **52**, 104003 (2010).

[11] M.J. Lanctot, et al., "Establish Requirements for Control of TBM-induced Effects for ITER, Report for Milestone 188," General Atomics Report GA-C27941 (2014).

[12] M.J. Schaffer, *Nucl. Fusion* **51**, 103028 (2011).

[13] C.E. Kessel, et al., *Nucl. Fusion* **49**, 085034 (2009).

[14] H. Reimerdes, et al., "Rotation Braking and Error Field Correction of the Test Blanket Module Induced Magnetic Field Error in ITER," *Proc. 24th IAEA Fusion Energy Conference* (San Diego, 2012), paper EX/P4-09, http://www-naweb.iaea.org/napc/physics/FEC/FEC2012/papers/339_EXP409.pdf

[15] Z.R. Wang, et al., *Phys. Plasmas* **21**, 042502 (2014).

## 4. Role of Plasma Response in Transport and NTV Torque

Non-axisymmetric magnetic fields change the transport process in a fundamental way. Since the magnetic field strength is no longer periodic by the symmetry breaking, the action for a particle becomes dependent on the toroidal location and the conservation of action $J = \oint M v_{\|} \, dl$ implies that the particle must drift across the magnetic surfaces. This process strongly depends on the species, and consequently induces non-ambipolar diffusion and modifies the radial electric field until an ambipolar electric field is established. This so-called non-ambipolar neoclassical transport is intrinsically different from the conventional neoclassical transport in tokamaks [1]. For example, the radial drift of particle orbits is naturally expected in non-axisymmetric configuration unless collisions occur, and therefore the transport can scale inversely with the collision as $D_{NA} \propto 1/\nu$, while $D_A \propto \nu$ in the axisymmetric configuration. Although the particle and heat transport may be still dominated by turbulent process, it is expected that the non-ambipolar transport can greatly enhance the toroidal momentum transport, as commonly called neoclassical toroidal viscosity (NTV) transport [2-4]. The modification of the radial electric field by NTV can strongly influence on various plasma instabilities, and thus NTV physics has been of great interest in 3D field physics. The predictive capability for NTV depends not only on the NTV model, but also on the plasma response model that provides the information of the magnetic field strength, on which NTV model is built upon. The experimental validation inevitably requires the simultaneous resolution of these two-fold issues, but it is possible to perform the numerical verification for each side of transport and equilibrium separately, among analytic theories and various computations.

Here the focus was made first on NTV modeling verification among PENT [5], MARS-Q [6], MARS-K [7], POCA [8] codes but using the same 3D equilibrium solutions, either by IPEC or MARS, as described in Sec. 4.1. The code benchmarking efforts show all the methods qualitatively agree to each other but can differ quantitatively by a few factors in a wide range of collisionality when the E×B is sufficiently low. In high E×B, an-order-of-magnitude under-estimation can be resulted if the bounce-harmonic resonances are not accounted. Section 4.2 describes the comparisons between NTV prediction based on IPEC-PENT or IPEC-POCA and experiments and the measured torque or torque profiles in DIII-D and NSTX. This coupling to the ideal 3D response code was successful to predict the measured torque (~3 Nm) in DIII-D with various NTV models, but NSTX case needed the first-principle NTV code such as POCA to have a quantitative agreement for the measured torque. Also it was shown that more relevant response modeling beyond

ideal MHD might be important to predict the details of the torque profiles. Section 4.3 describes those efforts with different response modeling, with vacuum assumption and with M3C-C1 non-ideal code. The results indicate that the plasma response is not strong for the NSTX $n$=3 and the vacuum method can be used if the Lagrangian correction is included, but again more precise 3D response modeling would be necessary to make a quantitative prediction in the torque profiles. In the last Sec. 4.4, one of the developed methods was utilized to optimize NTV torque and improve the new 3D coils in NSTX-U, by coupling with stellarator optimizers, yielding interesting implications to the 3D coil capability to control NTV.

### 4.1 NTV Model Verification

The NTV code benchmark has been carried out systematically among four different numerical codes; three different semi-analytic codes based on NTV and kinetic MHD stability theory, and also a particle simulation code based on first principles. Including the plasma response model, the numerical codes corresponding to each approach are respectively: (1) IPEC-PENT based on the combined NTV theory but without geometric simplifications, (2) MARS-Q based on the smoothly connected NTV formula based on Shaing's analytic formulation in various collisionality regimes [9], (3) MARS-K originally computes the drift kinetic energy and was upgraded to compute the NTV torque based on the equivalence between drift kinetic energy and NTV torque [10], and (4) POCA, which is δf drift-kinetic particle code directly computing NTV using perturbed anisotropic pressures.

First the equivalence of kinetic potential energy and NTV torque was numerically affirmed by comparison between MARS-K and IPEC-PENT as shown in Fig. 4-1 [7]. Excellent quantitative agreements were obtained in the NTV comparison without and ($\ell$=0) and with the bounce-harmonic resonances (total $\ell$). NTV scan in the wide range of collisionality with finite ExB precession has also been performed using four codes. The comparison between the connected NTV formula and the combined NTV theory in different collisionality regimes were successfully made for the first time using MARS-Q and MARS-K, respectively, and also IPEC-PENT. However, there are quantitative differences by a few factors, as Fig. 4-2 shows the predicted super banana-plateau (SBP) behaviour [11] in the low collisionality by three codes but with some differences depending on the collisionality. The additional comparison with POCA, which is based on the first principles and so believed to be more precise, shows that MARS-K and IPEC-PENT agree better to POCA possibly due to the geometric generalization. Note that these benchmarking examples are based on a circular, high-aspect ratio tokamak geometry, but it is shown that still a substantial difference can be resulted when the geometry is simplified in the velocity space integrations or when the arc-length change is ignored. The geometric simplification in MARS-Q has been removed in NTVTOK, which will

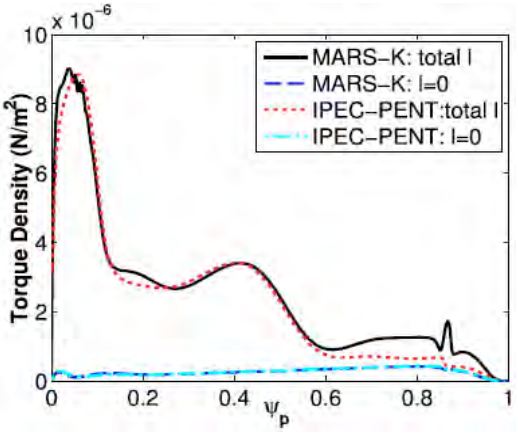


Fig. 4-1. NTV torque density profiles by MARS-K and IPEC-PENT compared for total $\ell$ and $\ell$=0.

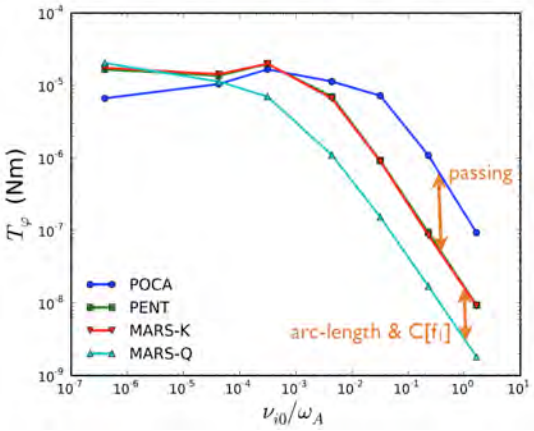


Fig. 4-2. SBP comparison among four NTV codes.

also be compared with other codes in the future. The difference in high collisionality between POCA and other codes is presently understood by incomplete orbit trajectories of most of particles in the regime, which can make the path of integral of the semi-analytic codes less precise. Also note that the benchmark of bounce-harmonic resonances between IPEC-PENT, MARS-K, and POCA indicates that the bounce-harmonic resonance can greatly enhance the NTV torque when E×B precession frequency reaches the resonance condition. The enhancement can easily reach to an order of magnitude especially in the low collisionality, indicating that it is important to include bounce-harmonic resonances in the practical application of NTV codes for experimental analysis.

### 4.2 NTV Validation with Ideal 3D Codes in DIII-D and NSTX

In parallel with the code benchmarking for the simplified geometry, efforts for experimental validation of the developed NTV codes have been made, and successful for rotation damping analysis in the DIII-D and NSTX magnetic braking discharges [12]. Experimental NTV analysis is a more complicated issue as (1) it is always difficult to isolate NTV torque in experiments, and (2) calculations of perturbed equilibrium and the 3D variation in the field strength may be not fully self-consistent. For the first step, the ideal plasma response model was employed so that the perturbed non-axisymmetric fields computed by IPEC were input to each code with prescribed kinetic profiles and parameters obtained from measurements.

NTV prediction results in the DIII-D QH-mode discharge (145117) are shown in Fig. 4-3, where POCA, IPEC-PENT and IPEC-LAR, which is a version of IPEC-PENT with the geometric simplification [1,5]. Non-resonant $n$=3 magnetic perturbations were applied using I-coil and C-coil to the NBI-heated plasma in this discharge, so the net-NBI torque at the ITER-relevant level was achieved with the magnetic braking by the NTV

torque. Collisionality-regime analysis indicates that the plasma is largely in the $\nu\_\nu^{1/2}$ regime [13] but bounce-harmonic resonances can take effects in the edge region. Note there is no experimental measurement for NTV profile for the discharge but the total NTV torque was measured using an angular momentum balance equation. Comparison of NTV profile between three codes shows a good quantitative agreement as shown in Fig. 4-3, and the total torque by each code also agrees well with the experimental estimation of ~3 Nm (cf. POCA: 2.9 Nm, IPEC-PENT: 2.8 Nm, IPEC-LAR: 2.6 Nm).

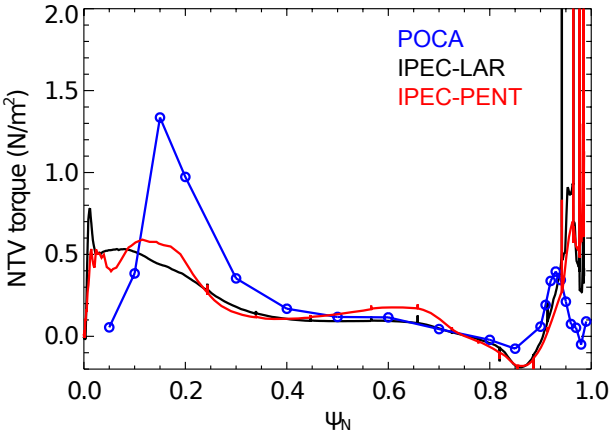


Fig. 4-3. Comparison of NTV torque profile computed by IPEC-RLAR, IPEC-PENT, and POCA for DIII-D discharge 145117.

NTV analysis in the NSTX experiment has many more difficulties compared to the DIII-D. Theoretical approximations such as the large aspect-ratio expansion and the zero-orbit-width become crucial and invalid for NSTX due to the low aspect-ratio and weak toroidal magnetic field. In addition, the bounce-harmonic resonance effects become stronger than theory prediction when the rotation is fast in NSTX since particle transport by bounce-harmonic resonances can be largely underestimated without finite orbit width [15].

The comparison between experiment and POCA calculation shown in Fig. 4-4 illustrates such difficulty. In this NSTX discharge 124439, NTV profile was measured from changes dL/dt in the angular momentum density profile, caused by the *n*=3 non-resonant magnetic braking. The plasma is in the complicated collisionality regime and bounce-harmonic resonances take a strong effect in the whole volume. Figure 4-4 indicates that the POCA code roughly agrees with the experimental measurement, although the location of the NTV peak is shifted inward and the finite amount of NTV at the central region is not well captured. Such discrepancies may indicate more self-consistent, non-ideal 3D equilibrium

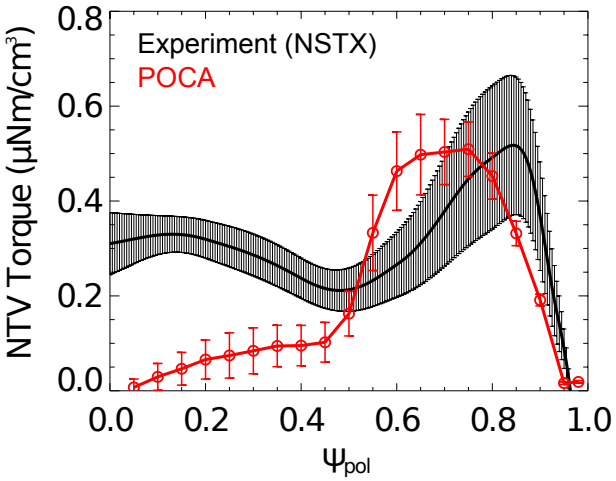


Fig. 4-4. Comparison of NTV torque profile between measurement and POCA simulation in NSTX discharge 124439.

including neoclassical friction forces, or better isolation and momentum transport analysis in measuring experimental torques. Nonetheless, POCA calculation largely improved the NTV predictability because the semi-analytic calculation by IPEC-LAR or IPEC-PENT predict much weaker NTV by up to an order of magnitude (not shown here). POCA prediction for the total torque is ~2.7 Nm which is indeed close to experimental value ~3.5 Nm, but prediction for torque density profile will require more details of NTV physics and perturbed fields.

Another approach to calculate NTV is to utilize even the full-f global particle simulation with XGC0, which is capable of rich physics simulation with multi-species particle dynamic of electrons and neutrals. The initial test has been performed in the same DIII-D 145117 discharge and shown that the qualitatively similar torque profiles can be predicted if the ions, electrons, and proper boundary conditions for neutrals are all included. Further studies are planned to perform the full time-evolution XGC0 simulation of the momentum transport and NTV, and with the injection torque models. In parallel with the effort for advanced transport modelling, the plasma response modelling should also be improved to include kinetic and/or non-ideal effects self-consistently. MARS-K applications to DIII-D highlighted the importance of the self-consistent kinetic response calculations in high-beta plasmas for $n$=1, and also M3D-C1 applications showed non-linear and non-ideal effects can play important roles especially in the high n resonant magnetic perturbations for ELM suppression. The various response modeling applications and validations are described in details in Sec. 2, and also the application of a non-ideal response code to NTV is described in the next section.

### 4.3 NTV Validation with Non-ideal 3D Code in NSTX

Experiments conducted on NSTX utilizing rapid changes (signifi-cantly faster than the momentum diffusion time) of an applied 3D field, $\delta B$, best isolate the torque profile exerted on the plasma by NTV. The measured angular momentum damping and the theoretically computed torque density profile, $T_{NTV}$, created by a range of experimentally applied 3D field spectra and plasma parameters were anal-yzed, including configurations with dominant $n$=2 and $n$=3 field components. Figure 4-5 com- pares the theoretically computed $T_{NTV}$, profile vs minor radial coordinate to the measured change in the plasma angular momentum density, $dL/dt$, for an $n$ = 3 field applied field configuration as $\delta B$ is rapidly changed. The analysis computes $\delta B$ fully in 3D, and uses the complete Shaing formulation of $T_{NTV}$ valid for all collisionality regimes and the super banana plateau regime for both ions and electrons as implemented in the NTVTOK code [6]. In this calculation, the vacuum approximation is used by assuming the weak amplification in the $n$=3 but including the Lagrangian evaluation of the field as, $\delta B = \vec{b} \bullet \left(\vec{B} / B\right) + \left(\vec{\xi} \bullet \nabla B\right)$, in order to approximate the effect of flux surface displacement, $\boldsymbol{\xi}$, in the plasma [16]. The

large radial variations of the theoretical $T_{NTV}$ shown in Figure 4-5 are due in part from this, and appear in other published models of $\boldsymbol{\xi}$. In contrast, such large radial variations of $T_{NTV}$ are not observed experimentally. Rather, $T_{NTV}$ is experimentally found to be radially extended, without strong localization of the torque as is observed in resonant braking by magnetic islands. Solution of the momentum diffusion equation shows that the charge exchange recombination spectroscopy diagnostic could discern details of the $\omega_\phi$ evolution caused by these strong radial variations if they existed. Experiments at low $A$ yield unique information as the maximum computed displacement $|\boldsymbol{\xi}|$ = 0.3 cm is smaller than either the ion banana width or gyroradius suggesting that finite-orbit effects will average the $T_{NTV}$ profile over such spatial scales. Figure 4-5 shows that averaging the ion $T_{NTV}$ profile over the banana width more closely matches the measured *dL/dt* profile.

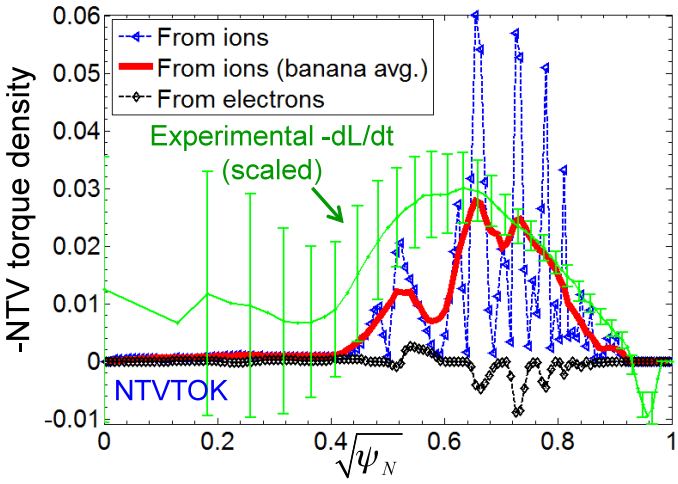


Fig. 4-5. $T_{NTV}$ profile components for an $n$=3 field configuration in NSTX, computed from (i) ions using the vacuum field assumption, (ii) ions using banana width-averaging, (iii) electrons. The measured (-dL /dt) profile is shown in green.

A related critical and advanced area of research regarding $T_{NTV}$ profile computation is the evaluation of the plasma response. A major issue is that the full plasma displacement $\boldsymbol{\xi}$ and its plasma-induced amplification are not directly measured in detail in any experiment and the development of first-principles models is still an active research area. An accurate, first-principles physics model of plasma response has been elusive. The NSTX NTV experimental data and analysis (e.g. as shown in Fig. 4-5) provides a strong constraint to validate plasma response models of the applied 3D vacuum field across the plasma minor radius. Since $T_{NTV}$ scales as $\delta B^2$, error in any particular theory of plasma response is strongly amplified when compared to the experimentally measured $T_{NTV}$ profile. Models tested to date against experiment using the comparison of the measured $T_{NTV}$ profile as a figure of merit include the vacuum field assumption for $\boldsymbol{\xi}$, and various physics models in the M3D-C$^1$ resistive MHD code, including the single, and two-fluid models. Analyses to date show the M3D-C$^1$ single-fluid model produces a flux surface-averaged $\delta B$ magnitude consistent with the experimentally measured $T_{NTV}$ profile in the region of the plasma where $T_{NTV}$ is strongest. In Fig. 4-9, the surface averaged $\delta B$ field profile from M3D-C$^1$ is compared to the equivalent profile used in the NTVTOK code calculations of the NTV torque density profile as shown in Fig. 4-6. As the reference [6]

shows, good agreement is found when comparing the single fluid M3D-C[1] field profile and that used to model the instantaneous NTV torque profile using the NTVTOK code in the radial region between $0.5 < \psi_N^{1/2} < 0.9$ using the banana width-averaged vacuum field assumption model for the NSTX plasma analyzed in Fig. 4-6. Conclusions regarding the strength of the field perturbation can only be drawn inside this region (at lower $\psi_N$), since outside of this region the instantaneous NTV torque density measurements made in the experi-ment are too weak to determine $\delta B$. This is expected, since the $T_{NTV}$ profile scales with plasma rotation, $V_\phi$, and ion temperature, $T_i$, approximately as $V_\phi T_i^{2.5}$ in the operational regime of this plasma, and outside of $\psi_N = 0.9$, both $V_\phi$ and $T_i$ are low). In this case, the M3D-C[1] simulation has a core mode, which may be contributing to a larger averaged $\delta \boldsymbol{B}$ in the core region than the NTVTOK calculation (dashed red line in Fig. 4-6). In contrast, the plasma response as computed by the M3D-C[1] two-fluid model presently overestimates the averaged $\delta B$ field profile.

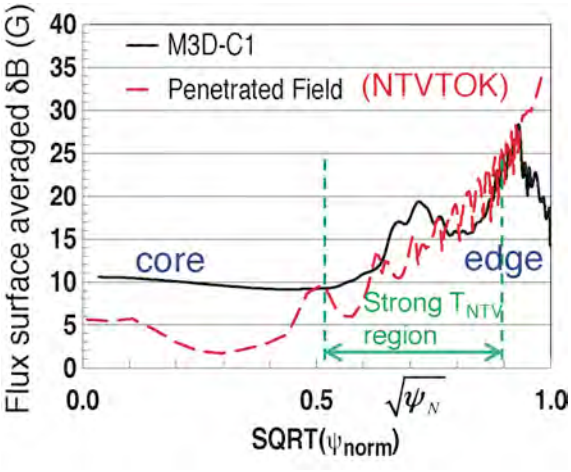


Fig. 4-6. Flux surface averaged δB from a single fluid M3D-C[1] simulation (solid black) and from the vacuum approximation in NTVTOK (dashed red) used to calculate $T_{NTV}$ for the $n$=3 applied field configuration as shown in Fig. 4-5.

### 4.4 NTV Optimization with NCC in NSTX-U

The verification and validation efforts described in Sec. 4.1.3 indicate the presently developed tools need to be improved to make quantitative NTV prediction precisely, but also can be used to predict the qualitative trends of NTV torque. So an advanced tool for optimization, using IPEC and PENT, has been developed and applied to the plasmas of the NSTX-U and DIII-D tokamaks. The IPECOPT code has been developed by leveraging the existing efforts in non-linear stellarator optimization. The code is a port of the STELLOPT code, wherein the VMEC 3D equilibrium code is replaced with the IPEC perturbed equilibrium code and it's associated interfaces to other codes. This gives the code access to well established parallelized optimization routines such as Levenberg-Marquardt, differential evolution, particle swarm, and hyperspace mapping. The parallelization significantly reduces the time necessary to carry out these optimizations in much the same way it way it was used for stellarator design. The initial development of IPECOPT has focused on total and vacuum normal magnetic field optimization with NTV torque serving as the target (calculated by the PENT code).

The NTV torque response of two NSTX-U equilibrium scenarios were investigated using the code in a fixed boundary mode. Optimization of core NTV torque with applied $n$=1 perturbing fields indicated kink resonant fields could drive core torque (inside ρ=0.5). This was done without driving significant edge torques. As a side effect of targeting the torque density, resonant fields were also minimized during these optimizations. Subsequent optimization of edge NTV torque with applied $n$=3 fields resulted in a normal field spectrum which was field line crossing and was capable of driving a broad edge toque while minimizing resonant effects near the edge of the plasma, as shown in Fig. 4-7. This pitch-crossing field pattern, as illustrated in Fig. 4-8, is one of many orthogonal modes to pitch-resonant field or Kink-mode in space, and requires the coils with sufficient spatial coverage to drive it without the amplification of the resonant field. It is shown that the NCC coil with partial 2x6 array in NSTX-U can substantially produce such a pattern if combined the existing midplane coils, indicating the advantage of the present NCC design in the fundamental level.

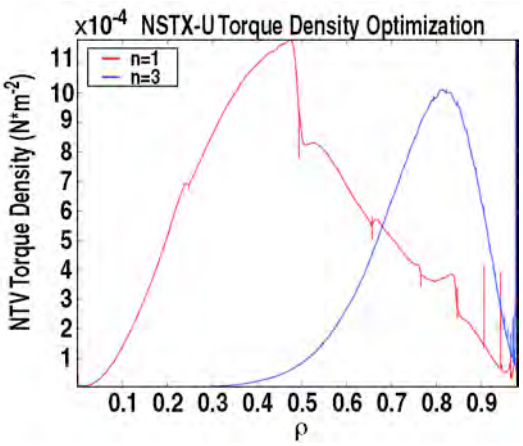


Fig, 4-7. Optimizations of core and edge torque showing ability to control torque profile with 3D fields.

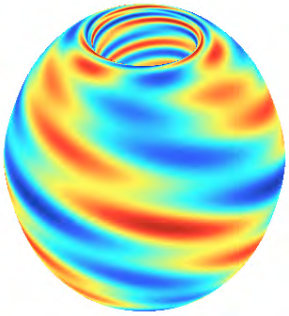

Fig. 4-8. Field pattern optimizing $n$=3 NTV.

A validation exercise of the code was carried out using an error field correction study in the DIII-D device. The mapping capability of the IPECOPT code was used to generate 625 equilibria, which scanned the applied C-coil amplitude and phase while error field information was provided by the SURFMN code. As shown in Fig. 4-9, mapping appears to predict an amplitude and phase consistent with experimental measures. An optimization was performed using IPECOPT (using the Levenberg-Marquardt algorithm), which corroborated this finding. This work highlights the added capability of the code to perform free boundary optimization using realistic coils and modeled error fields. Future plans include the

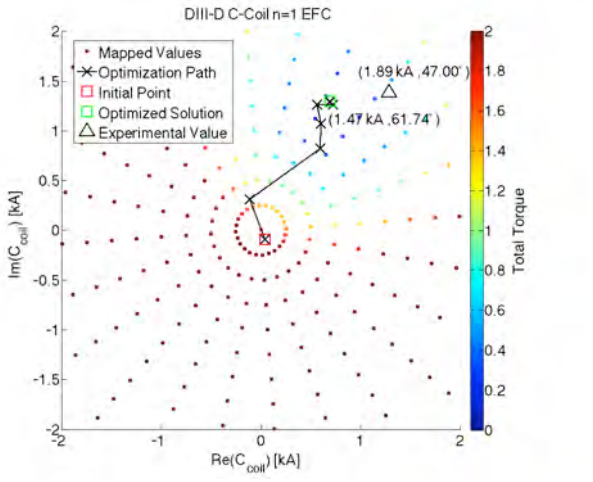


Fig. 4-9. Optimization of DIII-D error field using IPECOPT to minimize NTV torque.

implementation of new optimizer targets (island overlap, particle orbits), examination of I-coil based NTV optimization in DIII-D, and calculation of the effect of adding additional rows of coils to the NSTX-U non-axisymmetric control coil design.

## References

[1] J.-K. Park, *et al*., *Phys. Rev. Lett*. **102**, 065002 (2009).
[2] K.C. Shaing, *Phys. Fluids* **26**, 3315 (1983).
[3] K.C. Shaing, *Phys. Plasmas* **10**, 1443 (2003).
[4] W. Zhu, *et al.*, *Phys. Rev. Lett.* **96**, 225002 (2006).
[5] N.C. Logan, *et al.*, *Phys. Plasmas* **20**, 122507 (2013).
[6] Y. Sun, *et al.*, *Nucl. Fusion* **51**, 053015 (2011).
[7] Z. Wang, *et al.*, *Phys. Plasmas* **21**, 042502 (2014) .
[8] K. Kim, *et al*., *Phys. Plasmas* **19**, 082503 (2012).
[9] K.C. Shaing, *et al.*, *Nucl. Fusion* **50**, 025002 (2010).
[10] J.-K. Park, *Phys. Plasmas* **18**, 110702 (2011) .
[11] K.C. Shaing, *et al.*, *Plasma Phys. Control. Fusi*on **51**, 035009 (2009).
[12] K.C. Shaing, *et al.*, *Phys. Plasmas* **15**, 082506 (2008).
[13] K. Kim, *et al.*, *Nucl. Fusion* **54**, 073014 (2014).
[14] K. Kim, *et al*., *Phys. Rev. Lett*. **110**, 185004 (2013).
[15] A.H. Boozer, *Phys. Plasmas* **13**, 044501 (2006).

## 5. Role of Plasma Response in Divertor Heat Flux

A well-known result of applying 3D magnetic perturbation to diverted tokamak plasmas is the formation of striations in the particle and heat fluxes to the divertor, giving spiraling flux patterns on the PFC surface. This is attributed to the splitting of the separatrix into stable and unstable manifolds [1], which have a helical lobe structure that is pronounced near the X-point and can intersect the plasma facing components (PFCs) resulting in the observed striations. Understanding and predicting plasma transport along these magnetic structures is necessary for future devices such as ITER to avoid significant fluxes in unexpected locations. Further, the plasma response, especially the screening of resonant components of the applied fields, is known to affect the size and position of the lobes [2]. As a result, it is necessary to include plasma response in the magnetic field model used to predict divertor strike patterns. As shown below, including plasma response is necessary in order to correctly reproduce the measured divertor patterns, offering a unique path for validating response models. Finally, aside from the magnetics, divertor measurements in the presence of 3D fields allow the validation of 3D plasma transport models, which is a critical component of the overall plasma response aside from just the magnetic response. In this section, validation efforts are described in two major areas: (a) the presence and spatial patterns of plasma flux during 3D field application, and (b) the impact of 3D fields on divertor transport response, in particular affecting access to detachment. These involved experiments and modeling of DIII-D and NSTX plasmas with 3D fields applied.

### 5.1. The Role of Plasma Response in Strike Point Splitting

Externally applied 3D fields can break the toroidal symmetry of divertor heat and particle deposition, generating striated heat and particle footprints at the divertor surface. This is a direct consequence of the “strike point (SP) splitting” caused by the 3D fields to the plasma edge. As many tokamak PFCs are designed and built assuming toroidal symmetry to protect areas where high heat and particle fluxes are expected from the 2D equilibrium, these non-axisymmetric divertor profiles could result in additional engineering constraints.

The relation between the plasma response and strike point splitting, therefore divertor footprint patterns, has been investigated in DIII-D experiments as a function of several plasma parameters, particularly for plasma triangularity and collisionality. The amplitude and phase of response fields are obtained by subtracting vacuum reference fields from the total fields measured by recently upgraded magnetic pickup probes in both inner and outer walls [3]. A 2D plot of response fields is generated by fitting signals from multiple

probes. This is very useful as the 2D image can be compared to the modeling from plasma response calculation codes such as IPEC (linear ideal), and give confidence in the accuracy of modeled response fields. Figure 5-1 shows an example of 2D poloidal field ($B_p$) from the plasma response to the $n$=3 applied fields, for both magnetics and IPEC simulation. It is seen that both the amplitude and phase of measured response fields are in good agreement with the modeling. This result is interesting in that the modeled discharge achieved ELM suppression at high density $\left(\bar{n}_e > 7\times10^{19}\ \mathrm{m}^{-3}\right)$ and collisionality ($\nu_{*e} > 2$), a condition normally thought to lead to being resistive and therefore an ideal model wouldn't be applicable to. It is being investigated how plasma response in such a condition can become ideal.

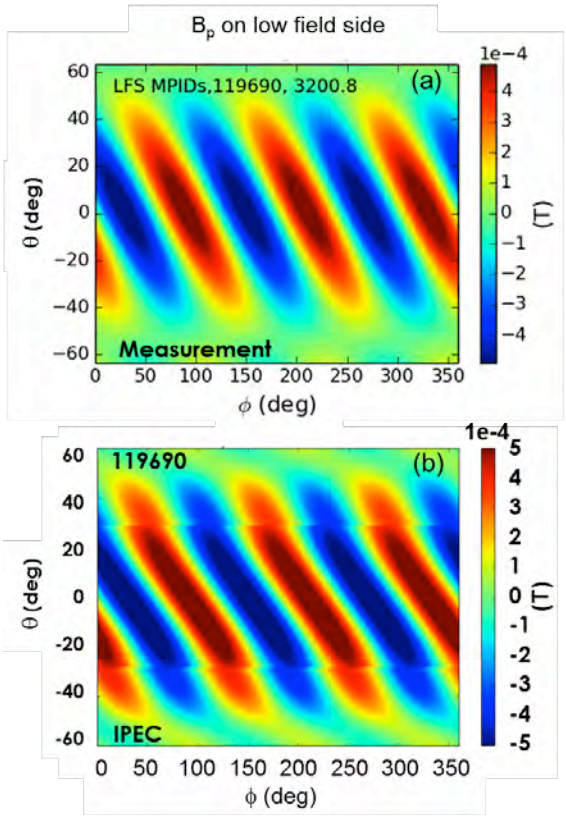


Fig. 5-1. Plasma response fields ($B_p$) at LFS for an odd parity $n$=3 perturbation in DIII-D, from the (a) measurement, and (b) ideal plasma response calculation (IPEC). θ is poloidal angle with 0 at the midplane and ϕ is toroidal angle.

Calculations of the perturbation to the plasma from the applied 3D fields can be performed. Figures 5-2(a) and 5-2(b) show the poloidal magnetic spectra of the applied perturbation ($\beta_N$) as a function of poloidal mode number ($m$) and normalized radius $\left(\Psi_N^{1/2}\right)$ for an $n$=3 coil configuration with even and odd parity (up-down symmetric and anti-symmetric) respectively. $\beta_N$ is surface weighted perpendicular component of the perturbed field. Superimposed on the spectra are the location of the $q$=$m$/3 rational surfaces, which is a representation of field line pitch and is therefore directly related to $q_{95}$. It is seen that the applied perturbation is more pitch-resonant in the even configuration; the rational surface locations in the odd parity are well aligned with the valleys in the applied perturbation. Figures 5-2(c) and 5-2(d) are poloidal spectra of total fields including plasma response calculated by IPEC. The first thing to note is that the pitch resonant components in the even parity are screened in the presence of a plasma, Fig. 5-2(c), which is due to the induction of localized currents that exactly cancel the resonant component of the applied fields. In addition, high $|m|$ components ($-20 < m < -10$) at the very edge of the plasma $\left(\Psi_N^{1/2} > 0.9\right)$ are excited by the plasma response, which is caused by the coupling of non-resonant components of the applied fields to the

global kink mode [4]. This kink mode excitation is significantly more prominent in the odd parity, Fig. 5-2(d), while the pitch-resonant components remain screened.

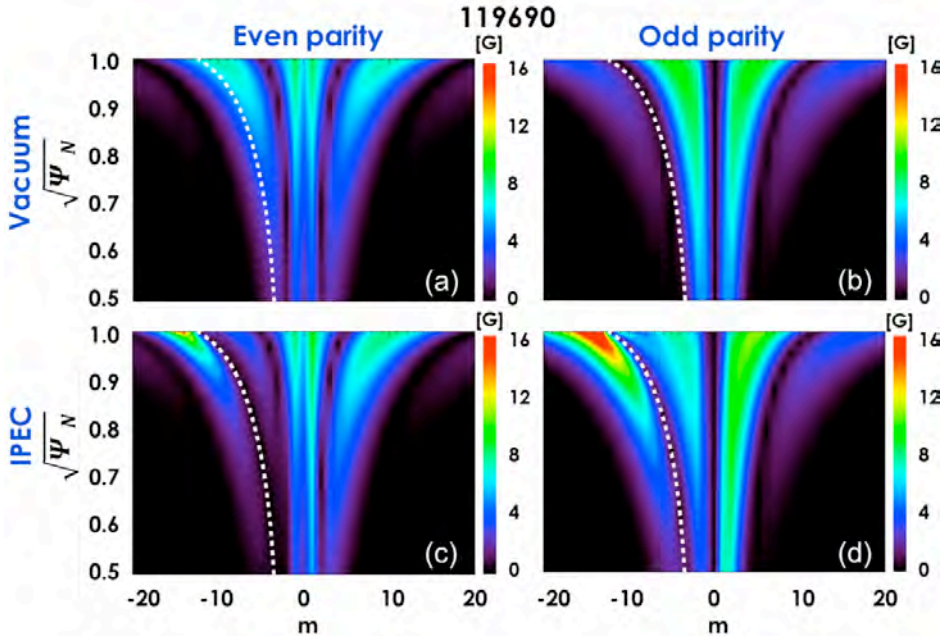


Fig. 5-2. Amplitude of the $n$=3 poloidal mode harmonics of normal component of applied perturbation, calculated with IPEC as a function of $\Psi_N^{1/2}$ for the same shot as in Fig. 5-1. (a) and (b) are for the applied fields only and (c) and (d) are total fields including plasma response. The dashed white line marks the locus of points satisfying $q=m/3$.

The next step is to look into the effect of this resonant and non-resonant plasma response on the strike point splitting. A 3D SOL/divertor transport calculation using a code such as EMC3-Eirene will be necessary to compare to the experiment, but at this stage we just seek for the field line tracing calculation to look at the divertor footprints. Figure 5-3(a) and 3(b) show the results from a field line tracing using the POCA code [5], for vacuum and ideal plasma response (IPEC) case, respectively. This shot had $n$=3 odd parity perturbation applied and there was clear strike point splitting observed for both heat and particle flux profiles. The vacuum field line tracing exhibits almost no splitting, Fig. 5-3(a). However, when plasma response is included in the field line tracing, the splitting is amplified and becomes substantially stronger, which is consistent with the strong kink response observed in the poloidal spectra plot, Fig. 5-2(b) vs 5-2(d). Indeed this result reflects the experimental observation of clear splitting for this shot, consistent with the amplification of splitting. Note that the footprint pattern from field line tracing does not include any transport effect, but is a pure representation of magnetic lobe structure induced by applied 3D fields. Thus this result indicates that magnetic separatrix splitting is strongly affected by plasma response, without which one could be led to an incorrect result. Another important conclusion from Figs 5-2 and 5-3 is that the separatrix

splitting is not affected only by resonant components, but non-resonant components also play an important role.

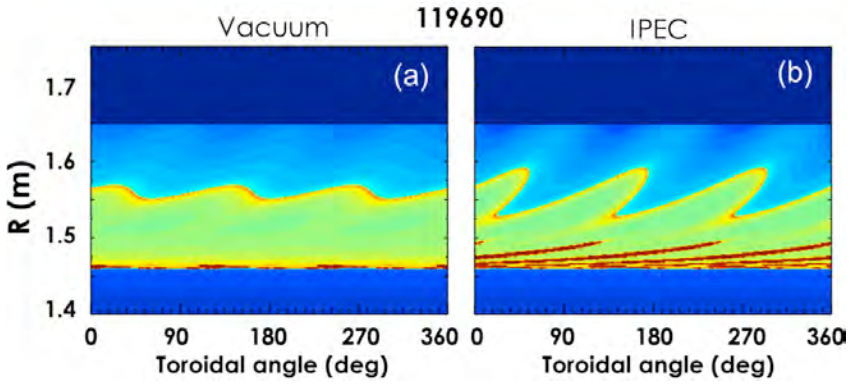


Fig. 5-3. Divertor footprints from a field line tracing in POCA [5] for (a) vacuum and (b) ideal plasma response (IPEC) case for an *n*=3 odd parity perturbation. The modeled discharge is the same as in Figs 5-1 and 5-2.

Now turning to the effect of plasma shape on the plasma response to determine separatrix splitting, Figs 5-4(a) and 5-4(b) compare poloidal spectra with IPEC plasma response included for discharges with different triangularities. It is immediately noticeable that kink response is much stronger for the high δ case. This is understandable as stronger shaping leads to higher edge parallel current ($j_{edge}$) which in turn can raise kink response according to recent work at DIII-D [6]. This result is consistent with the experimental observation that only a very weak splitting was observed for the low δ shape (155623) while a strong splitting was clear for the high δ shape (119690), with a *n*=3 odd parity perturbation applied for both shots. Again, the important role of non-resonant kink response in the determination of splitting is confirmed from this result. The screening of splitting for the even parity and amplification for the odd parity is also the same for both high and low δ cases.

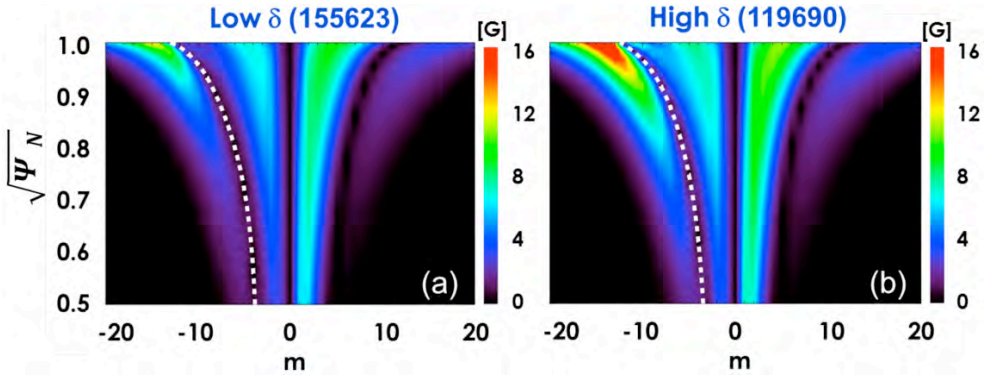


Fig. 5-4. Poloidal spectra of perpendicular component of applied perturbation for (a) high and (b) low triangularity case, calculated from IPEC, both for *n*=3 odd parity. The dashed white line marks the locus of points satisfying *q*=*m*/3.

Another interesting example is given in Fig. 5-5. Parity of the applied perturbation was flipped during the discharge, from odd to even, and the heat flux footprints show that splitting disappears during the even parity period. The amplitude of plasma response also dropped by a factor of ~5 compared to the odd parity period, see Fig. 5-5(a). This result is consistent with the stronger plasma response for the odd parity, confirmed from the IPEC modeling, due to the higher kink response presented in Fig. 5-2.

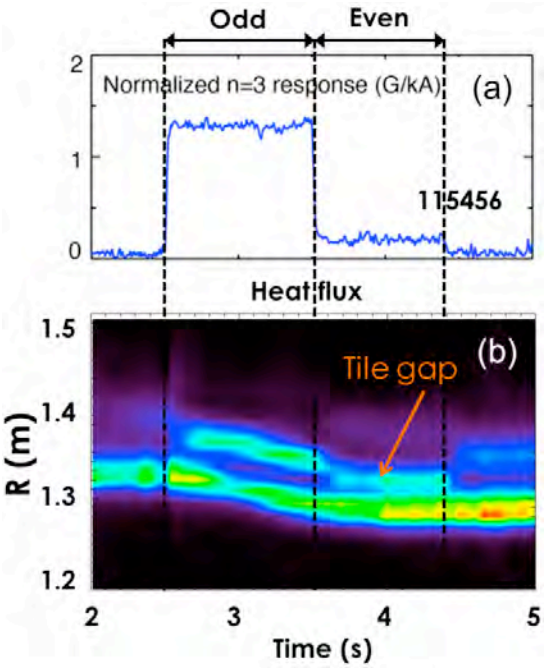


Fig. 5-5. Amplitude of measured plasma response (a) and heat flux profile (b) for 115456. Parity of 3D fields was flipped at t = 3.5 s from even to odd.

## 5.2 Effect of 3D Fields on Divertor Detachment

The strike point splitting caused by 3D fields can also affect the divertor regime. As shown in Fig. 5-6, NSTX has demonstrated that the application of 3D fields can cause a detached divertor plasma to re-attach [7]. Before the application of 3D fields, a gas puff is used to cause the divertor plasma to transition from attached (orange) to detached (blue), characterized here by a reduction in the primary peak. Fifty milliseonds after the gas puff, *n*=3 3D fields are applied, causing the plasma to reattach with several striated heat flux peaks.

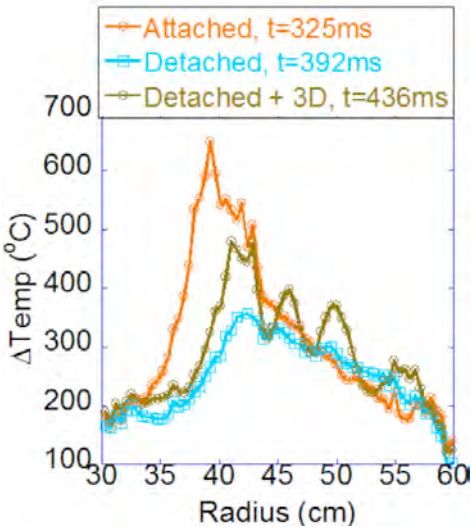


Fig. 5-6. Divertor temperature near the outer strike point ($R_{OSP}$ = 35.1 cm) under attached (orange) and detached (blue) conditions before the application of 3D fields in NSTX discharge 140508. The green curve shows the increased and peaked heat flux after 3D fields are applied.

These results can be used to validate various plasma response models against the experiment. One prevalent model is the so-called “vacuum approximation”, in which 3D magnetic fields calculated from the external coils in vacuum are superimposed over 2D equilibrium fields. In this model the 3D fields are strongly perturbative, resulting in significant stochasticity far inside the original separatrix. Figure 5-7 shows a Poincare plot generated using the vacuum approximation. Closed flux surfaces only exist far into the core, surrounded by remnant island chains. Magnetic

"lobes" produced by the perturbed separatrix connect the hot pedestal plasma to divertor plates, resulting in striated divertor fluxes. In this model these channels of hot, dense plasma could cause the divertor plasma to locally re-attach as seen in the experiment.

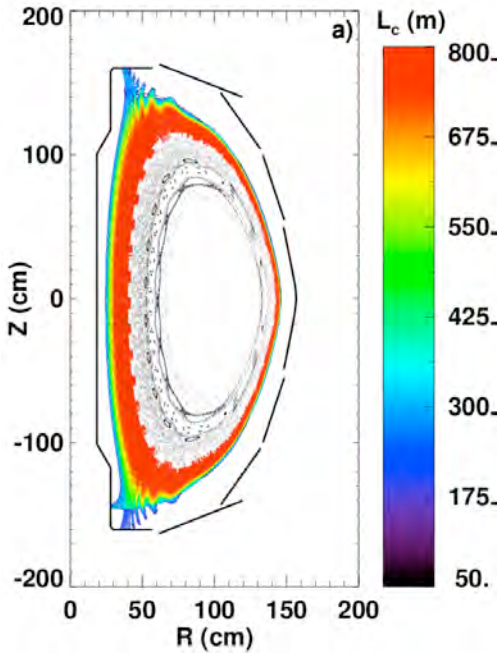


Fig. 5-7. Poincare plot using the vacuum approximation showing strongly stochastic fields.

The 3D transport code package EMC3-EIRENE [8] can be used to validate this and other field penetration models. The code consists of the steady-state fluid plasma solver EMC3 coupled to the kinetic neutral particle transport and plasma-material interaction code EIRENE. The fluid transport is classical (Braginskii) in the parallel direction, and diffusive with user-supplied heat and particle diffusion coefficients in the cross-field direction. The separation between parallel and cross-field transport is achieved in the grid definition, as the grid is required to be locally aligned with the magnetic field lines in the toroidal direction. The advantage to this method is that the fluid continuity, parallel momentum, and ion and electron energy equations are solved using a Monte-Carlo method in 3D for any magnetic field.

EMC3-EIRENE grids have been developed for NSTX for axisymmetric and 3D cases using the vacuum approximation. To investigate the effect of 3D fields on detachment, the core density was scanned in the code. Figure 5-8 shows the total particle flux (a), the power deposited (b), and the average electron temperature (c) on the divertor as a function of the separatrix density for the axisymmetric (red) and 3D (black) cases. As the separatrix density is increased, the particle flux initially increases as the deposited power and electron temperature decrease. The axisymmetric case begins to detach at a separatrix density of ~$0.5 \times 10^{20}$ $m^{-3}$, characterized by a decrease in the particle flux and an electron temperature of ~1 eV. (Note that the separatrix density decreases even as the density at the core boundary increases; the arrows in Fig. 5-8 indicate increasing core density). Over this density range the 3D case, on the other hand, does show trends characteristic of detachment.

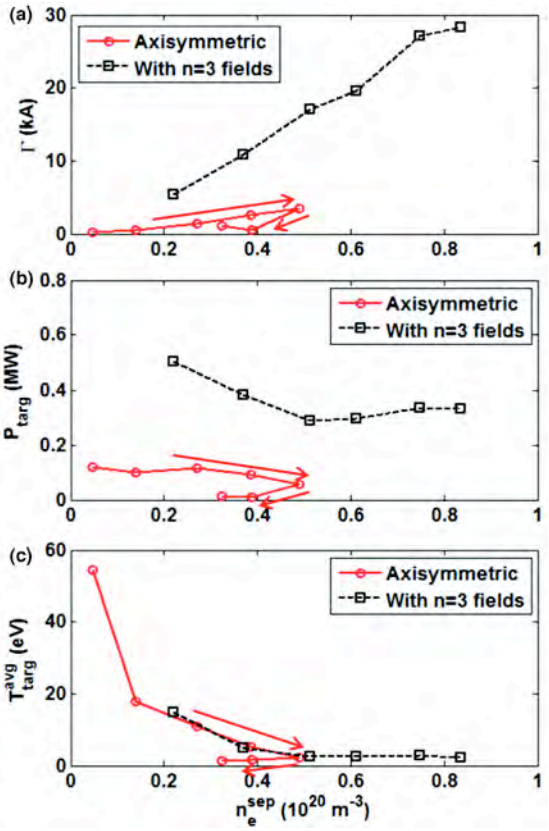


Fig. 5-8. Particle flux (a), deposited power (b), and average electron temperature (c) as a function of the separatrix density for axisymmetric (red) and 3D (black) cases.

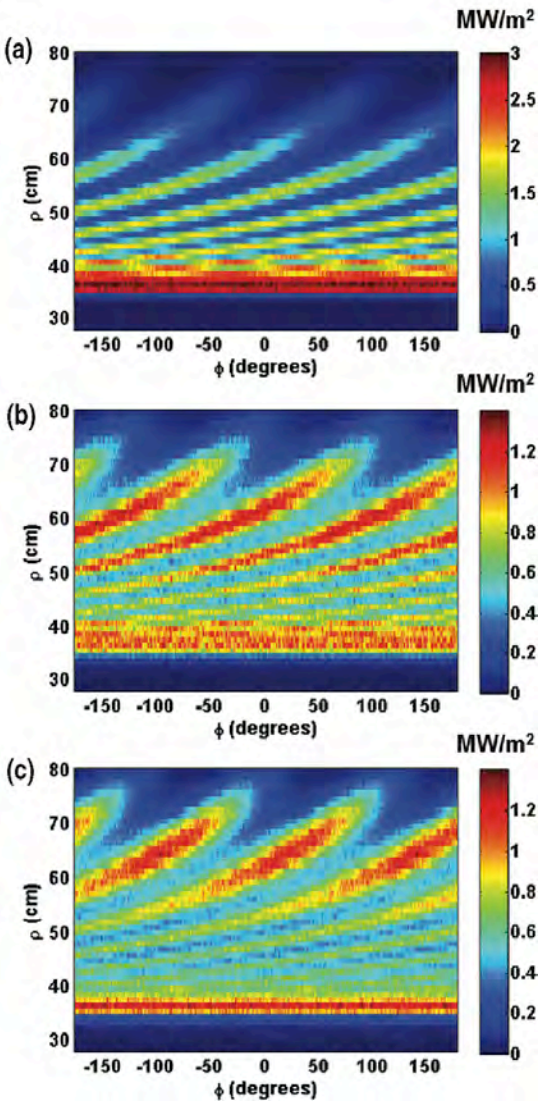


Fig. 5-9. 2D heat flux profiles at the outer horizontal target for three core densities: (a) $2x10^{20}$ $m^{-3}$, (b) $4x10^{20}$ $m^{-3}$ and (c) $5x10^{20}$ $m^{-3}$.

This difference between the axisymmetric and 3D simulations is thought to be due to an increased heat flux and electron temperature at larger radii caused by the short connection length flux tubes connected to the hot core plasma. Figure 5-9 shows 2D profiles of the heat flux to the outer horizontal target for three different core electron densities. As the core density is increased from (a) $2x10^{20}$ $m^{-3}$ to (c) $5x10^{20}$ $m^{-3}$ the plasma shows signs of local detachment at intermediate radii (40 cm < R < 50 cm), however this is counteracted by an increasing the power deposited in the lobes at large radii (R > 50 cm). As the density is further increased the continuous nature of the striations is obscured, and the heat flux appears to form “blobs” at large radii.

These trends, and the difference between the axisymmetric and 3D cases can be clearly seen in radial profiles of the heat flux, averaged over -170 < ϕ < -160 degrees. Figure 5-10 shows heat flux profiles without (a) and with (b) 3D fields applied for three

upstream densities. In the axisymmetric case the peak heat flux is reduced with increasing upstream density, reaching a low level characteristic of detached conditions. At an intermediate density, the heat flux is increased at larger radii, consistent with a transition to a conduction limited regime in the flux tubes near the strike point allowing perpendicular diffusion to have a larger effect, transporting energy and particles to the outer flux tubes. When 3D fields are applied the heat flux is only reduced near the strike point, while in the outer peaks the heat flux is not reduced, or is even increased. The outer peaks are connected to hotter regions of the plasma inside of the unperturbed separatrix, and do not transition to the conduction limited or detached regimes over this density range. The flux tubes connected to the primary peak do reach the conduction limited regime, which again allows for perpendicular diffusion to transport particles to larger radii and causes a smoothing of the secondary peaks. These results are qualitatively consistent with the experimental data, however a quantitative comparison has yet to be performed.

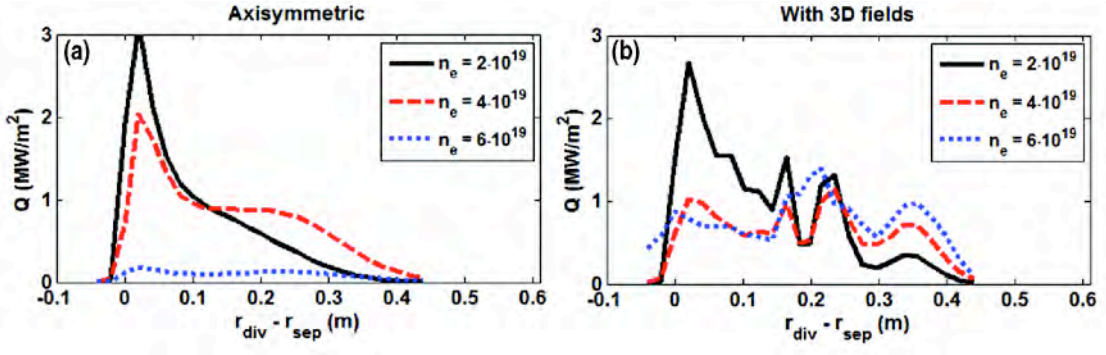


Fig. 5-10. Heat flux profiles calculated by EMC3-EIRENE for several upstream densities without (a) and with (b) 3D field applied.

A similar experiment to look into the effect of 3D fields on divertor detachment was performed at DIII-D in the fall of 2013. A low triangularity plasma shape was chosen in order to locate the outer strike point on the shelf to allow for full diagnostic data from the divertor Thomson scattering (DTS) and IR camera. However, this shape turned out inducing very weak plasma response due to the low kink response, confirming the conclusion in Sec. 4.1 for the role of plasma shape in plasma response and separatrix splitting. Consequently, there was no strike point splitting from the IR heat flux profile

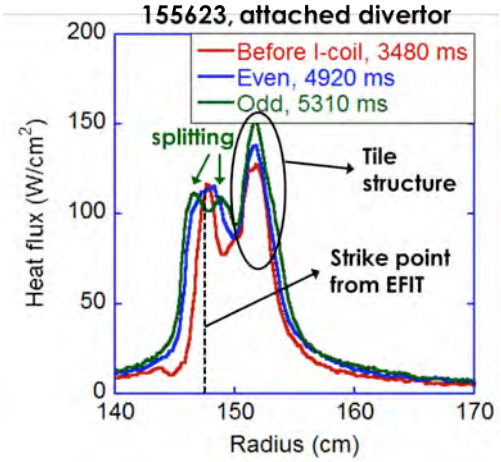


Fig. 5-11. Measured heat flux profiles before 3D fields are applied (red) and with I-coils energized with even (blue) and odd (green) phasing

observed for the $n$=3 even parity and only a subtle but persistent splitting was observed for the odd parity. Figure 5-11 shows an example of heat flux profile for each case. Since the weak or no strike point splitting by applied 3D fields represent weak 3D response, it is not surprising that the divertor detachment was not affected by 3D fields. Since the causal relationship is now better understood following the data analysis of these discharges, a follow-up experiment to be performed later in 2014 will focus on the effect of plasma shape and collisionality on the plasma response and the divertor plasma regime.

**References**

[1] T.E. Evans, *et al.*, *Contrib. Plasma Physics* **44**, 235 (2004).

[2] P. Cahyna, *et al.*, *J. Nucl. Mater.* **415**, S927 (2011).

[3] J.D. King, *et al*., *Rev. Sci. Instrum.* **85**, 083503 (2014).

[4] M.J. Lanctot, *et al.*, *Phys. Plasmas* **18**, 056121 (2011).

[5] K. Kim, J.-K. Park, G. J. Kramer, A. H. Boozer, *Phys. Plasmas* **19**, 082503 (2012).

[6] A. Wingen, *et al.*, *Nucl. Fusion* **54**, 064007 (2014).

[7] J.-W. Ahn, *et al.*, *Plasma Phys. Control. Fusion* **56**, 015005 (2014).

[8] Y. Feng, F. Sardei and J. Kisslinger, *J. Nucl. Mater*. **266–269**, 812 (1999).

# 6. Locked-mode Stabilization

## 6.1 Introduction and Background

Understanding the formation and stability of three-dimensional (3D) helical modes in the core of an otherwise, axisymmetric toroidal configuration, is still one of the challenges of current fusion research. Small deviations from toroidal axisymmetry are well known to destabilize non-rotating tearing modes (a.k.a. locked-modes), which can significantly impact plasma operation. Discharge scenarios with error-field-induced locked-modes (like the one illustrated in Fig. 6-1) have been studied in several tokamak devices and are observed to result in a strong density pump-out, partial or complete braking of core toroidal rotation, modification of the sawtooth activity in the core and significant reduction in energy and particle confinement, often leading to disruptions and associated vertical displacements. These 3D perturbations are more easily produced in low-density plasmas, and so are of most concern for ITER, especially during the early heating phase proposed for high-confinement H-mode access. This restriction has placed design and operational constraints on ITER that are now considered as essential, with some form of error-field-correction using 3D coils as well as external or intrinsic torque to drive plasma rotation for mode stabilization.

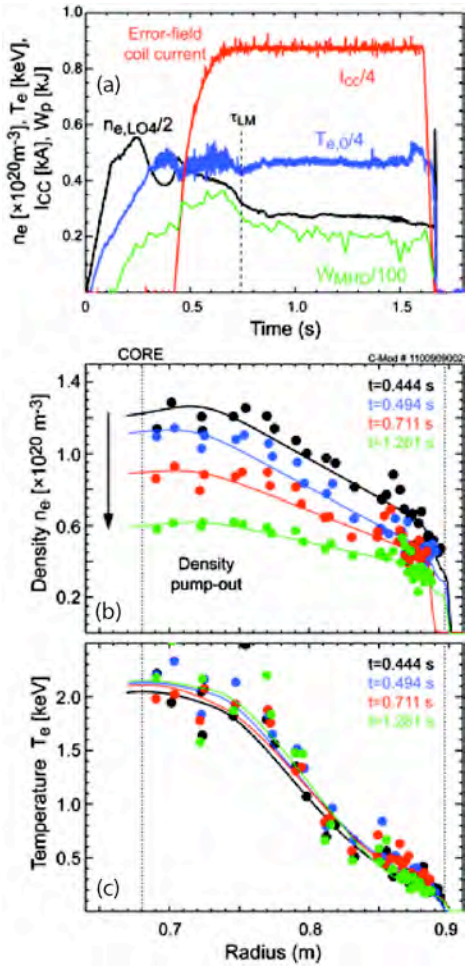


Fig. 6-1. (a) Error-field-induced locked-mode discharge in Alcator C-Mod. Electron $n_e$ and $T_e$ profiles at different times during mode-locking are shown in (b) and (c), respectively.

Error fields arise inevitably from departures from axisymmetry in the poloidal and toroidal field circuit such as coil positioning errors, eddy currents, coil feeds and connections, etc. Experimentally, it has been observed that the resonant *(m,n)=(2,1)* field component can induce a *(2,1)* locked-mode under various discharge regimes in tokamaks with distict aspect ratio (Refs [1–5] and references therein). In the absence of rotation, the response of a tearing-stable plasma to a static nonaxisymmetric field perturbation results in the formation of a static island whose size will typically be greater than that of the "vacuum island". In rotating plasmas helical currents are induced in the rational surface, which oppose the perturbation and inhibit island formation (e.g. tearing of flux surfaces). However, finite resistivity introduces a phase shift that gives rise to a $\tilde{J} \times \tilde{B}$ torque, which in

steady-state must be balanced by a viscous drag. For small perturbing fields, the rotation frequency remains close to its "natural" value $\omega_0$. The use of tangential neutral beams imparting toroidal momentum will result in an increase of $\omega_0$ and therefore the magnitude of the required perturbation. When the external perturbation is sufficiently large to slow the rotation to about $\omega_0/2$, there is an abrupt transition to locked-mode and significant tearing, the island grows nonlinearly and the plasma rotation slows abruptly to lock to the frame of the perturbation at the rational surface. This effect is generally called "mode penetration" [1–5]. Experimentally, the use of a high-resolution ECE imaging diagnostic enables the identification of the magnetic island during error-field-induced locked-modes; these islands are generally located at mid-radius as shown in Fig. 6-2 (Refs [6,7]).

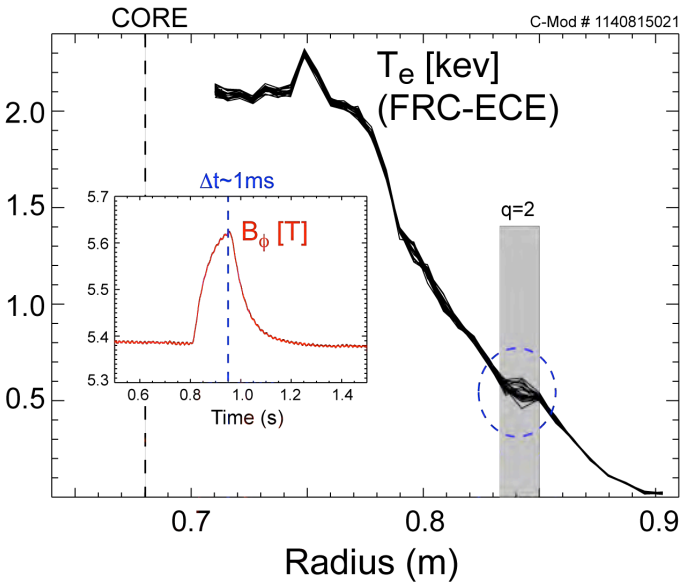


Fig. 6-2. Electron temperature profiles showing flattening just inside the nominal $q$=2 radius caused by a "waggle" in the toroidal-field during a locked-mode experiment in Alcator C-Mod [5–7].

The relative magnitude of the critical helically resonant field obtained from torque balance considerations can be parameterized as $\frac{B_{\perp,mn}}{B_T} \propto \omega_0 \tau_A \left(\frac{\tau_{rec}}{\tau_v}\right)^{1/2}$ where, $\tau_A = R\sqrt{\mu_0 n_i(r_s) m_i}/B$ is the Alfvén time calculated at the rational surface of interest, and $\tau_{rec}/\tau_v$ is the reconnection time normalized to the viscous diffusion time. For a given perturbation locking is favored at lower density $B_{\perp,mn} \propto \sqrt{n_i}$, as the electromagnetic torque is applied in slowing less mass. The dependence with magnetic field is not strong since $\tau_A \propto 1/B$. In the absence of bulk rotation the natural rotation frequency for a tearing mode is expected to be of the order of the electron diamagnetic frequency, $\omega_0 \rightarrow \omega_{D,e} = \nabla p_e / e n_e B r_s$, so the sensitivity to error fields might expect to be greater as the device and field increases.

Experimental locked-mode threshold studies performed in various tokamaks of different aspect ratio have considered only engineering macroscopic parameters resulting in a scaling law of the form $B_r^{lock}/B_T \propto \bar{n}_e^{\alpha_n} B_T^{\alpha_B} q_{95}^{\alpha_q} R_0^{\alpha_R}$ (Refs [1–15] and references therein). The determination of this dependence is useful for extrapolating low-aspect and standard-aspect ratio tokamaks results to ITER. However, the influence of drift-MHD as well as collisional and neoclassical flow-damping effects dependent on local kinetic profiles [10–13] can alter the predicted scaling and have not yet been considered. In addition, the locked-mode threshold including the effects of plasma rotation can be approximately $\left(\delta B_{2/1}/B_{t,0}\right)_\omega \approx \left(\delta B_{2/1}/B_{t,0}\right) \cdot \left(0.2\omega_\phi/\omega_D\right)^{1.5}$, where $\omega_\phi$ and $\omega_D$ are rotation and ion diamagnetic frequency [12]. This scaling suggests that there is a

strong dependence on rotation frequency offering a window of opportunity for mode stabilization and damping regardless of the torque source (external and/or intrinsic). Such stabilization should be compared with more traditional techniques like radio-frequency (rf) electron heating and current drive. The toroidal velocity is a very attractive parameter for scaling the locked-mode thresholds by its direct relation with the viscous torque. The experimental validation of these new theoretical models [12–15] should be investigated in concert by the MHD teams at DIII-D, Alcator C-Mod and in the future, NSTX-U. Section 6.2 of this report discusses the stabilization experiments in DIII-D using electron heating and current drive while results from Alcator C-Mod using ion heating are summarized in Sec. 6.3. The conclusions are presented in Sec. 6.4.

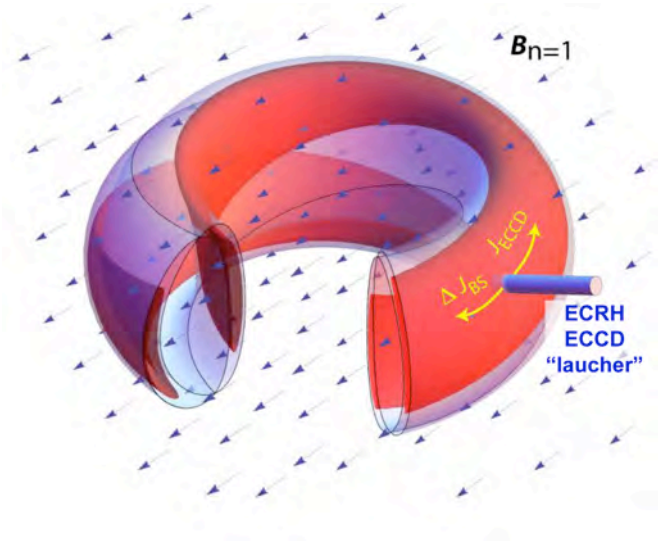


Fig. 6-3. Artistic rendering of recent experiments in DIII-D where *n=1* magnetic perturbations give control of LM toroidal position first, and then EC launcher completely suppressed locked modes by ECCD [15–17].

### 6.2. Stabilization of Locked-modes Using ECRH/ECCD and NBI in DIII-D

Previous tests on COMPASS-D [10,16] and new experiments DIII-D [17–19] have shown that ECRH and ECCD near the *q=2* rational surface can stabilize and even remove locked-modes. Stabilization by ECCD is well developed in several tokamaks but it becomes impossible if mode "locks" to the error-field or to the vacuum vessel wall in a position not accessible to the ECCD launcher. Recent experiments in DIII-D used *n=1* magnetic perturbations to control the rotation and toroidal phase of locked modes and of their rotating precursors, thus enabling their first full suppression by modulated or continuous ECCD as illustrated in Fig. 6-3. Once the island is "positioned" in front of the EC launcher, locked modes are completely suppressed by ECCD while without ECRH or ECCD the mode caused a disruption.

In the first set of experiments the applied perturbations were static and caused the rotating precursor to directly lock in a position such that its O-point was accessible to localized and continuous ECCD. ECCD in the O-point rapidly and completely stabilized the locked-mode and avoided a disruption as shown in Fig. 6-4. A key aspect in the stabilization mechanism is that RF current drive at *q=2* is greater that the missing bootstrap current so higher ECCD power was more stabilizing; ECCD was also found to be more efficient than simple ECRH heating in the O-point. For ECCD in the X-point the locked-mode was increased in amplitude. For ECCD in the X-point the locked-mode was increased in amplitude. For ECCD at intermediate toroidal

locations the mode grew slower and the disruption was delayed, but not avoided (see various stabilizing options illustrated in Fig. 6-4). Locked-mode suppression permitted disruption-free operation at $\beta_N$ as high as 2.5 in discharges which otherwise disrupted at $\beta_N$ as low as 1.7 (Fig. 6-5). The confinement was also improved, ELMs and *3/2* tearing modes reappeared and the H-mode was not lost as a result of suppression mechanism. ECCD at *q=2* prevents reappearance of *2/1* tearing modes, whether locked or rotating. Complete locked-mode stabilization was observed in slowly rotating plasmas for cases of balanced NBI. For unbalanced NBI, instead, the locked mode was often unlocked and accelerated by the NBI torque before being completely suppressed by the ECCD. The mode amplitude was observed to decrease as the rotation rate increased.

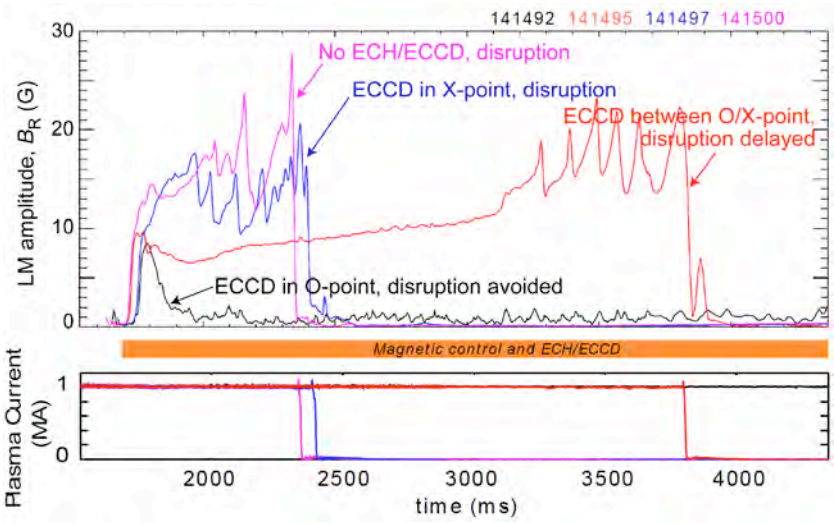


Fig. 6-4. Magnetic control of locking phase allowed ECCD deposition in O-point to suppress locked-modes and avoid disruptions [15–17].

Another possibility for avoiding locked modes is to raise the error field threshold using only the external torque imparted by a tangential NBI to spin the plasma. The increase in threshold with NBI has been demonstrated experimentally on DIII-D in L mode [20] and also at TEXTOR [21]. Increases were also observed on JET experiments [10,22] when 2 MW of co-injected neutral beam doubled the mode thresholds. Back-of-an-envelope calculations shown in ref. [19] indicated that 5–10 MW of tangential counter-injected 1 MeV beams in ITER would increase the error field threshold by about a factor of 5. Unfortunately, a tangential NBI system will not be deployed at ITER, and *n=1* magnetic perturbations, paramount for the ECCD stabilization scheme discussed above, will be used instead for various applications (e.g. error

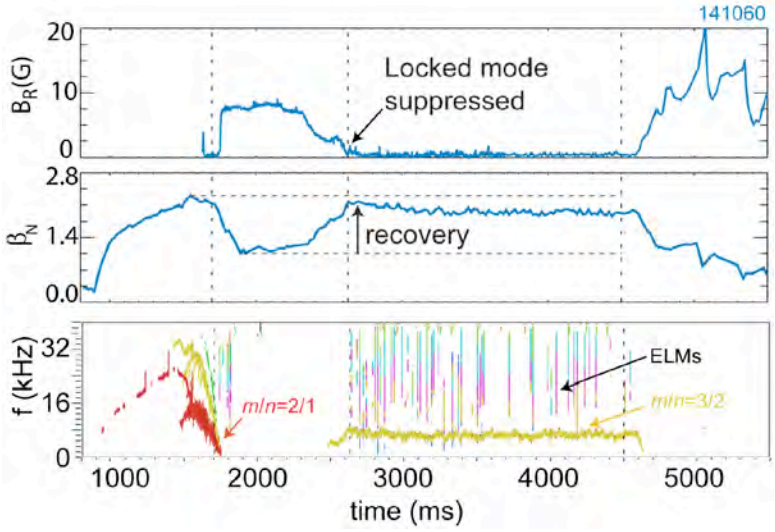


Fig. 6-5. $\beta_N$ is recovered after locked-mode suppression. ELMs and 3/2 modes reappeared.

field correction, ELM pacing and suppression as well as RWM stabilization). Therefore, additional actuators like radio frequency current drive and heating techniques - which could also have an effect driving toroidal and poloidal rotation - should be considered and tested for the sole purpose of locked-mode stabilization.

### 6.3. Locked-mode Avoidance and Recovery with ICRH and LHCD in C-Mod

As discussed above, locked-mode avoidance in low-density Ohmic discharges is highly desirable, if not crucial, for reliable tokamak operation. Error-field-induced locked-modes can be studied in C-Mod at ITER toroidal fields and without NBI fueling and momentum input. Locked-mode excitation is achieved by ramping-up a set of external "A-coils" capable of producing non-axisymmetric, predominantly $n$=1, fields with different toroidal phase and a range of poloidal mode $m$ spectra [Ref. [9] and Fig. 6-1(a)]. The objective of this research at Alcator C-Mod is two-fold. First, study the evolution of the plasma profiles ($T_{e,i}$ and $v_{\phi,\theta}$) during the formation of error-field-induced locked-modes at ITER fields without external sources of fueling and momentum input. And second, attempt stabilization or "unlocking" of the core plasma using available radio frequency techniques such as ICRH and lower hybrid current drive (LHCD). The typical plasma discharge parameters were $I_p$~0.8 MA, $B_{t,0}$~5.4 T, $T_{e0}$~2.0 keV and $n_{e0}$=(0.6–1.3)×$10^{20}$ $m^{-3}$ [see also Figs. 6-1(b) and 6-1(c)]. The safety factor on axis was $q_0$~0.9 while $q_{95}$~4. As a result, sawteeth activity was present; plasma discharges with long- and short-lived core MHD activity – such as impurity-snakes [23,24] and electron fishbones [25,26] – often observed during Ohmic, ICRH and LHCD scenarios, were not considered in this study.

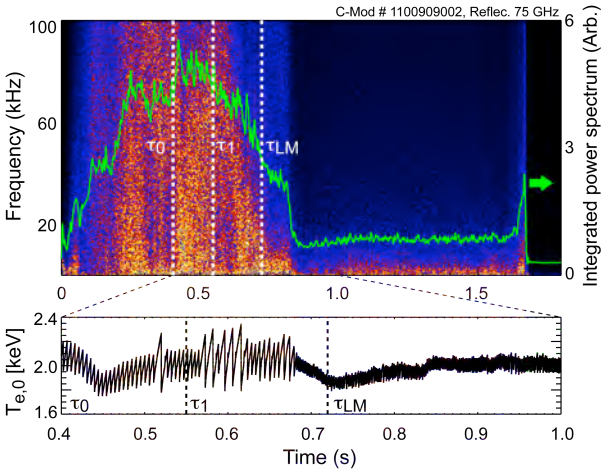


Fig. 6-6. (a) Spectrogram and integrated power spectrum (10<$f$<100 kHz) of density fluctuations measured by a 75 GHz reflectometer. The modification of sawteeth activity from the ECE Grating Polychromator electron temperature diagnostic is shown in (b).

A strong decrease of the plasma density is commonly observed in error-field-induced locked-mode discharges. The pump-out at the edge is approximately 30% while the core density is typically reduced a factor of two, at nearly constant electron temperature [Figs 6-1(b) and 6-1(c)]. This density pump-out can also be the root for a reduction in the mode-locking thresholds and is the main cause for a reduction of 50% in stored energy and a loss of confinement time, β and neutron production. As a result of the density pump-out there is a significant reduction of density fluctuations measured by the reflectometer as depicted in Fig. 6-6(a); the time window between $\tau_0$ and $\tau_1$ corresponds to the raise-time of the control coils

to their maximum current of $I_{CC}$=3.5 kA. The change of the sawtooth instability at the locked-mode onset $t \sim \tau_{LM}$ [Figs. 6-1(a) and 6-1(b)] is also noteworthy: the temperature excursions during the ramp-up phase changed from $\Delta T_{e,0}$~200–250 eV at 0.2 kHz – before the locked mode, to $\Delta T_{e,0}$~100–150 eV at 6.6 kHz during the steady state. The characteristic times $\tau_{LM}$ which also "marks" the locking-phase of the core plasma were reproducible to within ±65 ms and showed to be sensitive to the density evolution ($\langle n_e \rangle \sim 0.75\times10^{20}$ m$^{-3}$) in accordance with a strong linear dependence of mode-locking thresholds ($\alpha_n \rightarrow 1$).

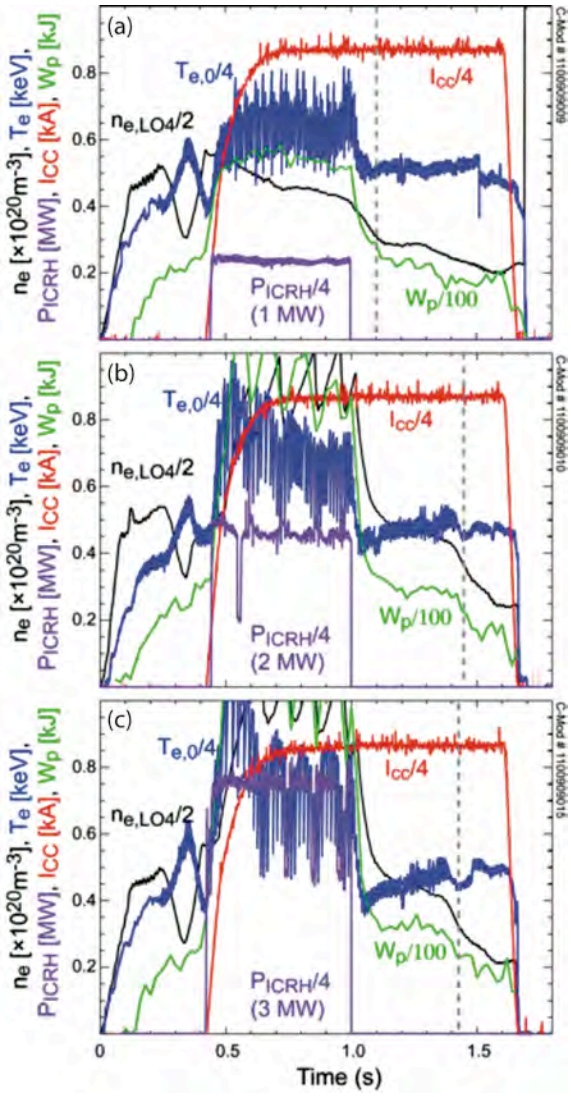


Fig. 6-7. Time history of the electron density and temperature, ICRH power, error-filed coil current and stored energy during the LM avoidance experiments using (a) 1, (b) 2 and (c) 3 MW of ICRH.

Ion cyclotron resonance heating has had traditionally a much weaker effect driving rotation and changing locked-mode thresholds than NBI. Previous MHD studies at JET during a 10 MW ICRH heated high-$\beta_p$~1 scenario found similar locked-mode thresholds in comparison to the ohmic values [8]. However, the ICRH effects on Alcator C-Mod plasmas may open a new window of parameter-space never tested due to an increased factor of 10–30 in power density since the total plasma volume of JET is 100 m$^3$, in comparison with the 1 m$^3$ of C-Mod. The first experiments aiming at delaying the mode onset in Alcator C-Mod considered a coarse power scan in steps of 1 MW of ICRH power *in-sync* with the $I_{CC}$ ramp-up in the control coils [Refs [6–8] and Fig. 6-7(a)]. The use of 1 MW for instance, delayed the mode-onset but was not sufficient to transition into an H-mode even when the stored energy was doubled from 25 to 55 kJ. However, for $P_{ICRH}$=2 and 3 MW the plasma experienced transient L→H transitions [Figs 6-7(b) and 6-7(c)] as the average density, core ion temperature, toroidal velocity and stored energy increased up to $2\times10^{20}$ m$^{-3}$, 2–2.5 keV, 50–60 km/s and 150 kJ, respectively. Nonetheless, when ICRH power is turned off the core plasma "locks" at later times and its characteristic high-frequency magnetic signatures reappear until the end of the discharge [6,8]. The locking times ($\tau_{LM}$) after the heating pulse are similar for all these cases due to nearly

identical time-histories of density, temperature and toroidal flow velocity. H-mode access in the presence of an error-field appears therefore not be of challenge at these high densities.

A different set of experiments used ICRH power pulses well into the low density non-rotating phase of the locked-mode in order to change the plasma profiles and its gradients as well as attempt unlocking the core plasma [6,8]. These L-mode plasmas did not experience transitions to H-mode due to their lower-density (~1/2 of the density before locked-mode onset), even though $P_{ICRH}$ was raised up to 3 MW. During these recovery experiments the core electron and ion temperature increased 400, 600, 1000 eV when heated with $P_{ICRF}$=1, 2 and 3 MW, respectively. The density augments were small and the stored energy increased 20, 35, 55 kJ, respectively (Fig. 6-8). The high-frequency magnetic signatures remained when 1 MW was applied but were suppressed for the cases with $P_{ICRF}$=2 and 3 MW. A comparison of the toroidal flow velocity and ion temperature between an Ohmic and ICRH-heated locked-mode measured with a high-resolution x-ray crystal spectrometer [27,28] is shown in Fig. 6-9. One interesting detail is that the change in core toroidal rotation for the ICRH-heated case *points* in the counter-current direction recovering the direction and magnitude of the toroidal flow before the formation of the locked-mode [Fig. 6-9(c)], but contrary to the expected Rice-scaling in the co-current direction [29]. However, the locked mode occurs at a low density near the LOC/SOC transition where rotation reversals are commonly observed [30,31].

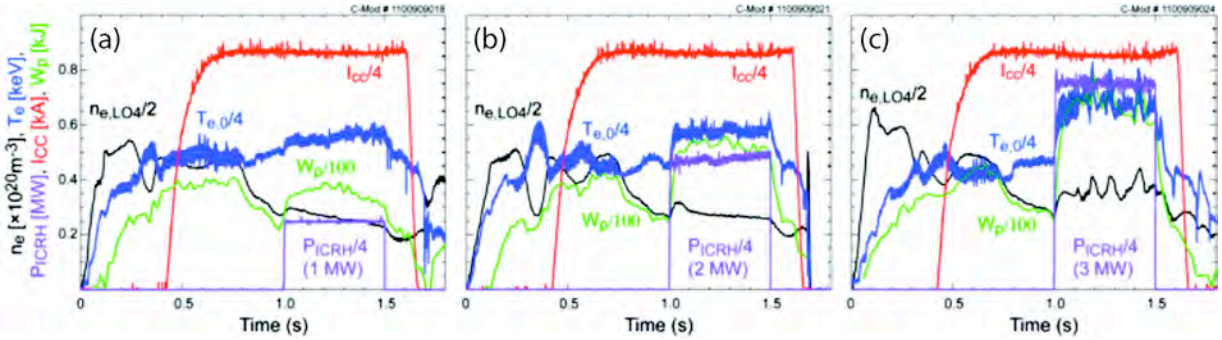


Fig. 6-8. Time history of the electron density and temperature, ICRH power, error-filed coil current and stored energy during the LM recovery experiments using (a) 1, (b) 2 and (c) 3 MW of ICRH.

The C-Mod's ICRH system provides on- and/or off-axis heating in experiments with no external particle and momentum sources. This capability enables a unique contribution to worldwide research in support of ITER, to study error-field locked-mode thresholds and unlocking by comparing C-Mod's results to those from devices that utilize neutral beam injection. The effects of ion heating observed on unlocking the core plasma may be due to ICRH induced flows in the plasma boundary [32,33], or modifications of plasma profiles which change the underline turbulence (e.g. from ITG to TEM). It is thought that $P_{ICRH}$ can be modifying the temperature and density gradients at the edge, that generate a toroidal flow through anomalous momentum transport, which in turn "unlocks" the core plasma, though the details of this are not fully understood. As mentioned above, the generation of a poloidal or toroidal flow velocities is a very

attractive parameter for scaling the locked-mode thresholds by its direct relation with the viscous torque.

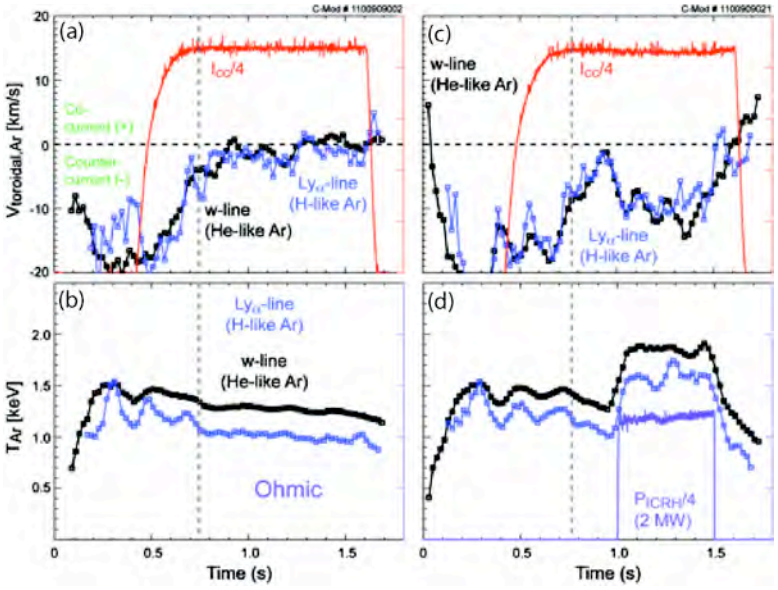


Fig. 6-9. Comparison of the toroidal flow velocity and ion temperature inferred with the x-ray crystal spectrometer (using the w- and Lyα-line of the He- and H-like spectra) for an Ohmic [(a) & (b)] and ICRH-heated [(c) & (d)] locked-modes, respectively.

Recent experiments performed during the last quarter of 2014 confirmed the results obtained with the ICRH power scan aimed at delaying the mode onset as well as unlocking the core plasma. These experiments aimed also at "fine-tuning" the ICRH power to evaluate the power density threshold for avoiding the mode locking as well as determine whether the H-mode accessibility varies in the presence of error fields. A comparison between the unlocked and locked phases was also performed using the toroidal and poloidal charge exchange recombination spectroscopy (CXRS) as well as the gas puff imaging (GPI) diagnostics. The simultaneous use of $D_2$ and He puffs [30,31] help in the assessment of the plasma flows in the boundary ($\rho$>0.8) during the locked-mode transitions during Ohmic and ICRH scenarios. Measurements of the toroidal velocity from the Doppler shift shows a decrease from about 20 km/s to zero over the course of about 70 ms during the locking phase of the Ohmic plasma. This is approximately equivalent to the time it takes for the density to pump out as the plasma locks. During the unlocking phase using ICRH, the CXRS measurements indicate that the edge plasma rapidly spins up to about 20 km/s much faster than the braking when the locked mode sets in. The GPI power spectrum for views inside the separatrix showed also drastic changes in the fluctuations levels during the transitions to the locking and unlocking phases [7,8].

### 6.4. Conclusions

Using 3D fields to control the position of magnetic island and aid ECCD-stabilization of locked modes has been demonstrated in DIII-D. ECCD deposition in "O-point" and "X-point" has different effects: the former being stabilizing, while the latter destabilizing. When ECCD deposition fall "in-between", the saturated locked-mode is held for several energy confinement times. Stabilization improves with ECCD power and was found to be more effective than pure ECRH. However, after ECCD is turned off, 2/1 locked-modes grow again. The challenge of implementing this stabilization technique relies on the fact that magnetic islands can lock in a

position "toroidally" not accessible by the ECCD antennae. For this case, *n=1* magnetic perturbations of sufficient strength should give control of locked-mode toroidal position first.

Error-field-induced locked-modes have been studied also in Alcator C-Mod at ITER-$B_\phi$, without NBI fueling and momentum input. Delay of the mode-onset and locked-mode recovery has been successfully obtained without external momentum input using ICRH. The use of external heating *in-sync* with the error-field ramp-up resulted in a successful delayed of the mode-onset when $P_{ICRH} \gtrsim 1$ MW, which demonstrate the existence of a power threshold to "unlock" the mode; in the presence of an error field the L-mode discharge can transition into H-mode only when $P_{ICRH} \gtrsim$ 2 MW and at high densities. During the recovery experiments the "induced" toroidal rotation was in the counter-current direction recuperating the direction and magnitude of the toroidal flow before the mode onset. However, once $P_{ICRH}$ is turned off, the core plasma "locks" at later times depending on the evolution of $n_e$ and $v_{\phi,\theta}$. Studying the connection between $\nabla T_{e,i}$ and $v_{\phi,\theta}$ through the residual stress and the effects of neoclassical toroidal viscosity will shed light on the mechanisms unlocking the core plasma. Regardless of the torque source, the scaling calculated by J-K. Park et al. [9] - $\left(\delta B_{2/1}/B_{t,0}\right)_\omega \propto V_\phi^{1.5}$- suggests that there is a strong dependence on plasma rotation offering a *window-of-opportunity* for locked-mode stabilization.

**References**


[1] T.C. Hender, *et al*., *Nucl. Fusion* **32**, 2091 (1992).

[2] T.C. Hender *et al.*, *Nucl. Fusion* **47**, S128 (2007).

[3] R.J. La Haye, *et al.*, *Phys. Fluids* **B4**, 2098 (1992).

[4] T.H. Jensen, *Phys. Fluids* **B3**, 1650 (1991).

[5] R. Fitzpatrick, *Nucl. Fusion* **33**, 1049 (1993).

[6] L. Delgado-Aparicio, *et al., Proc. of the 41st European Physical Society Conf. on Plasma Physics, Berlin, Germany* (2014).

[7] L. Delgado-Aparicio, *et al., Proc. of the 56th Annual Meeting of the APS Division of Plasma Physics, New Orleans, Louisiana* (2014)

[8] L. Delgado-Aparicio, *et al.*, to be submitted to *Phys. Rev. Lett*. (2014).

[9] S.M. Wolfe, *et al*., *Phys. Plasmas* **12**, 056110 (2005).

[10] R.J. Buttery, *et al*., *Nucl. Fusion* **39**, 1827 (1999).

[11] J.E. Menard, *et al., Nucl. Fusion* **50**, 045008 (2010).

[12] J-K. Park, *et al., Nucl. Fusio,* **52**, 023004 (2012).

[13] A. Cole, *et al., Phys. Plasmas* **13**, 032503 (2006).

[14] A.B. Mikhailovskii, *et al*., *Plasma Phys. Report* **21**, 789 (1995).

[15] A. Cole, *et al., Phys. Rev. Lett*. **99**, 065001 (2007).

[16] P.G. Carolan, *et al*., *Proc. of the 41st European Physical Society Conf. on Plasma Physics, Montpellier* (1994).

[17] F. Volpe, *et al.*, *Phys. Plasmas* **16**, 102502 (2009).
[18] F. Volpe, *et al., Proc. of the 41st European Physical Society Conf. on Plasma Physics, Berlin, Germany* (2014).
[19] F. Volpe, *et al.*, submitted to *Plasma Phys. Control. Fusion* (2014).
[20] R.J. La Haye, General Atomics Report GA-A22468 (1997).
[21] P.C. De Vries, *et al.*, *Plasma Phys. Control. Fusion* **38**, 467 (1996).
[22] A. Santagiustina, *et al.*, *Proc. of the 22nd European Physical Society Conf. on Plasma Ph*ysics, *Bournemouth, Geneva* (1995).
[23] L. Delgado-Aparicio, *et al.*, *Phys. Rev. Lett.* **110**, 065006 (2013).
[24] L. Delgado-Aparicio, *et al.*, *Nucl. Fusion* **53**, 043019 (2013).
[25] L. Delgado-Aparicio, *et al.*, submitted to *Phys. Plasmas* (2014).
[26] L. Sugiyama and L. Delgado-Aparicio, to be submitted to *Phys. Plasmas* (2014).
[27] M.L. Reinke, *et al.*, *Rev. Sci. Instrum.* **83**, 113504 (2012).
[28] L. Delgado-Aparicio, *et al.*, *Plasma Phys. Control. Fusion* **55**, 125011 (2013).
[29] J.E. Rice, *et al.*, *Nucl. Fusion* **47**, 1618 (2007).
[30] J.E. Rice, *et al.*, *Phys. Plasmas* **19**, 056106 (2012).
[31] R. McDermoth, *et al.*, *Nucl. Fusion* **54**, 043009 (2014).
[32] J.L. Terry, *et al.*, *Proc. of the 24th IAEA Fusion Energy Conf., San Diego, California* (2012) Paper EX/P5-39.
[33] I. Cziegler, *Plasma Phys. Control. Fusion* **54**, 105019 (2012).

## 7. Acknowledgment

This material is based upon work supported in part by the U.S. Department of Energy, Office of Science, Office of Fusion Energy Sciences, using the DIII-D National Fusion Facility, a DOE Office of Science user facility, under Award DE-FC02-04ER54698, DE-AC02-09CH11466 and DE-FC02-99ER54512.